Seismic Wave Attenuation in

Fluid Saturated Rocks

by

Hege Susanne Birkeland

Cand. Scient thesis

Institute of Solid Earth Physics

University of Bergen

December 2002

Acknowledgment

Contents

Chapter 1

Introduction

Far more information about the constitution of the earth is obtained from seismic studies than from all other geophysical methods combined.

Of the two main aspects of the wave propagation - velocity and attenuation - knowledge of velocities has provided most of our information about the earth. Attenuation data is of much more limited use. Partly because it is difficult to obtain, but mainly because it is difficult to interpret in terms of rock properties. This is due primarily to our lack of understanding of the physical processes involved in the attenuation of seismic waves.

P- and S-waves influence and deform the medium very differently, and one can therefore expect to obtain different kinds of information from these two wave types. Both seismic velocities and seismic attenuation are highly sensitive to some rock physics parameters, such as porosity, cracks and fluid saturation. The combined use of the information obtained from both the velocity ratio V_p/V_s, and the attenuation ratio Q_p/Q_s will thus give evident characteristics for several types of rocks.

The realization of the advantages practical use of information obtainable attenuation has, prompted a strong augmentation in interest and research concerning attenuation in the fields of both seismology and rock physics.

And due to the improved and more precise methods of performing seismic surveys, and thus obtain higher quality data, it is now possible to extract this information and make it useful. Potentially, this gives the opportunity to improve reservoir characterization for future data acquisitions - both in order to find new reservoirs

and to monitor already producing reservoirs through 4D seismic.

In this thesis attenuation, represented by Q-factor, is the subject of the research performed. Models are explored to extend the understanding of this aspect of wave propagation.

The main objectives of the thesis can be divided into two parts;

- discuss how the attenuation is a function of the saturation degree in a reservoir, and how this influences the amplitude and phase rotation of a seismic signal,

- evaluate how $Q_P(z)$ and $Q_s(z)$ influence the resolution powers for PP-, PS- and SS-waves.

The first two chapters describe the theoretical aspects of attenuation, and physical parameters and phenomena involving attenuation.

Chapter 2 presents several definitions of both the attenuation coefficient α, and (mainly) the quality factor Q. Mechanisms causing, and different models describing attenuation (constant Q and nearly constant Q) are also outlined. Finally, the principles of seismic resolution, both vertical and horizontal are outlined.

Wave propagation given by Zoeppritz equations is presented in chapter 3. Based on these equations, reflection and transmission are defined.

A short introduction on how wave modelling is implemented in Nucleus (a software) is also given in this chapter.

The second part of the thesis is devoted to modelling. A thorough description of how the construction and exploration are performed is given. The results are carefully studied and analyzed. For each part of the modelling, individual conclusions are made.

The first of these chapters, chapter 4, deals with the attenuation effects on amplitude and phase distortion. Different scenarios are compared, and general tendencies are pointed out.

Chapter 5 regards more complex scenarios which are used to further investigate how attenuation effects a seismic signal. In this chapter the effect of the presence of a gas-cloud in the overburden is explored.

A real set of data is explored with the same object in chapter 6. Well data from the Jotun field in the North Sea is used to demonstrate attenuation effects on

real data. The results in this chapter are also compared to those of the previous modelling chapters to evaluate if they all show the same tendencies.

General remarks and conclusions are given in the last chapter.

Chapter 2

Propagation and attenuation of elastic waves

2.1 Introduction

In this chapter the basic theory evolving elastic and anelastic materials, and P and S-waves are presented.

Several definitions of the two parameters denoting attenuation will be introduced, along with a thorough description of the mechanisms causing this loss of energy for seismic waves.

A presentation of different models for the quality factor, concerning whether or not it is dependent on frequency, will also be done at the end of this chapter. Finally there will be an outline of the main features of seismic resolution.

This chapter is meant to give a better basic understanding of seismic attenuation and resolution, before proceeding to a more detailed and profound discussion in the following chapters.

2.2 Elastic and anelastic materials

When a fixed solid body is exposed to an external force, F , it will change its shape and size. An *elastic material* will return to its original form and size after the external force is removed. If small deformations occur during a short period

of time, the material will still be considered to be elastic. A material that does not return to the original size and shape is on the other hand considered to be *inelastic*. The deformation the external force causes is then said to be irreversible. The transition between reversible and irreversible deformation is called the elastic limit.

Stress is defined as a force per unit area. The magnitude stress (σ) is not just a function of the force (F) from which it was derived. It also relates to the area (A) on which the force acts (Davis & Reynolds, 1996):

$$\sigma = \frac{F}{A}. \tag{2.1}$$

When a body is subjected to stress, the resulting deformations will be called strain. Strain, e, is defined as the relative change in the shape of the body (Fowler, 1998). Uniform stress will cause a solid to change in size, but not in shape. Differential stress on the other hand causes a change in shape, but it may or may not also change in size.

The theory of elasticity gives a mathematical relation between stress and strain in a solid. This theory is based on an assumption of infinitesimal and homogeneous deformation. This is an assumption which simplifies the mathematical framework considerably. Because of this assumption the higher order components in the series of the extension ϵ and the shear deformation γ are excluded. In the theory of infinite small strains, the ratio between forces and deformation is mainly based on, and given by Hooke's law. Hooke's law gives relation between stress and strain:

$$\sigma = Ke \,, \tag{2.2}$$

where K is the elastic parameters (stiffness tensor) of the material.

In an isotropic solid the elastic properties at a point will be independent of directions, and they can be described by only two elastic constants. Based on this, Kanestrø m (1982) gives the following relation between stress and strain in a solid that is perfectly elastic and isotropic:

$$\tau_{ij} = \lambda \delta_{ij} e_{kk} + 2\mu e_{ij} \,, \tag{2.3}$$

where δ is the Kronecker delta, μ is the shear modulus, and λ is Lam's parameter. The notations $_i$, $_j$ and $_k$ refers to elements in the strain matrix.

τ_{ij} represents an element in the *stress tensor*, τ. In a Cartesian coordinate system, this tensor may be defined by the tractions across the yz, xz, and xy planes (Shearer, 1999):

$$\tau = \begin{bmatrix} t_x\left(\widehat{\mathbf{x}}\right) & t_x\left(\widehat{\mathbf{y}}\right) & t_x\left(\widehat{\mathbf{z}}\right) \\ t_y\left(\widehat{\mathbf{x}}\right) & t_y\left(\widehat{\mathbf{y}}\right) & t_y\left(\widehat{\mathbf{z}}\right) \\ t_z\left(\widehat{\mathbf{x}}\right) & t_z\left(\widehat{\mathbf{y}}\right) & t_z\left(\widehat{\mathbf{z}}\right) \end{bmatrix} = \begin{bmatrix} \tau_{xx} & \tau_{xy} & \tau_{xz} \\ \tau_{yx} & \tau_{yy} & \tau_{yz} \\ \tau_{zx} & \tau_{zy} & \tau_{zz} \end{bmatrix}. \tag{2.4}$$

Because the solid is in static equilibrium, there can be no net rotation from the shear stresses. For example, consider the shear stresses in the xz plane. To balance the torques, $\tau_{xz} = \tau_{zx}$. Similarly, $\tau_{xy} = \tau_{yx}$ and $\tau_{yz} = \tau_{zy}$, and the stress sensor is symmetrical.

The stress tensor contains only six independent elements, and these are sufficient to completely describe the state of stress at a given point in the medium.

The most customary elastic constants used are the bulk modulus k, the shear modulus μ, Poisson's ratio σ, Young's modulus E and Lam's parameter λ. For a perfectly elastic solid any of the tree first constants can be expressed by the other two. This relation is given by;

$$\sigma = \frac{3k - 2\mu}{2\left(3k + \mu\right)}. \tag{2.5}$$

Since both elastic and anelastic constants are very sensitive to the rock lithology, there is a discussion how these vary with various lithologies. It is by using the velocity of the P- and S- waves, and the attenuation of these that makes it possible to detect these variations from seismic data.

2.3   P- and S- wave velocities

Within an elastic medium body waves may propagate. There are two kinds of body waves; P- and S-waves.

P-wave is short for *primary* or *pressure* wave. It travels parallel to the direction of propagation, meaning that this kind of waves involve compression and rare-

fraction of the material as the wave passes through. It does not involve any rotation (Fig.2.1).
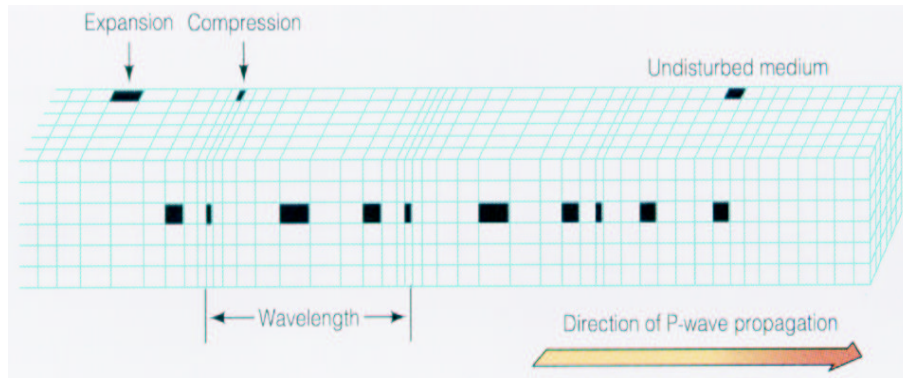
Figure 2.1: *Illustration of the particle movement of a P-wave. A P-wave causes alternate compressions and expansions in the rock the wave passes through (Skinner & Porter, 1995).*

Due to this, P-waves involve both a change in volume and shape of the material. It can be said that they are the analogue in a solid to sound waves in air. In an infinite, homogeneous, isotropic, elastic medium the P-wave velocity is given by the equation:

$$V_p = \sqrt{\frac{k + 4\mu/3}{\rho}}, \qquad (2.6)$$

where ρ is the density of the solid.

S-waves on the other hand involves shearing and rotation of the material as the waves pass trough. These waves do not involve changes in volume. The particle motion is transverse, meaning that it travels perpendicular to the direction of propagation (Fig. 2.2). As a consequence to this, the S-wave motion can be slip into a horizontally polarized motion termed SH, and a vertically polarized motion termed SV .

The motion of the SV wave has an orientation that can be connected to P-waves. Because of this, SV waves can be converted into P-waves at an interface between two layers. The velocity of an S-wave, at the same conditions as given for P-wave velocities, is given by:
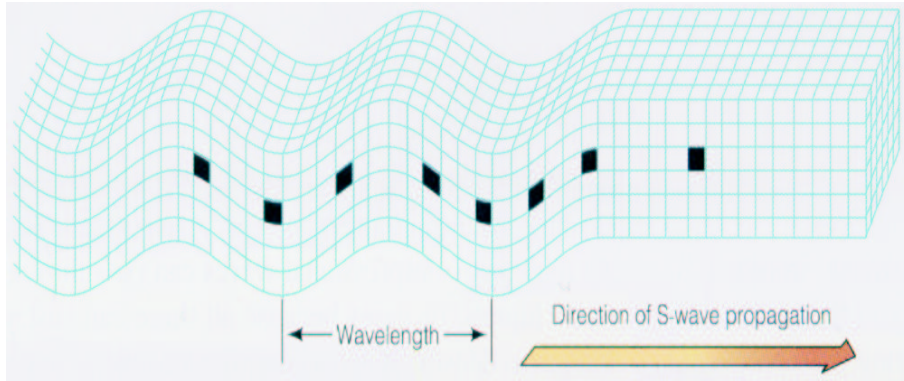
Figure 2.2: *Illustration of the particle movement of a S-wave. A S-wave causes a shearing motion in the rock the wave passes through (Skinner & Porter, 1995).*

$$V_s = \sqrt{\frac{\mu}{\rho}}. \tag{2.7}$$

Combining equation 2.6 and 2.7, gives an expression for the ratio between the two velocities;

$$\frac{V_p}{V_s} = \sqrt{\left(\frac{k}{\mu} + \frac{4}{3}\right)} = \sqrt{\frac{2\,(1-\sigma)}{1-2\sigma}}. \tag{2.8}$$

Both laboratory measurements and studies of well log show a connection between lithology and observed V_p/V_s values (Tatham, 1982). This agrees with the fact that the elastic parameters k and μ are highly dependent on different lithologies, which again influences the ratio of the P- and S-velocities. V_p/V_s is therefore considered an indicator of various rock lithologies. But one important note to this is that it is not just variations in the elastic constants in the matrix itself that influences the velocity ratio. Variations of k for possible fluids in the rock, plus the pore geometry are also factors that will influence this ratio. The relation between the velocity ratio V_p/V_s, k/μ and σ is shown in figure 2.3.

2.4   Attenuation parameters

In an ideal, perfectly elastic medium no elastic energy would be lost during the passage of a seismic wave. Geometrical spreading, reflection and transmission
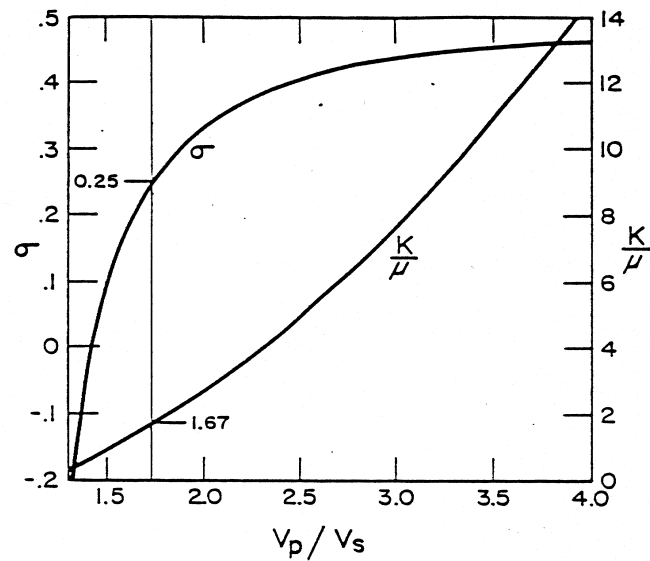
Figure 2.3: *The relation between the velocity ratio V_p/V_s, Poisson's ratio σ and the relative ratio of incompressibility and rigidity, k/μ (Tatham, 1982).*

of energy at an interface would in this case be the only factors to influence the amplitude of the seismic pulse. Meaning that it could propagate infinitely through the medium.

But the earth is far from perfectly elastic, and a propagating seismic wave will therefore attenuate with time due to different mechanisms causing energy losses. The total energy of a particle motion will continuously diminish, especially as a result of conversion from elastic energy into heat due to friction. The amplitude of the signal will be reduced and the phase distorted.

The attenuation properties in a medium can be described by several parameters. Generally one refers either to *the attenuation coefficient α*, or *the quality factor Q*.

2.4.1   The attenuation coefficient

Absorption of energy is constant per wavelength. The amplitude will therefore decrease a certain percentage compared to the previous wavelength. This leads to an exponential reduction of the amplitude with distance.

In case of a plane wave in a homogeneous medium the attenuation will be given

by

$$A = A_0 e^{-\alpha x}, \tag{2.9}$$

where A and A_0 is the present and the initial amplitude, respectively. x is the distance the wave has traveled, and α is the attenuation coefficient (Sundvor, 1989).

Rearranging equation 2.9, the attenuation coefficient will be expressed by;

$$\alpha = - \left[\frac{\ln (A/A_0)}{x} \right]. \tag{2.10}$$

α is dependent on the waves frequency, and it is thus dependent on both the medium and the frequency of the wave. This fact means that the attenuation coefficient is not a unique measure of the absorption in a medium.

2.4.2 The quality factor

There are several different ways to define the quality factor, Q, depending on the parameters used to consider the attenuation. These definitions will slightly differ from each other. But for those cases where the absorption is less than 10 ($Q > 10$), these differences can be ignored.

Some of the various definitions can be summed up as follows:

- The quality factor can be defined by the ratio of elastic energy ΔE dissipated during one cycle of harmonic motion of frequency ω and the maximum or the mean energy E accumulated during the same cycle (Udas, 1999);

$$\frac{1}{Q(\omega)} = \frac{1}{2\pi} \frac{\Delta E}{E}. \tag{2.11}$$

- Kanestrø m (1982) defines the quality factor by the parameter δ (the logarithmic decrement) :

$$\frac{1}{Q} = \frac{\delta}{\pi}, \tag{2.12}$$

where δ is the logarithm of the amplitude ratio between two subsequent

maximum (or minimum) of an exponentially attenuated sine wave; $\delta = \ln(A_1/A_2)$.

- For linear mechanisms the quality factor is defined as (Jackson & Anderson, 1970)

$$\frac{1}{Q} = \tan\varphi, \tag{2.13}$$

where φ is the phase angle between stress and strain.

- The quality factor can be defined using the complex visco-elastic moduli; $M = M_{re} + iM_{im}$ (Jones, 1992).

$$\frac{1}{Q} = \frac{M_{im}}{M_{re.}} \tag{2.14}$$

The P- and S-wave modules will in this case be given respectively as:

$$\frac{1}{Q_p} = \frac{K_{im} + \frac{4}{3}\mu im}{K_{re} + \frac{4}{3}\mu_{re}}, \tag{2.15}$$

$$\frac{1}{Q_s} = \frac{\mu_{im}}{\mu_{re}}. \tag{2.16}$$

- For the dynamic systems most commonly used to measure attenuation, Q may be defined in termed of a resonance-peak bandwidth (Johnston & Toksz, 1981):

$$Q = \frac{f_r}{\Delta f}. \tag{2.17}$$

Δf is in this case the frequency width between halfpower (3 dB in amplitude) points about a resonance peak at f_r on a power-frequency plot.

- The quality factor is also connected to the attenuation coefficient, α. Initially the relation describing this is given by equation (Klimentos & McCann, 1990):

$$\frac{1}{Q} = 2\alpha\lambda, \tag{2.18}$$

where λ is the wavelength.

But by ignoring small changes of phase velocity, c, with frequency f, Q^{-1}

is approximately

$$\frac{1}{Q} = \frac{\alpha c}{\pi f}.$$

(2.19)

2.4.3   The attenuation ratio.

A ratio between the P-wave attenuation and the S-wave attenuation may be derived from the definitions listed in subsection 1.4.2.

- Considering equation 2.11, this ratio gives the following expression:

$$\frac{Q_p^{-1}}{Q_s^{-1}} = \frac{\Delta E_p / (2\pi E_p)}{\Delta E_s / (2\pi E_s)}.$$

(2.20)

- Equations 2.15 and 2.16 combined, express the attenuation ratio by this equation:

$$\frac{Q_p^{-1}}{Q_s^{-1}} = \frac{\left(K_{im} + \frac{4}{3}\mu_{im}\right)\mu_{re}}{\left(K_{re} + \frac{4}{3}\mu_{re}\right)\mu_{im}}.$$

(2.21)

- The attenuation ratio is also defined by

$$\frac{Q_p}{Q_s} = \frac{2\left(1 - 2\xi'\right)}{\left(1 - \xi'\right)\left[3 + 4\left(\frac{\xi'}{1-\xi'}\right) + 8\left(\frac{\xi'}{1-\xi'}\right)^2\right]},$$

(2.22)

where the original expressions for Q_p^{-1} and Q_s^{-1} only are valid for low frequencies. But it is believed that equation 2.22 should be at least approximately correct to much higher frequencies. The parameter ξ' is the effective Poisson's ratio of a porous rock.

2.5   Attenuation mechanisms

There has been an increasing interest in seismic attenuation the last decades. This has created a need to better understand the mechanisms behind this phenomenon. The physical processes involved are the center of interest. To increase the knowledge in this field one need to study the effects of different parameters

such as lithology, pore fluid saturation and frequency on attenuation, and through these studies identify the processes causing the absorption.

Numerous absorption mechanisms have been proposed. In particular:

- Matrix anelasticity, including frictional dissipation due to relative motions at the grain boundaries and across surfaces.

- Attenuation due to fluid flow, including relaxation due to shear motions at pore-fluid boundaries.

- Dissipation in a fully saturated rock due to the relative motion of the frame with respect to fluid inclusions.

- Squirting phenomena (squirt flow).

- Partial saturation effects such as gas pocket squeezing.

- Energy absorbed in systems undergoing phase changes.

- And a large category of geometrical effects, including scattering by small pores and large irregularities and selective reflection from thin beds.

In the following some of these mechanisms will be presented further.

2.5.1   Attenuation due to fluid flow

There is a general agreement on the fact that rocks containing pore fluids generate a larger amount of attenuation than dry rocks. But there is so far no agreement on the mechanisms responsible for this effect. Several theories concerning this has been proposed;

- THE EFFECTS OF WETTING ON GRAIN BOUNDARY FRICTION.
  Laboratory work shows that due to low saturations the value of Q is drastically reduced. It is believed that this is caused by a wetting effect, which is a possible reaction between the water entering the fine cracks and the granular material causing the rock to soften. This lubrication of cracks makes it easier for frictional sliding to occur, and therefore increase attenuation (Johnston et al., 1979).
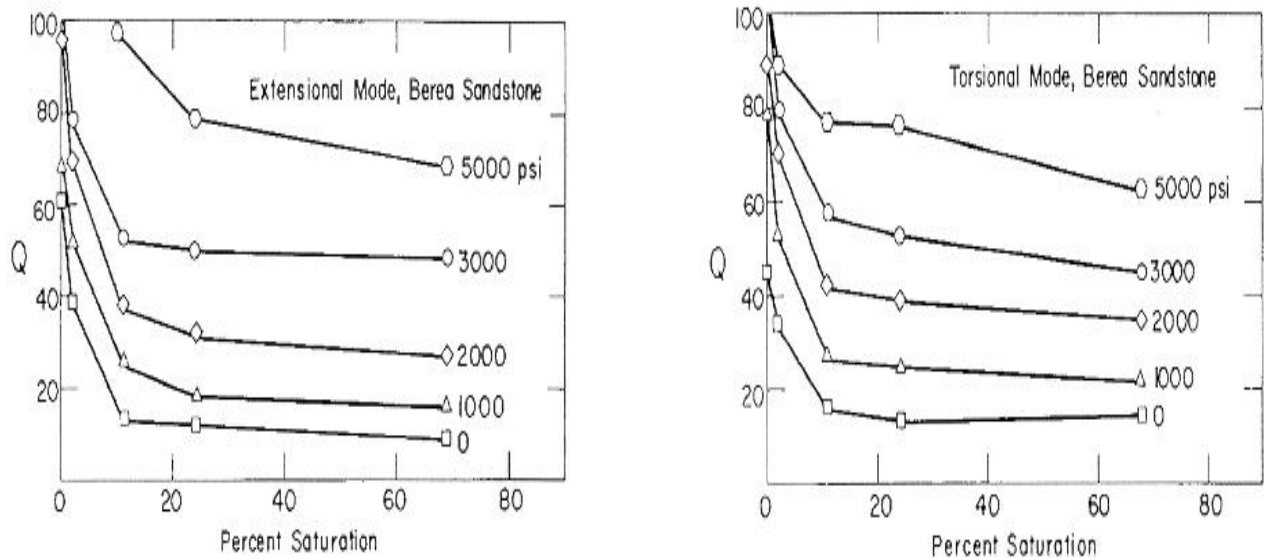
Figure 2.4: *This figure shows Q as a function of saturation and differential pressure in Berea sandstone. Extensional mode is given in the figure on the left hand side, while torsional mode is given one on the right hand side (Johnston et al., 1979).*

- MACROSCOPIC FLUID FLOW.

  A measure of the macroscopic fluid flow gives the average relative movement between all fluid particles and all 'solid' particles, illustrated in figure 2.5. Let the two vectors u and U denote the movement of the solid grains and the pore fluid. The different movement these two components has, implies a difference in the connection between stress and strain.

  Biot (1956a, 1956b) developed a microscopic theory to attempt to model the behavior of fluid-saturated poro elastic systems. His model was based on the assumption of having an acoustic wave propagation in a homogeneous, isotropic, porous and permeable rock which is saturated with fluid. The wave traveling through the rock will lose its energy due to the relative motion between the solid and the inclusions filled with fluid. Biot's definition of macroscopic fluid flow coincide with the definition above. The observation of how the average particle movement of the solid grains and the pore fluid might differ from each other is known as *Biot's phenomenological observation* (Johansen, 1997). A more detailed summary of Biot's theory is to be found in Appendix A.
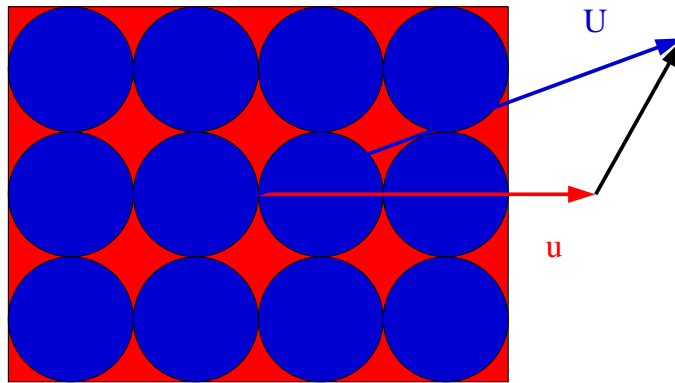
Figure 2.5: *Macroscopic fluid flow is defined as the relative movement between the particles of the solid, and the particles of the fluid (Johansen, 1997).*

- MICROSCOPIC (SQUIRT) FLUID FLOW. This kind of fluid flow will occur whenever there are adjacent and connected volumes containing a fluid exposed to different deformation. The uneven ratios of pressure causes the fluid to flow from high pressure zones into zones of low pressure. In this case it is common to distinguish between *intercrack flow* and *intracrack flow* (figure 2.6).

  Intercrack flow denotes a fluid flow between pores. This phenomenon comes to pass whenever fully saturated cracks are compressed. It might occur in various degree depending on the shape and orientation of the crack. Intracrack flow, on the other hand, denotes an internal fluid flow within the pore itself. Opposed to intercrack flow, intracrack flow occurs in partially saturated cracks when exposed to compression. The compression causes the liquid to flow into gas filled regions within the pore. Seismic frequencies are considerably attenuated during this occurrence. These two mechanisms of fluid flow are often referred to as *squirt-flow phenomena.*

  It is a difficult task to try to estimate the attenuation due to intercrack fluid flow, because this mechanism is very sensitive to unknown details as the micro structure. This is because the deformation caused by a propagating seismic wave is dependent on the shape and orientation of the pore/crack. How these variations affect the attenuation due to compression has been an area of interest for many researchers. Johnston et al. (1979) based their research on a model giving fluid flow between flat cracks and more equi-dimensional pores. This model predicts more bulk compressional at-

tenuation than shear attenuation, when a random orientation of cracks is assumed. O'Connell & Budiansky (1977) used a model where the fluid would flow between thin cracks. Their results showed exactly the opposite of Johnston et al. (1979). They found that shear attenuation is larger than bulk compressional attenuation. By assuming cracks of identical shape or infinitely thin, the bulk attenuation can be made zero. Due to this wide range of possible predictions, intercrack flow can be made to fit the data, but no unique prediction can be made. Winkler & Nur (1982) used a sample of Massilon sandstone exposed to waves in the kHz-domain. They conclude that under the conditions of their experiments, intercrack flow is a more significant source of seismic attenuation than Biot-type flow. They also state that the observation of $Q_p^{-1}/Q_s^{-1} < 1$ may imply that 'crack-to-crack' flow dominates over 'crack-to-pore' flow.
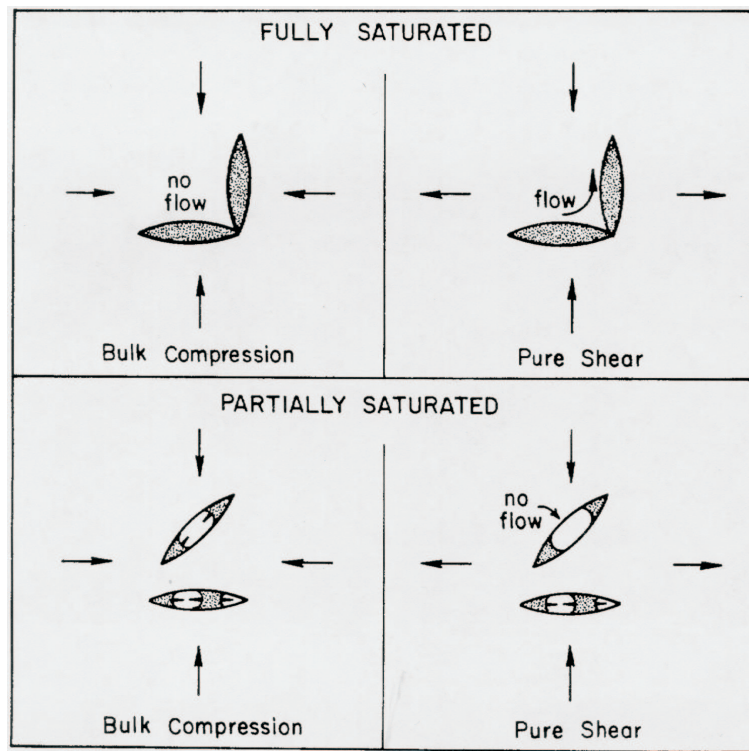
Figure 2.6: *This is a conceptual model showing pore fluid attenuation mechanisms involving microscopic fluid flow. On top; the illustration of intercrack flow, while intracrack flow is illustrated at the bottom (Winkler & Nur, 1982) .*

Intracrack fluid flow occurs, as mentioned above, in partially saturated rock.

And attenuation in partially saturated rock is significantly different from that in fully saturated rock. When a partially saturated crack is exposed to compression the liquid will flow into volumes occupied by gas, causing viscous energy losses for both seismic and sonic frequencies. When exposed to bulk compression every crack will be compressed and contribute to the attenuation. For pure shear compression however, not every crack will be compressed. This is due to the fact that some cracks will be oriented so that there is no normal stress on the crack faces. These cracks will not be compressed, and therefore not contribute to the attenuation (Fig. 2.6). According to Winkler & Nur (1982) bulk compressional (and P-wave) attenuation is much larger in partially saturated than in fully saturated rock. And P-waves are also attenuated stronger than S-waves in partially saturated rock, whereas the reverse is the case in fully saturated rock.

- THERMOELASTIC EFFECTS.
  This model is based on Zener's work from 1938 (Zener, 1938). He found that the vibration of stress inhomogeneities in a vibrating body results in fluctuations in temperature, and further on to local heat currents. This process will give a decrease in attenuation with increasing pressure. This theory also predicts an increase in Q for low frequencies. Armstrong (1980) and Kjartansson (1979a) has also done research on this topic. Armstrong agrees with the findings of Zener, while he also further explores more complex solid models. Kjartansson's discoveries indicate that compressional waves are more affected by this mechanism than shear waves. That this observation is very sensitive to the characteristics of the pore fluids is also one of Kjartansson's conclusions. Especially large losses are expected when small amounts of gas are introduced into an otherwise liquid-saturated rock. They all agree on the fact that thermoelastic effects are strongly dependent on temperatures, especially those ¿ 150°C. Even though all three agree on the basics of this mechanism, this is still regarded as an area that, up until now, lacks experimental work to support these findings.
  It is difficult to predict the magnitude thermoelastic effects has on the total attenuation. This is stated by Winkler & Nur (1982) who say that it is possible that both fluid flow and thermoelastic effects contributes to the total energy loss, and that it might be difficult to determine their relative

importance.

- Viscous shear relaxation.

  The fluid flow within and between different pores is dependent on the nor-
  mal stresses on the pore plane. Enforced shear stresses may also however
  induce motion in the pore fluid. Shear stresses in the pore plane causes
  oscillations of the pore walls (relaxation). This leads to a relative motion
  between the matrix and the fluid. Maximum attenuation will occur at cer-
  tain frequencies, depending on the aspect ratio and viscosity. O'Connell &
  Budiansky (1977) found that there will be maximum attenuation caused by
  shear relaxation in an isolated, fully saturated crack at a certain frequency.
  This characteristic frequency for the relaxation of shear stress in the viscous
  fluid in the crack is given by the following equation;

$$\omega = (G/\eta)\,(c/a)\,, \qquad\qquad (2.23)$$

  where G is a moduli for the uncracked solid, η is the fluid viscosity, and c/a
  is the aspect (thickness to diameter) ratio of an oblate spheroidal crack.
  Viscous shear relaxation is assumed to be of little importance for both
  fully water saturated (O'Connell & Budiansky, 1977), and partly water
  saturated (Mavko & Nur, 1979) rocks at seismic and sonic frequencies. But
  the mechanism may be significant at MHz-frequencies or for frequencies
  within the kHz area in rocks containing more viscous pore fluids.

- Flow between macroscopic regions of total and partial sat-
  uration.

  White (1975) came up with a model to explain attenuation in inhomoge-
  neous porous rocks. He bases his theory on the assumption that the dimen-
  sions of the inhomogeneities are small compared to the wavelength of the
  seismic wave, but much larger than the grains. These inhomogeneities are
  gas-filled spherical regions in an otherwise brine-filled rock. White showed
  that a compressional wave passing through such a composite medium can
  induce a rather large fluid flow near the inhomogeneities. This results in a
  considerable loss of energy due to the viscosity of the denser fluid.
  Dutta & Od (1979a, 1979b) investigated this model. But they removed
  several of White's dubious approximations, and examined their effects on

the quantitative results. Their results are in reasonably good agreement with White's approximate theory.

2.5.2 Attenuation due to scattering

Per definition scattering is the irregular and diffuse dispersion of energy caused by inhomogeneities in the medium through which the energy is traveling (Sheriff, 1999). This means that scattering is a purely geometrical effect, and not dependent on intrinsic rock properties.

This kind of attenuation is dependent on frequency. Rewriting equation 2.19, and the attenuation coefficient is expressed by $\alpha = \pi f / QV$. This coefficient resulting from elastic scattering is dependent on the seismic wavelength, λ, and on the diameter, d_s, of the scattering heterogeneity. This is divided into three domains (Mavko et al., 1998):

- Rayleigh scattering, where $\lambda > d_s$ and $\alpha \propto d_s^3 f^4$

- Stochastic/Mie scattering, where $\lambda \approx d_s$ and $\alpha \propto d_s f^2$

- Diffusion scattering, where $\lambda < d_s$ and $\alpha \propto 1/d_s$

These domains are illustrated in figure 2.7.

The scattering effects can be neglected if $\lambda \gg d_s$, since the heterogeneous medium in this case behaves like an effective homogeneous medium. And on the other hand, if $\lambda \ll d_s$, the heterogeneous medium may be treated as a piecewise homogeneous medium.

The phase velocity is non-dispersive at very long wavelengths ($\lambda \gg d_s$), and it is close to the static effective medium result seen in figure 2.7. As the frequency increases (decrease in wavelength) there will be a velocity dispersion caused by scattering. In the Rayleigh scattering domain ($\lambda/d_s \approx 2\pi$), the velocity shows a slight decrease with increasing frequency. As illustrated by the figure, this is followed by a rapid and much larger increase in phase velocity owing to resonant (or Mie) scattering ($\lambda \approx d_s$).

The concentration, shapes and physical properties of the inhomogeneities in a medium are important parameters to consider when calculating the attenuation
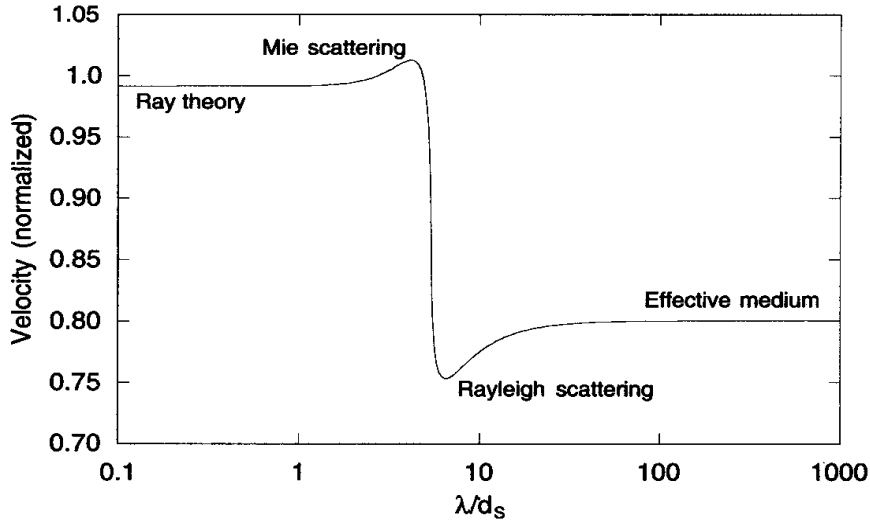
Figure 2.7: *The general frequency dependence of wave velocity that is expected due to scattering in a heterogeneous media (Mavko et al., 1998).*

caused by scattering. According to Kuster & Toksz (1974) a concentration of a fraction of one percent of thin (small aspect ratio) inclusions could affect the compressional and shear velocities by more than ten percent.

2.5.3   Attenuation due to matrix anelasticity

Seismic wave attenuation in a rock matrix can be attributed to two factors :

- intrinsic anelasticity of matrix materials

- frictional dissipation due to relative motions at the grain boundaries and across crack surfaces.

Generally the intrinsic anelasticity of minerals is very small. In individual crystals, Q values are generally higher than a few thousand, while in a rock, Q values are normally lower than a few hundred. Therefore, in considering matrix attenuation, it is responsible to neglect the intrinsic attenuation in minerals and to consider only the attenuation across grain surfaces and thin cracks.

However; friction across crack surfaces can not account for all the anelasticity of

the matrix. Because even though a rock is being subjected to confining pressure that is high enough to close all cracks, it will still possess non-zero attenuation. Meaning that, in addition to dissipation across crack surfaces, it is necessary to consider an intrinsic anelasticity of the aggregate minerals (Johnston et al., 1979).

Exactly how the mechanism of grain boundary and crack dissipation work is not yet know. But according to Walsh (1966), one major factor may be frictional dissipation due to relative motion of the two sides. If this is so, then the attenuation strongly should depend on the surface conditions that affect friction between grains. Whether or not the rocks are saturated, the properties of the saturating fluids, and the amount of clay or other soft components in the matrix are examples of such conditions.

2.6 Different models for the quality factor

That attenuation is a very complex phenomenon is a well stated fact. And it can not be explained by a single model or mechanism. Many of the questions and issues evolved around the mechanisms of attenuation are still unanswered.
The question whether or not the quality factor is dependent on frequency, has in particular been disputed many times. In the following section published results of laboratory data and mathematical deductions treating this issue will be summed up.

2.6.1 Constant Q (CQ)

Constant, or frequency independent, Q implies that the energy loss per argument cycle is independent of the time scale of the oscillation. This is the basis of a linear model for attenuation of waves.
This kind of wave propagation is completely specified by only two parameters; Q and c_0, a phase velocity at an arbitrary reference frequency ω_0. This is why this model is easily described mathematically.

Kjartansson (1979b) reasons that due to the fact that a constant Q model implies a time independent energy loss, it would be logical to try a material that has a

creep function that plots a straight line on a log-log plot, or

$$\Psi(t) = \frac{1}{M_0 \Gamma(1 + 2\gamma)} \left(\frac{t}{t_0}\right)^{2\gamma} \quad t > 0, \tag{2.24}$$

$$\Psi(t) = 0 \quad t < 0, \tag{2.25}$$

where Γ is the gamma function which has a value close to unity, t_0 is an arbitrary reference time introduced so that when t has a dimension of time, and M_0 will have the dimension of modulus.

By taking the Fourier transform;

$$S(\omega) = \frac{1}{M_0} \left(\frac{i\omega}{\omega_0}\right)^{-2\gamma}, \tag{2.26}$$

$$\omega_0 = \frac{1}{t_0}, \tag{2.27}$$

and by using

$$1 = M(\omega) S(\omega), \tag{2.28}$$

it may result in the expression:

$$M(\omega) = M_0 \left(\frac{i\omega}{\omega_0}\right)^{2\gamma} = M_0 \left|\frac{\omega}{\omega_0}\right|^{2\gamma} e^{i\pi sgn(\omega)}, \tag{2.29}$$

where

$$sgn(\omega) = 1, \quad \omega > 0 \tag{2.30}$$

$$sgn(\omega) = -1, \quad \omega < 0. \tag{2.31}$$

$M(\omega)$ and $S(\omega)$ are the Fourier transforms of $m(t)$ and $s(t)$, two real functions used to express stress and strain ($\sigma(t) = m(t) * e(t)$ and $e(t) = s(t) * \sigma(t)$).

Equation 2.29 shows that the argument of the modulus and thus the phase angle between the stress and the strain, is independent of frequency; therefore, it follows from the definition of Q, equation 2.13, that Q is independent of frequency:

$$\frac{1}{Q} = \tan(\pi\gamma) \tag{2.32}$$

or

$$\gamma = \frac{1}{\pi} \tan^{-1} \left(\frac{1}{Q} \right) \approx \frac{1}{\pi Q}. \tag{2.33}$$

This approximation is valid when $Q^{-2} \ll 1$ (Kjartansson, 1979a).

Mavko et al. (1998) support Kjartansson's theory by presenting an illustration that shows that attenuation is constant for all frequencies, and that velocities always increase with frequency (figure 2.8).
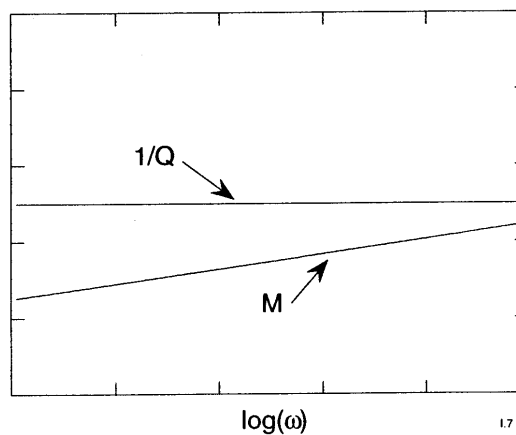
Figure 2.8: *Attenuation is constant for all frequencies, while velocity increases with frequency (Mavko et al., 1998).*

After a study of the Berea sandstone Winkler & Nur (1982) found that, in the interval of 1-9 kHz, Q is independent of frequency when the rock is dry (except for some slight fluctuations in the low pressure shear data). Their findings also coincide with the observations done by Born (1941) and Prandit & Savage (1973). Figure 2.9 shows Winkler & Nur (1982)'s results graphically. The attenuation has been measured at two different confining pressures; $P_c = 5 \cdot 10^5 \, Pa$ and $P_c = 10^7 \, Pa$. Both shear (S) and extensional (E) data are shown.

2.6.2 Nearly constant Q (NCQ)

The nearly constant Q model states that attenuation is nearly constant over a finite range of frequencies.
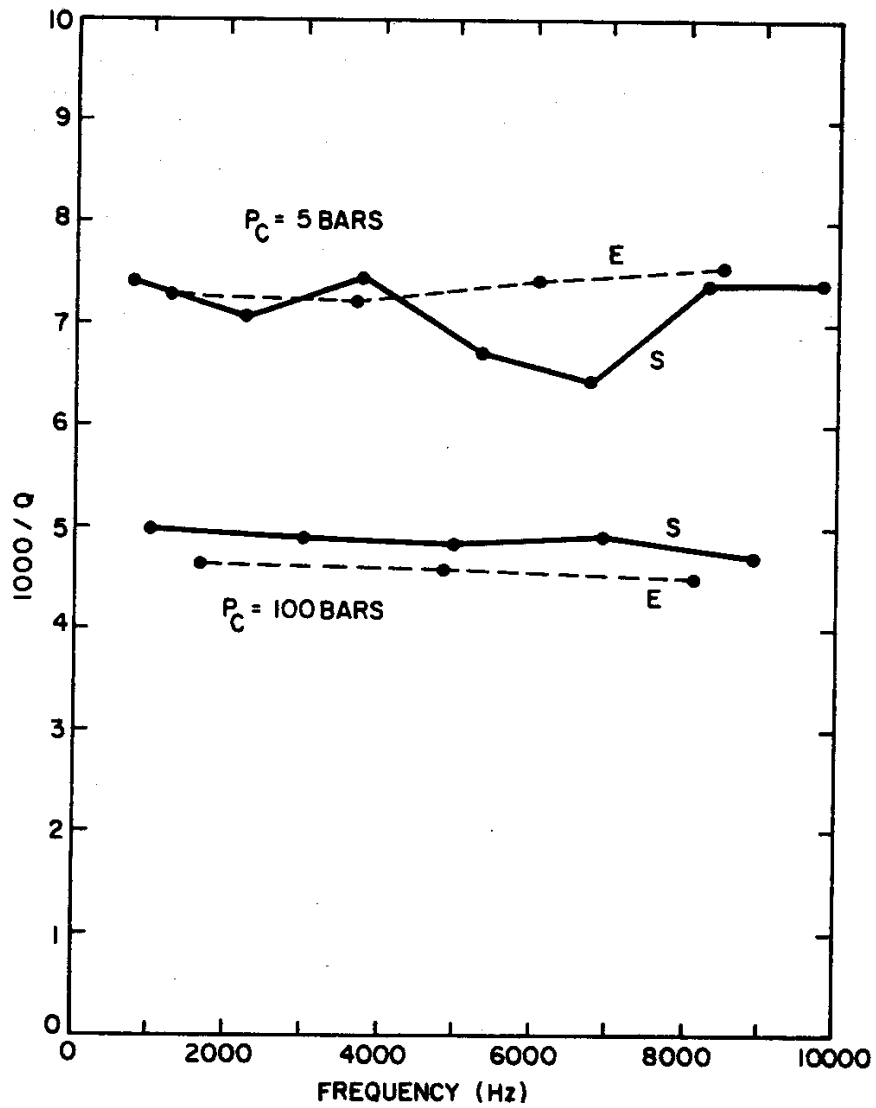
Figure 2.9: *Attenuation as a function of frequency for dry Berea sandstone (Winkler & Nur, 1982).*

Liu et al. (1976) are amongst those who has considered such a model. They used a model in which simple attenuation mechanisms are combined.

Based on their work, it is possible to write:

$$\frac{V(\omega)}{V(\omega_0)} = 1 + \frac{1}{\pi Q} \log\left(\frac{\omega}{\omega_0}\right), \tag{2.34}$$

where $V(\omega)$ and $V(\omega_0)$ are velocities dependent on present and initial frequency respectively. This equation relates the velocity dispersion within the band of constant Q, to the value of Q and the frequency.

$V(\omega)/V(\omega_0)$ can also be written as:

$$\frac{V(\omega)}{V(\omega_0)} = \frac{\sqrt{M_0 + \Delta M}}{\sqrt{M_0}} = \sqrt{1 + \frac{\Delta M}{M_0}}. \tag{2.35}$$

Expanding for small $\Delta M/M$, and by substitution in equation 2.34, the attenuation can be expressed by:

$$\frac{1}{2}\frac{\Delta M}{M_0} \approx \frac{1}{\pi Q} \log\left(\frac{\omega}{\omega_0}\right), \tag{2.36}$$

$$\frac{1}{Q} \approx \frac{\pi}{\log\left(\frac{\omega}{\omega_0}\right)} \left(\frac{1}{2}\frac{\Delta M}{M_0}\right). \tag{2.37}$$

Nearly constant attenuation is in some cases interpreted as a superposition of individual (Standard Linear Solid) attenuation peaks (Mavko et al., 1998). This means that a broadening of the attenuation peak is accompanied by a broadening of the range of frequency where velocity increases. This is illustrated in figure 2.10.

As mentioned earlier Winkler & Nur (1982) performed a thorough study of Berea sandstone. As a part of these studies the shear attenuation for water-saturated rock at various frequencies was measured. The results showed a strong frequency dependence of Q, unlike what was found in dry rock. Figure 2.11 illustrates these findings, and the data used are taken at high confining pressure and various pore pressures. The results found for saturated Berea sandstone, is also consistent with the observations of Born (1941).
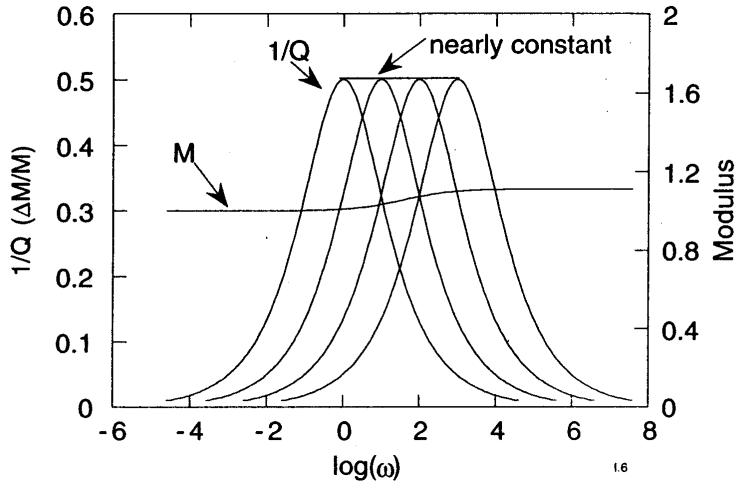
Figure 2.10: *Attenuation is nearly constant over a finite range of frequencies (Mavko et al., 1998)*

2.7   Seismic resolution

Seismic resolution is per definition the ability to separate two, or more, features which are close together. The minimum separation of two bodies before their individual identities are lost on the resultant map or cross-section (Sheriff, 1999). How accurate details can be obtained in a seismic survey, is highly dependent on the degree of seismic resolution. And to specify this term, seismic resolution is considered as either *vertical* or *horizontal* resolution.

2.7.1   Vertical Resolution

Vertical resolution can be considered as the minimum resolvable bed thickness. Normally two criteria are used to define this limit (Sheriff, 1999):

- The Rayleigh resolution limit: the minimum separation so that one can ascertain that more than one interface is involved is $\lambda/4$, where λ is the dominant wavelength (the dominant wavelength is that of the dominant frequency in the interval velocity V_p). This is called tuning thickness (2.12).

- The Widess limit: the minimum separation is $\lambda/8$.
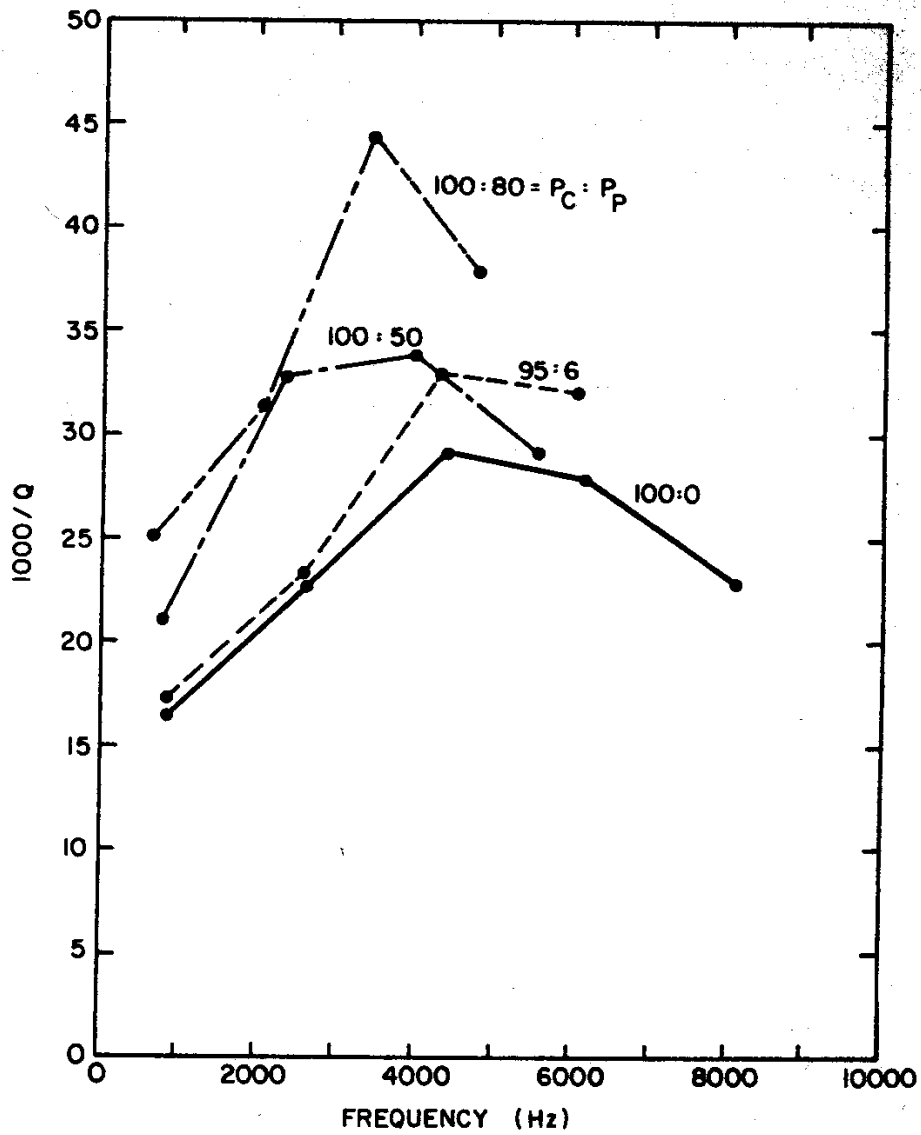
Figure 2.11: *Shear attenuation as a function of frequency for saturated Berea sandstone (Winkler & Nur, 1982).*
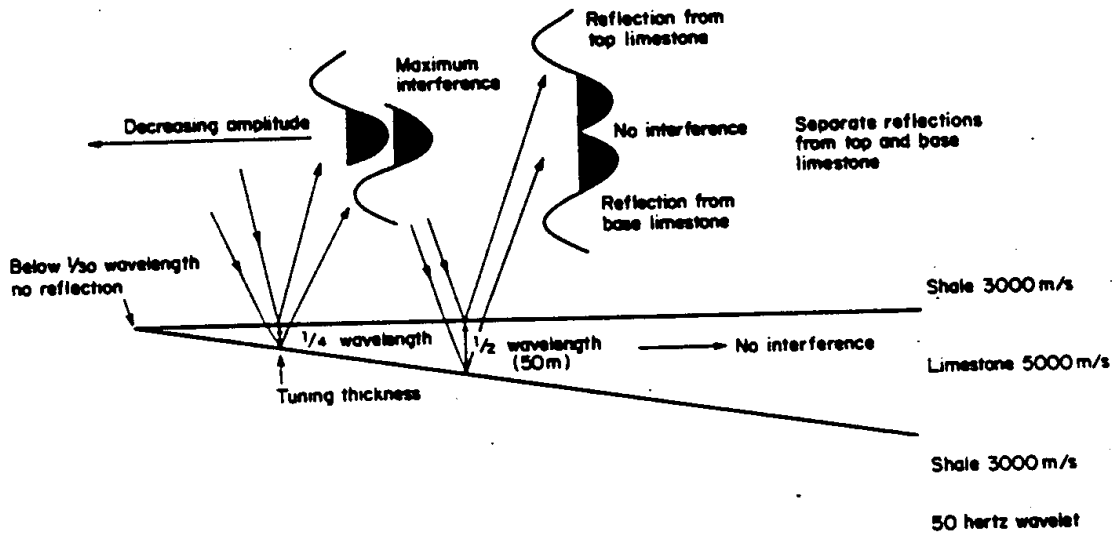
Figure 2.12: *An illustration of the effects of interference. When the layer has a thickness of $1/4\,\lambda$, (tuning thickness) the reflection of the top and the bottom will interfere constructively, and together form one single wave with abnormally high amplitude. If the wavelength is smaller than this, it will not be possible to separate the two reflectors at all.*
If the layer has a thickness of $1/2\,\lambda$, the reflection from the bottom will be of reversed polarity from that from the top. These will be separated in time, and therefore tell apart.
Wavelengths between the two mentioned, will cause the reflections to overlap, and interfere. (Sundvor, 1989)

According to Widmaier (1999), the Rayleigh resolution limit is based on the assumption that there must be a separation of at least $\lambda/2$ between the top and the bottom interface of a thin layer in order to avoid destructive interference between the two reflected signals.

This can also be expressed as a function of time. By using that time delay equals the two-way traveltime through the thin layer thickness, d, the mathematical basis will be:

$$\Delta t = 2 \left(\frac{d}{V_p} \right). \tag{2.38}$$

Per definition of the criteria, the time delay between top and bottom reflection must be larger that $T/2$, where T is the time period of the signal;

$$\frac{T}{2} < \Delta t = 2 \left(\frac{d}{V_p} \right). \tag{2.39}$$

In order to be resolved by P-waves, and by using that $T = 1/f$, the equation for the thickness d, becomes

$$d > \left(\frac{1}{4f} \right) V_p. \tag{2.40}$$

And further, by using the the equation for velocity, $V_p = \lambda_p f$, equation 2.40 can be written as

$$d > \frac{\lambda_p}{4}. \tag{2.41}$$

This mathematical deduction is only valid for PP-reflections (the incident P-wave is reflected as a P-wave).

In the case of PS-wave converted reflections the corresponding resolution limit will be somewhat different. By ignoring the fact the physically, for normal incidence, PS reflections do not exist, and by applying equation 2.38, the mathematical basis in this case is

$$\Delta t = \frac{d}{V_p} + \frac{d}{V_s} = d \left(\frac{V_p + V_s}{V_p V_s} \right). \tag{2.42}$$

As done in the PP case, the $T/2$ requirement is introduced, and the resolution limit for PS converted waves is

$$d > \frac{1}{2f} \left(\frac{V_p V_s}{V_p + V_s} \right). \tag{2.43}$$

Converted into a function of wavelengths, equation 2.43 becomes;

$$d > \frac{1}{2}\left(\frac{\lambda_p \lambda_s}{\lambda_p + \lambda_s}\right). \tag{2.44}$$

An interesting aspect of vertical resolution is to reveal whether PP or PS converted waves gives the best resolution. Considering the deductions done above, and by assuming the same dominant frequency, the resolution limits for PP and PS can be combined as follows;

$$d_{PS} = \frac{1}{2f}\left(\frac{V_p V_s}{V_p + V_s}\right) = \frac{1}{2f}V_p\left(\frac{1}{1 + V_p/V_s}\right) = \frac{2}{1 + V_p/V_s}d_{PP}. \tag{2.45}$$

According to this equation PS converted waves are able to resolve thinner layers than PP waves. The V_p/V_s ratio controls the resolution power of PS waves relative to P waves. The general trend is that vertical PS resolution improves with increasing V_p/V_s.

The presence of attenuation has not been considered in the deductions done above. At shallow targets, before the attenuation becomes significant, the conclusion that PS converted waves has a better resolution than PP waves is often correct. But at a certain depth, when $Q_p > Q_s$, there will be a so called *resolution crossover depth*. At this depth, the PP waves will possess a better resolution ability than that of the PS waves.

Deffenbaugh et al. (2000) found an equation expressing the crossover depth, z_c;

$$z_c = \Delta T_0 Q_s Q_p \left(\frac{V_p - V_s}{Q_p - Q_s}\right), \tag{2.46}$$

where ΔT_0 is the duration of the initial wavelet.

Their conclusion is that for near offsets, the crossover depth is the same for both vertical and horizontal resolution.

Another interesting aspect of seismic resolution, is what kind of waves that would give the best resolution through a gas-cloud. As discussed under section 2.5, seismic waves will be attenuated considerably when passing through a media containing liquid. Considering the two different types of waves separately, the P-waves will lose their energy faster than the S-waves. This is due to the fact

that the P-waves give a change in volume, which will create a fluid flow, and therefore be attenuated as described earlier. The S-waves on the other hand, involve shearing and rotation, which creates very little fluid flow. The attenuation of this kind of wave is therefore a lot smaller.

Regarding a wave passing through a medium filled with liquid, being reflected at the bottom interface, before returning up through the same medium, it is clear that the amount of energy lost depends on the type of wave used. A PP-wave will lose the most energy, since it will be strongly attenuated due to the fluids both before and after the reflection point. PS-waves will also lose energy due to the large attenuation it is exposed to as a P-wave. But not as much as a PP-wave, since it travel as a S-wave upwards, meaning less attenuation. A SS-wave will lose the least energy, and therefore formally give the best resolution.

A further discussion of this topic will be done in chapter 5.

2.7.2 Horizontal resolution

Historically, vertical resolution has been the main focus when discussing seismic resolution. The ability to "resolve" two reflectors with close vertical spacing has been of particular interest for most analysis. However, resolution is most completely understood when it is regarded in a three-dimensional sense. Meaning that horizontal resolution must also be considered.

Horizontal resolution is dependent on *the Fresnel zone*. When defining the Fresnel zone, it is important to keep in mind that a wave propagates spherically, and not as a ray from one point to the next. This means that the reflection does not come from a point, but must be generated by integration over an area. It is this area which is termed "the Fresnel zone" (figure 2.13).

How large this area is establishes the horizontal resolving power of the seismic method. The size is moreover dependent on frequency.

A point of observation on the surface receives reflection energy from the flat planar reflector in an area surrounding the reflection "point". The limit of constructively interfering reflection elements is defined as the loci away from the reflection area centroid where the increase in path length is a defined amount.

According to Sheriff (1980), the increase is $1/4\,\lambda$, causing these remote reflection
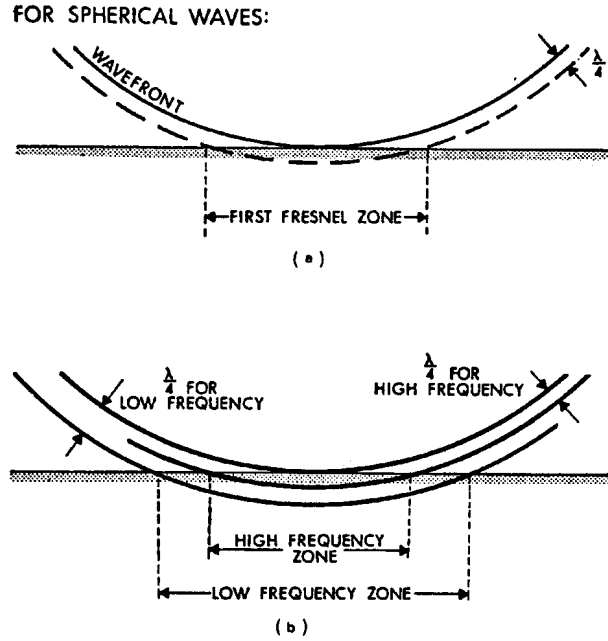
Figure 2.13: *An illustration of the term "Fresnel zone", and its variations with frequency (Simm, 2001).*

elements to be $1/2\,\lambda$ out of timing. Based on this he defines the Fresnel zone as follows;

$$F_{Sheriff} = 2\sqrt{(z + \lambda/4)^2 - z^2}. \tag{2.47}$$

Berkhout (1984), on the other hand, suggest that the limits of constructive interference be defined where the outer-zone path length is $1/8\,\lambda$ longer since this would cause the two-way arrival time to be $1/4\,\lambda$ later that that of the centroid path. A $1/4\,\lambda$ criterion corresponds to the point of transitioning from constructive to destructive interference with the energy from the centroid (or reflection) path length. Berkhout's definition of the Fresnel zone is therefore:

$$F_{Berkhout} = 2\sqrt{(z + \lambda/8)^2 - z^2}. \tag{2.48}$$

z denotes the depth in both formulas.
It is not of prevailing importance as to which criterion is used.

From the equations it is easy to see that the Fresnel zone is larger for low frequencies than for high frequencies. This can also be seen in figure 2.13.

2.8 Chapter summary

In the opening of this chapter, a brief sum up of the most important principle evolving elasticity versus inelasticity in a material is presented. This is followed by a presentation of the two kinds of body waves; P- and S-waves.
This is just a short presentation, to set the theoretical foundation.

A thorough description of the two attenuation parameters; the attenuation coefficient, α, and the quality factor, Q, is done in the following. Emphasis has been put on the Q-factor since this is the parameter used to measure attenuation in the remaining parts of this thesis. As one can see in this part, there are several ways to define the Q-factor, depending on ones focus.
Different ways to express the attenuation ratio between Q_p and Q_s is also sketched out.

To achieve a better understanding of the attenuating processes, a complementing description of different mechanisms is made. Only the most important mechanisms are described here, but many are mentioned. Various aspects concerning the effect of fluid flow is presented, since this is regarded as one of the most important contributors to attenuation of seismic waves.
The effects of scattering is also considered cause to a large part of the loss of energy; and more than matrix anelasticity.

A massive discussion whether or not the quality factor is frequency dependent has been going on for a long period of time. At the early stage of laboratory work, it was assumed that the Q-factor was independent of frequency. They used a constant Q-model. But through further research frequency dependent theories were put forward. A few of the results from experiments, together with mathematical deductions are presented in this chapter. As a rough conclusion, it seems as if there is a common conviction that for dry rocks, Q is independent of frequency. But as soon as saturation of a fluid is present in the rock, it becomes dependent of frequency.

Vertical and horizontal resolution is also sketched out, and it is important to see that these to go hand in hand. To get a good idea of the resolution level, one need to consider them both.
In this section it is stated that PS-waves has the best resolution at shallow depths.

But at a certain depth, the crossover depth the PP-waves gives the best resolution; when $Q_p > Q_s$.

But for waves propagating through a gas-cloud PS-waves would give better resolution than PP-waves. Theoretically SS-waves would give the best resolution. This topic will be discussed further in chapter 5.

Chapter 3

Seismic wave propagation in attenuating materials

3.1 Introduction

This chapter is meant as an introduction to the basics of wave propagation in a medium. These principles are founded on the theory of stress and strain presented in the previous chapter.

The equation of motion is given, which leads to the deduction of the seismic wave equation.
Snell's law is further used as a base for the understanding of reflection and transmission coefficients given by Zoeppritz equations.
Finally, a summary of the principles of the software Nucleus used for the modeling of this thesis. The main focus is kept on the equations defining the wave propagation for the models generated by this program.

3.2 The equation of motion

In the previous chapter, the definitions of stress and strain were introduced. These were considered in static equilibrium and unchanging with time.
But seismic waves are a time-dependent phenomenon that involve velocities and

accelerations. Newton's law ($F = ma$) is therefore applied on to a continuous medium.

Consider the forces on an infinitesmall cube in a (x_1, x_2, x_3) coordinate system (figure 3.1).The forces on each surface on the cube are given by the product of the traction vector and the surface area.
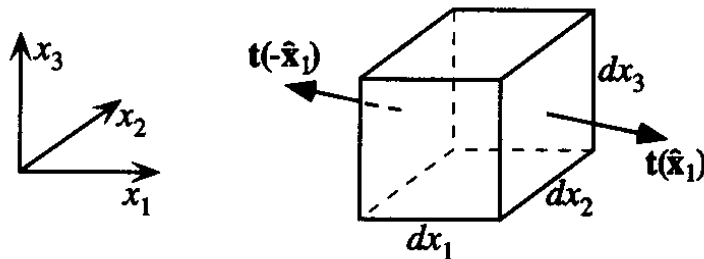
Figure 3.1: *The force on the (x_2, x_3) face of an infinitesmal cube is given by* ***t(*$\widehat{x}_1$*)****$dx_2 dx_3$**, *the product of the traction vector and the surface area.*

By combining the equations for these forces given by the traction vector **t**, the stress tensor τ, and the displacement **u,** with Newton's law gives the *equation of motion* for a continuum;

$$\rho\frac{\partial^2 u_i}{\partial t^2} = \partial_j \tau_{ij} + f_i, \tag{3.1}$$

where ρ is the density and f is the body force (Lay & Wallace, 1995).
This is the most fundamental equation underlying the theory of seismology, as it relates forces to the medium to measurable displacements.

Gravity is an important factor at very low frequencies in normal mode seismology, but it can generally be neglected for body- and surface-wave calculations at typically observed wavelengths.

In the absence of body forces, we have *the homogeneous equation of motion*;

$$\rho\frac{\partial^2 u_i}{\partial t^2} = \partial_j \tau_{ij}, \tag{3.2}$$

which governs seismic wave propagation outside the source regions.

3.3 The seismic wave equation

In order to solve equation 3.2, the relationship between stress and strain defined in equation 2.3 is required, so that the stress tensor τ can be expressed by the displacement $\mathbf{u}$.

To illustrate the following deduction, equation 2.3 is hereby repeated;

$$\tau_{ij} = \lambda \delta_{ij} e_{kk} + 2\mu e_{ij} \tag{3.3}$$

The strain tensor is defined as

$$e_{ij} = \frac{1}{2} \left(\partial_i u_j + \partial_j u_i \right). \tag{3.4}$$

Substituting for e_{ij} in equation 3.3 gives

$$\tau_{ij} = \lambda \delta_{ij} \partial_k u_k + \mu \left(\partial_i u_j + \partial_j u_i \right). \tag{3.5}$$

By substituting equation 3.5 into 3.2, and by defining $\hat{\mathbf{u}} = \partial^2 \mathbf{u}/\partial t^2$, the following equation is obtained;

$$\rho \hat{\mathbf{u}} = \nabla \lambda \left(\nabla \cdot \mathbf{u} \right) + \nabla \mu \cdot \left[\nabla \mathbf{u} + (\nabla \mathbf{u})^T \right] + (\lambda + \mu) \nabla \nabla \cdot \mathbf{u} + \mu \nabla^2 \mathbf{u}. \tag{3.6}$$

By using the vector identity $\nabla \times \nabla \times \mathbf{u} = \nabla \nabla \cdot \mathbf{u} - \nabla^2 \mathbf{u}$, and by ignoring the gradient terms, the momentum equation for homogeneous media becomes (Shearer, 1999);

$$\rho \hat{\mathbf{u}} = (\lambda + 2\mu) \nabla \nabla \cdot \mathbf{u} - \mu \nabla \times \nabla \times \mathbf{u}. \tag{3.7}$$

This is the standard form for *the seismic wave equation* in homogeneous media and forms the basis for most body wave synthetic seismogram methods.

However, its important to remember that it is an approximate expression, which has neglected the gravity and velocity gradient terms and has assumed a linear, isotropic earth model.

3.4   Reflection and refraction

3.4.1   Snell's law

A wavefront is defined as the surface over which the phase of a traveling wave disturbance is the same. The wavefront moves perpendicular to itself as the disturbance travels in an isotropic medium.
Body waves traveling through an isotropic medium propagates spherically, meaning that the wavefront spreads like a spherical surface around the source.
If the distance is large enough, one can consider a sector of the wavefront as a plane surface, and the wave can therefore be regarded as a plane wave.

The propagation of seismic waves are analogous to the propagation of sound and light waves.
The energy of the waves are reflected and transmitted at discontinuity caused by differences in acoustic impedance ($V \times \rho$) related to lithological changes.
When a wave crosses over such a boundary, the wave changes direction such that

$$\frac{\sin i}{V_i} = \frac{\sin \theta_{p1}}{V_{p1}} = \frac{\sin \theta_{s1}}{V_{s1}} = \frac{\sin \theta_{p2}}{V_{p2}} = \frac{\sin \theta_{s2}}{V_{s2}} = p, \tag{3.8}$$

where i is the angle of the incident wave with a velocity $V_i = V_{p1}$ if a P-wave, or $V_i = V_{s1}$ if an S-wave. θ_{p1} and θ_{s1} are the angles of reflection of the P- and S-waves in medium 1, which have velocities V_{p1} and V_{s1}, respectively. θ_{p2} and θ_{s2} are the angles of refraction of the P- and S-waves in medium 2 which have velocities V_{p2} and V_{s2}, respectively. p is the raypath parameter (see figure 3.2).

3.4.2   Reflection and transmission coefficients

In the general case for an interface between two solids, when the incident angle is not zero, four waves are generated; reflected P- and S-waves, and transmitted P- and S-waves.
The partition of energy at the boundary is given by Snell's law (eq. 3.8).

For an incident P-wave the reflection coefficient $R_{pp}(\theta_1)$ is defined as the ratio of the amplitude of the displacement of a reflected wave to that of the incident wave, while the transmission coefficient $T_{pp}(\theta_1)$ is the ratio of the amplitude of
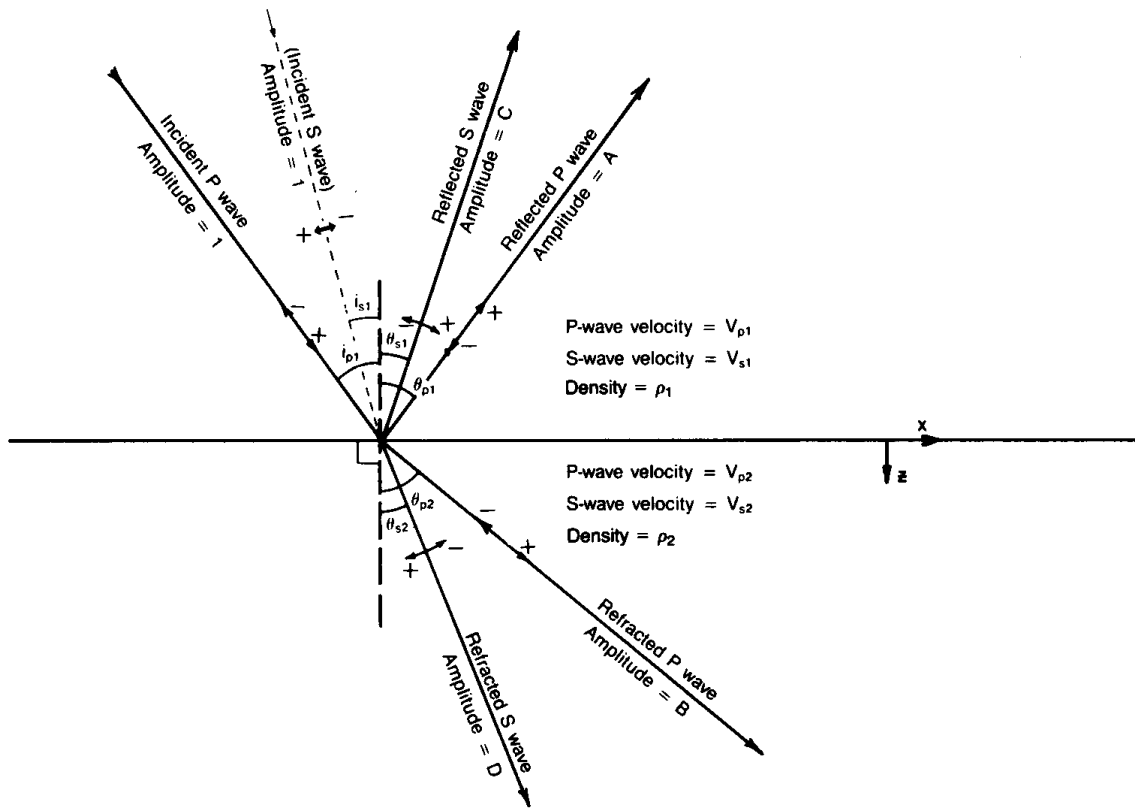
Figure 3.2: *Snell's law relations for either incident P- or S-wave:* $V_i/\sin i = V_{p1}/\sin \theta_{p1} = V_{s1}/\sin \theta_{s1} = V_{p2}/\sin \theta_{p2} = V_{s2}/\sin \theta_{s2} = 1/p$, *where p is the ray parameter (Sheriff, 1999).*

a wave transmitted through an interface to that of the wave upon it. Equivalent definitions are given for the mode converted waves; R_{ps} and T_{ps}.

The shear modulus for a normal incident P-wave in the zx plane equals zero ($\sigma_{ij} = 0\ for\ i \neq j$).This causes zero deformation in the xy nor the yz plane, making a conversion from P-waves to S-waves at the interface impossible.

The reflection coefficient for a normal incident P-wave is (Torgersen, 1999)

$$R_p = \frac{\rho_2 V_{p2} - \rho_1 V_{p1}}{\rho_2 V_{p2} + \rho_1 V_{p1}}. \tag{3.9}$$

The notation $_1$ and $_2$ indicate the layer above, and the layer underneath the interface, respectively.

The transmission coefficient for a normal incident P-wave is

$$T_p = 1 - R_p = \frac{(\rho_1 V_{p1})^2}{\rho_2 V_{p2} + \rho_1 V_{p1}}. \tag{3.10}$$

With increasing offsets there will also be an increase in the angle of incidence. Thus the incident P-wave acquire shear modulus, which causes the wave to convert into both reflected and transmitted S-waves. This conversion is a function of the angle of incident, meaning the the reflection and transmission coefficients also are a function of the incident angle. These variations with angle of incidence are often referred to as *offset-dependent reflectivity*, or AVO (Amplitude Versus Offset).

The reflection coefficients are defined by the Zoeppritz equations (Waters, 1981):

$$
\begin{bmatrix}
\sin\theta_{p1} & \cos\theta_{s1} & -\sin\theta_{p2} & \cos\theta_{s2} \\
-\cos\theta_{p1} & \sin\theta_{s1} & -\cos\theta_{p2} & -\sin\theta_{s2} \\
\sin 2\theta_{p1} & \frac{V_{p1}}{V_{s1}}\cos 2\theta_{s1} & \frac{\rho_2 V_{s2}^2 V_{p1}}{\rho_1 V_{s1}^2 V_{p2}}\sin 2\theta_{p2} & -\frac{\rho_2 V_{s2} V_{p1}}{\rho_1 V_{s1}^2}\cos 2\theta_{s2} \\
\cos 2\theta_{s1} & -\frac{V_{s1}}{V_{p1}}\sin 2\theta_{s1} & -\frac{\rho_2 V_{p2}}{\rho_1 V_{p1}}\cos 2\theta_{s2} & -\frac{\rho_2 V_{s2}}{\rho_1 V_{p1}}\sin 2\theta_{s2}
\end{bmatrix}
\times
\begin{bmatrix}
A \\ B \\ C \\ D
\end{bmatrix}
=
\begin{bmatrix}
-\sin\theta_{p1} \\
-\cos\theta_{p1} \\
\sin\theta_{p1} \\
-\cos 2\theta_{s1}
\end{bmatrix}
\tag{3.11}
$$

This equation is based on the assumption of plane waves, plus a continuous motion of particles across the interface separating the two layers.

From the equation it is clear that the reflection coefficients, as a function of angle of incidence, are determined by the density ρ, and the velocities V_p and V_s of

both layers.

For all angles above a certain angle of incidence, θ_1, all the energy of the wave will be reflected.

The angle of incidence where transmitted waves propagates along the surface of the discontinuity is defined as the critical angle θ_c, given by;

$$\sin \theta_c = \frac{V_1}{V_2}.$$

And if $\sin \theta_{s2} \succ 1$ as given by equation 3.8, total reflection will occur.

Figure 3.3 illustrates the reflection and transmission of energy of an incident P-wave on a solid-solid boundary.

For this example there are two critical angles, 30 deg and 60 deg. Beyond the first critical angle, that for P-waves, there are no transmitted P-waves. The reflected P-wave energy increases greatly as the angle of incidence increases towards the first critical angle; there are the wide-angle reflections which are used extensively in seismic refraction work to determine critical distances. Similarly, beyond the critical angle for S-waves there are no transmitted S-waves.

3.5   Wave propagation theory used in Nucleus

Nucleus is a software, constructed as a tool for designing seismic surveys and to carry out feasibility studies - ranging from exploration surveys, reservoir characterization projects to seismic monitoring studies - in a way that all aspects of the acquisition system can be simulated, quantified and evaluated on synthetic data.

The *1D Reflectivity modelling* module within Nucleus provides the user the ability to accurately model and predict the behaviour of the elastic seismic wave field in a horizontally layered earth model. All kinds of waves can be included in this modelling; P-waves, S-waves, converted waves, refracted waves, as well as surface and interbed multiples. What makes this tool so valuable for amplitude versus offset (AVO) or seismic reservoir characterization studies, is the ability this program has to calculate the full frequency dependent interaction of the various seismic wave fields. Even in the presence of thin layering.

Anelastic attenuation can be incorporated by specifying the quality factors Q_p
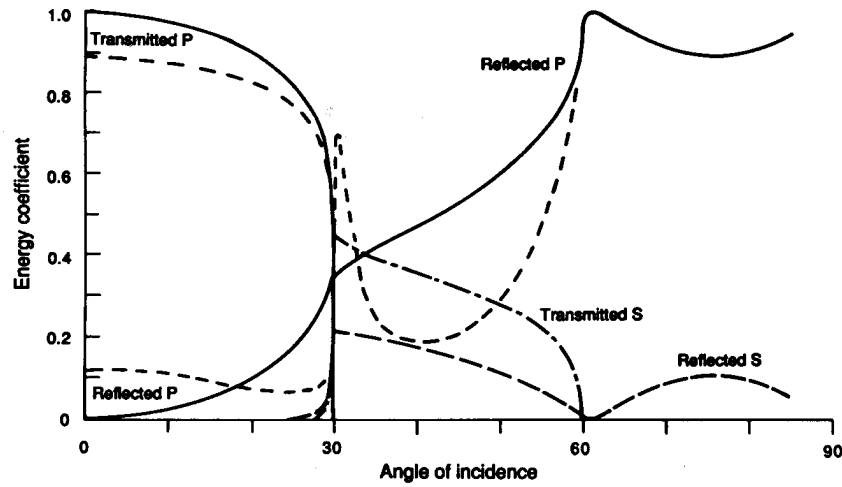
Figure 3.3: *Reflected and transmitted energy for a P-wave incident on an interface between two solid media.*
For this example: $V_{p1}/V_{p2} = 0.5$, $\rho_1/\rho_2 = 2.0$, $V_{p1}/V_{s1} = 1.87$, and $V_{p2}/V_{s2} = 1.73$.
Solid lines, reflected and transmitted P-wave; long dashed line, reflected S-wave; the dashed and dotted line, reflected S-wave; the short dashed lines, reflected and transmitted P-wave when $\rho_1/\rho_2 = 1.0$ (Fowler, 1998).

and Q_s. Additionally, anisotropy can be specified through Baniks anisotropy parameters ε_p and ε_s, which describe a vertical transverse isotropic (VIT) medium (PGS, 2001).

This seismic wave field can be modelled for the conventional streamer acquisition geometry, for ocean bottom seismic (OBS) acquisition, vertical cables (VS), and vertical seismic profiling (VSP).

For the construction of a subsurface model there are some required parameters for each layer. These are the thickness of the layer $[m]$, the P-wave velocity $[m/s]$, the S-wave velocity $[m/s]$, and the density $[kg/dm^3]$. Some optional information can also be added if desired; the quality factor for P- and S-waves, and the anisotropy parameter for P- and S-waves.

The maximum number of layers is set to 2.500.

Under the *modelling* menu item, four marine modelling options are offered. These are *streamer-*, *OBS-*, *VC-*,and *VPS reflectivity* modelling. A fifth option is *land reflectivity* modelling. The options for in- or excluding parts of the wave field differ slightly, due to the different implementation of reflectivity algorithms em-

ployed for the available survey types. How these options vary are summarized in table 3.4.

	Streamer	OBS	VSP	Vertical Cable	Land
modelling type	elastic/acoustic	elastic	elastic	Elastic/acoustic	elastic
an-/isotropic	both (default is model depended)	both (model depended)	isotropic	Both (default is model depended)	isotropic
interbed multiples	yes/no	yes/no	yes	yes/no	yes
surface multiples	no/yes	no/yes	no/yes	no/yes	no/yes
P-S converted waves	yes	yes/no	yes/no	yes/no	yes/no
absorption effects	yes/no	yes/no	yes/no	yes/no	yes/no
up/-downgoing P- or S-wave field	-	-	yes/no for P- or S-waves	-	yes/no for P- or S-waves
Wavefields	pressure	pressure, vertical comp. horizontal comp.	vertical comp. horizontal comp.	Pressure	vertical comp. horizontal comp.

Figure 3.4: *Available options for wave field calculations for the different survey types in the 1-D Reflectivity module within Nucleus (Nucleus, 2001).*

The modelling of the seismic data is performed in two steps. First the plane wave seismic response for each ray parameter p is calculated, then the resulting $\tau - p$ gather is transformed to the $x - t$ domain.

The first step is based on a modification of Kennett (1983)s recursive reflectivity matrix multiplication algorithm by Lokshtanov (1993).Various wave field components or effects can in this first step be included or excluded, e.g. absorption effects, surface or interbed multiples, converted waves. The increment in p-values controls the accuracy of the modeling.

In the second step the spherical divergence effect of a line or a point source is added through an inverse Radon transformation from the $\tau - p$ to the $t - x$ domain.

The scheme used to compute the reflection response from a stratified media is as mentioned earlier developed by Lokshtanov (1993). It consists of three steps:

- Decomposition of the source wavefield into plane waves.

- Evaluation of the reflection response due to each incident plane wave.

- Summing the plane wave reflection responses.

If attenuation is included in the calculations this will require changes in the second step only. This is because the source and the geophones are located in the upper water layer without attenuation.

Lokshtanov (1993) states that the exact reflection response from a horizontally-layered medium due to a line source can be expressed as a superposition of all reflected plane waves with different slownesses p:

$$P(\omega, x) = \int_{-\infty}^{\infty} R(\omega, p) S(\omega, p) \exp\{i\omega p\} \, dp. \tag{3.12}$$

In this equation P is a pressure or displacement potential in the upper water layer at the geophone depth level, ω is a temporal frequency and x is an offset. $S(\omega, p)$ is a source term, describing the spectrum of the source wavelet and the source directivity pattern. The term $R(\omega, p)$ describes the complex plane wave reflection coefficient from a subsurface structure.

In the computer code Lokshtanov (1993) developed, he performed the integration 3.12 by a discrete wave number approach (Bouchon & Aki, 1977), while the reflection coefficients $R(\omega, p)$ are found by using the fast and accurate recursive scheme developed by Kennett (1983). This scheme uses as input the plane wave reflection and transmission coefficients for individual boundaries.

The intrinsic attenuation effects can be included in Kennetts scheme. These effects lead to complex and frequency dependent P- and SV- velocities. This will furthermore influence the vertical slownesses, and reflection and transmission coefficient for individual boundaries.

The wave equation that the calculations done in the 1D Reflectivity moduli in Nucleus is based on, is the one dimensional wave equation given as;

$$(\lambda + 2\mu) \frac{\partial^2 u_x}{\partial x^2} = \rho \frac{\partial^2 u_x}{\partial t^2} \tag{3.13}$$

where λ is Lams elastic constant, μ the shear modulus, u_x is the displacement and ρ is the density. This equation is given by White (1983).

3.6   Chapter Summary

In this chapter a fundamental understanding of how a wave propagates in a medium is established.
Initially the equation of motion is defined (equation 3.1), which further is used to show the deduction of the seismic wave equation (equation 3.7).

Definitions of reflection and transmission are also given in this chapter. An introduction to Snell's law is given to help understand the complex Zoeppritz equations, which describe the reflection coefficients.

To have a basic understanding of how the software used in the modelling is built up, gives a better understanding of the results obtained. To know the foundations behind Nucleus helps getting a wider perspective on the models made in the research. And this further helps give a deeper knowledge of the outcome.

Chapter 4

Modelling of seismic attenuation

4.1   Introduction

This chapter presents the modelling performed to study various characteristics due to attenuation of seismic waves.

The modelling itself is divided into two main groups - conceptual modelling and somewhat more realistic modelling. The purpose for this segmentation is to primarily obtain a basic understanding of how a signal will change when exposed to attenuation of varying degree. And then, secondly, using this to understand the changes a signal will go through when several of the physical parameters will vary.

Each main section gives a description of the construction of the models, the modelling, and the achieved results. The results in particular, are described thoroughly in regard to theories, physical laws and previous obtained results.

4.2   Initial models

To better understand the effects influencing a seismic wave as it propagates in a solid material, these initial models are kept very simple and perspicuous.
The purpose of the initial models is to give an understanding of the basic effects of the thickness of overburden, and of the reservoir itself. The effect of attenuation alone is also explored by keeping all parameters, except Q-factor, fixed.

4.2.1 Earth models

Earth models are built under the option $Model \rightarrow Create \rightarrow Simple\,model\,builder$ in the 1-D Reflectivity module in Nucleus.

To keep the models simple, the amount of layers is limited to 4. All layers are homogeneous, isotropic and flat.

The modelling is executed in several sets of models. Meaning that almost identical models are explored, i.e. only Q_p and Q_s in the reservoir layer are varied. The remaining parameters; such as velocities, density and thickness, are set constant for all these models.

The first set of earth models is very simple. The first earth model is illustrated in figure 4.1.
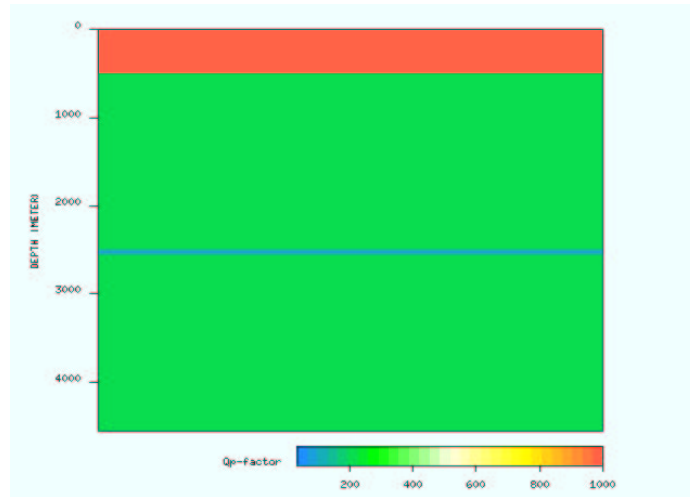
Figure 4.1: *1D earth model used for forward modelling. The Q_p-factor is used as the plot parameter.*

The values of the different parameters used in the first five models are listed in table 1.1. In this table *layer 3* represents the reservoir. The velocities in this layer are kept the same as in the overburden, in order to prevent a reflection response from top reservoir. There is a small change in density so that the software program will recognize it as an individual layer.

The Q-factor in the reservoir layer are chosen from 30 to 200, based on an article by Clark et al. (2001). These are the typical values for a Jurassic sandstone reservoir in the North Sea. For the water layer, the Q_p and Q_s are both set to

MODEL 1A						
	$d\,(m)$	$V_p\,(m/s)$	$V_s\,(m/s)$	$\rho\,(kg/dm^3)$	Q_p	Q_s
Layer 1	500	1.480	0	1,00	10.000	10.000
Layer 2	2.000	2.000	1.000	2,30	200	100
Layer 3	50	2.000	1.000	2,31	200	100
Layer 4	3.000	3.000	1.500	2,40	200	100

MODEL 1B						
	$d\,(m)$	$V_p\,(m/s)$	$V_s\,(m/s)$	$\rho\,(kg/dm^3)$	Q_p	Q_s
Layer 1	500	1.480	0	1,00	10.000	10.000
Layer 2	2.000	2.000	1.000	2,30	200	100
Layer 3	50	2.000	1.000	2,31	150	75
Layer 4	3.000	3.000	1.500	2,40	200	100

MODEL 1C						
	$d\,(m)$	$V_p\,(m/s)$	$V_s\,(m/s)$	$\rho\,(kg/dm^3)$	Q_p	Q_s
Layer 1	500	1.480	0	1,00	10.000	10.000
Layer 2	2.000	2.000	1.000	2,30	200	100
Layer 3	50	2.000	1.000	2,31	100	50
Layer 4	3.000	3.000	1.500	2,40	200	100

MODEL 1D						
	$d\,(m)$	$V_p\,(m/s)$	$V_s\,(m/s)$	$\rho\,(kg/dm^3)$	Q_p	Q_s
Layer 1	500	1.480	0	1,00	10.000	10.000
Layer 2	2.000	2.000	1.000	2,30	200	100
Layer 3	50	2.000	1.000	2,31	50	25
Layer 4	3.000	3.000	1.500	2,40	200	100

MODEL 1E						
	$d\,(m)$	$V_p\,(m/s)$	$V_s\,(m/s)$	$\rho\,(kg/dm^3)$	Q_p	Q_s
Layer 1	500	1.480	0	1,00	10.000	10.000
Layer 2	2.000	2.000	1.000	2,30	200	100
Layer 3	50	2.000	1.000	2,31	30	15
Layer 4	3.000	3.000	1.500	2,40	200	100

Table 4.1: *Earth properties of the five different models made in the first set of modelling. Layer 3 represents the reservoir.*

10.000. In the remaining two layers Q_p is set to 200, and Q_s to 100.

Now, after discussing the modelling results of model 1, other models are explored. This to see how the different parameters influence the attenuation of the waves. The thickness of the overburden for the new models varies. Three new values are chosen; 500, 1.000 and 1.500 meters.

For all the new models, the thickness of the reservoir is increased to 100 meters. This is done to increase the travel path for the waves, thus expose the signal for stronger attenuation. This change is done to better see the effects of a change in Q-factor in the reservoir.

The thickness of the basement is also increased to 3.000 meters for all the new models.

4.2.2 Shot geometry

Before the modelling itself can be done, the vessel conducting the survey has to be created.

A 30.0 Hz Ricker wavelet (the center frequency is set to 30.0 Hz) is used as the seismic source signal. The sample rate is set to 2 ms. This specific wavelet is chosen because it resembles the most of a seismic signal used in real seismic surveys.

The signature of the seismic source used in the modelling is displayed in figure 4.2.

The vessel is defined with a streamer. To build such a vessel the options $Vessel \rightarrow Create \rightarrow With\,streamer$ is used.

The vessel is designed with one streamer, and the Ricker wavelet is adopted as the source signal. The streamer depth is 6 m, while the shot depth is 5 m. The group-length is set to 12.5 m, the near-offset is 200 m, and the group-interval to 25 m. The streamer contains 160 groups, which gives a maximum offset of 4.200 m. Surface related multiples are not computed, while interbed multiples are included.
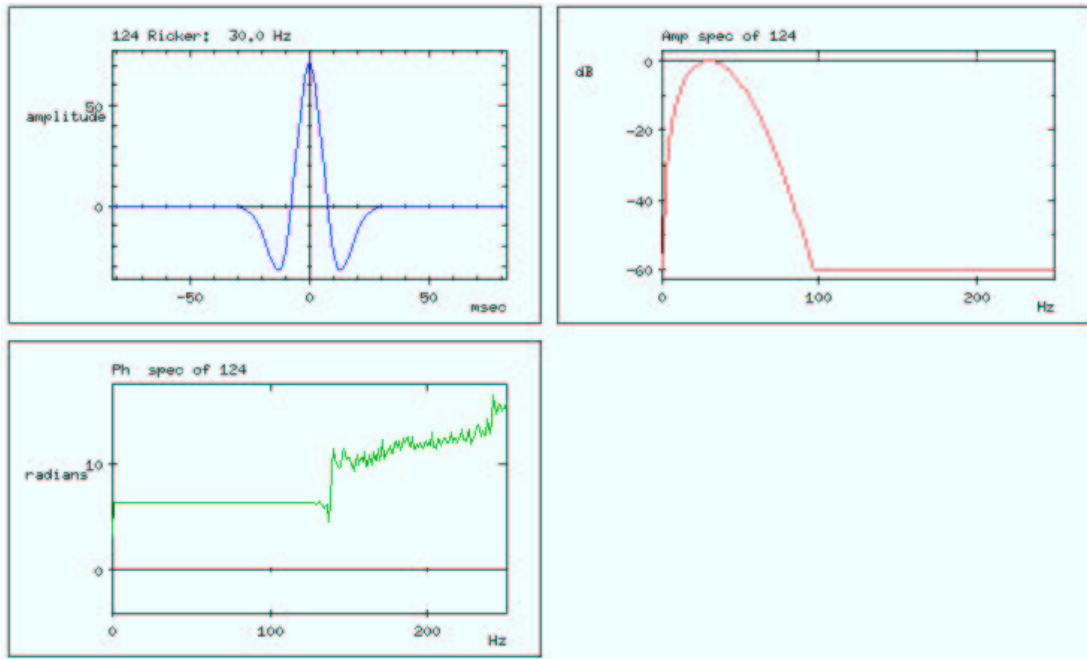
A model of the vessel is shown in figure 4.3.

Figure 4.2: *The source signature (Ricker wavelet of dominant frequency of 30.0 Hz) and its amplitude and phase spectrum.*
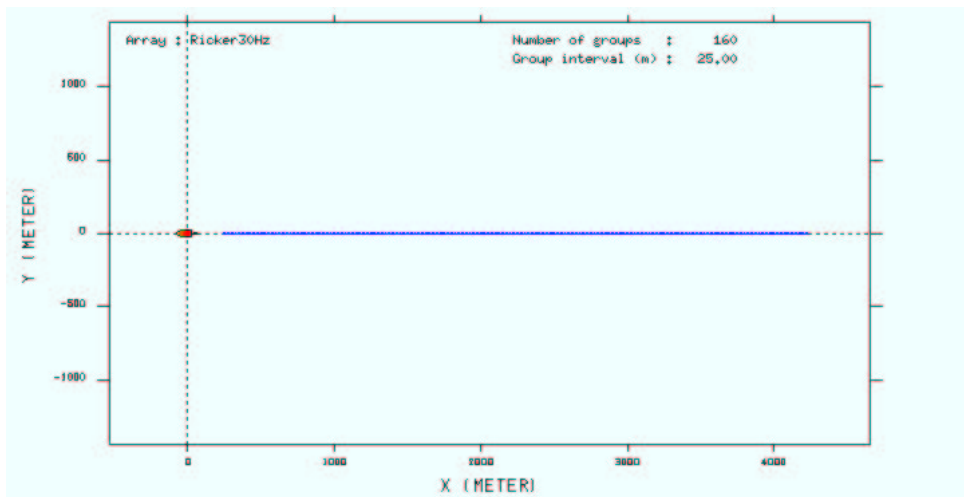

Figure 4.3: *A model of the shot geometry used in the seismic modelling.*

4.2.3   The modelling

The option *Automatic seismic modelling* is used to perform the modelling itself. It is performed in two steps. First the plane wave seismic response for each ray parameter p is calculated, then the resulting $\tau - p$ gather is transformed to the $x - t$ domain. This step is based on the modification (Kennett, 1983) of recursive reflectivity matrix multiplication algorithm by Lokshtanov (1993). Here various wave field components or effects can be included or excluded, e.g. surface or interbed multiples, converted waves, and absorption effects.

In the second step the spherical divergence effect of a line or a point source is added through an inverse Radon transformation from the $\tau - p$ to the $x - t$ domain. Simultaneously, the dip dependent directivity effect of the source and receiver array as specified in the vessel parameters can be added.

By using automatic seismic modelling these two steps start automatically, while they normally need to be started manually one after the other by the user.

To display the synthetic seismogram in colors on have to use the option $Plot \rightarrow Seismic\,data \rightarrow Interactive\,seismic\,plotting$. If colors are not necessary, $Plot \rightarrow Reflectivity\,result$ can be used instead.

To be able to compare the different wavelets, and to better see the effect of attenuation, another module in Nucleus is used; *Wavelet analysis*.

The wavelet analysis module is a single trace utility for signal comparison, filtering, manipulation and filter design. Data must be imported into this module via the $Data$ menu. Through $Data \rightarrow Input\,to\,workfile$, the user can select a dataset, or a part of a dataset, that subsequently will be converted to a workfile. Workfiles can also be generated directly in $Wavelet\,analysis$; as done when creating the source signal.

Traces 5 and 155 are, after the modelling of the synthetic seismogram, imported and truncated, so that the wavelets can be compared more easily. To perform this comparison, the option $Plot \rightarrow Comparison\,analysis$ is chosen, where the two current truncated traces are chosen. The traces are overlayed, showing *wavelet difference*, *spectral difference*, *superimposed wavelets* and *superimposed spectras*. The difference in the two traces compared, is showed visually, but it is not defined by specific values.

To get a better presentation of the exact difference, a *Wiener filter* is generated.

One of the wavelets is set as the input signal, and the other as the output. *Wiener filter generation* is used to perform this analysis. A two-sided, shaping filter is selected. The length of the filter is 200 ms, and 0.10 percent pre-whitening noise is added to make the filter more stable.

The result of such a plot shows the spectrum of the Wiener filter that would be used to convert the input to the output, plus its amplitude and phase spectrum. Especially the plot of the phase change will give useful information. It will show the change in phase the input wavelet, in order to equal the output wavelet.

4.2.4   Results

First set of models

The main objective of the modelling is to obtain information on how the attenuation of seismic waves behaves. And moreover, to try to decide if the effects of attenuation can give information of saturation conditions in the reservoir.

To obtain the basic understanding of these questions, the initial models have been made very simple as only the value of Q_p and Q_s varies. This way it is possible to see the isolated effect of attenuation.

The synthetic seismograms generated from the earth models listed in table 1.1 are all very similar. The main difference is the magnitude of the amplitudes of the reflector at the bottom of the reservoir. But even these effects are so small that they are hardly detectable just by looking at the seismograms.

One of these seismograms, model 1E, is shown in figure 4.4.

The first break at 0.67 seconds is the reflection of the sea bed. The following event at 2.72 seconds is the PP-wave reflection of the bottom of the reservoir. The attenuation of the seismic energy is clearly demonstrated in the diminishing amplitude of the reflections, from the first break to the second event.

As mentioned earlier, the seismograms generated from the first set of models have a high degree of similarity. To get a better understanding of just how small these differences are, the wavelets reflecting the bottom of the reservoir for all five seismograms are compared to eachother. Both trace 5 and trace 155 are investigated. For instance, trace 5 from the seismogram based on model 1A is
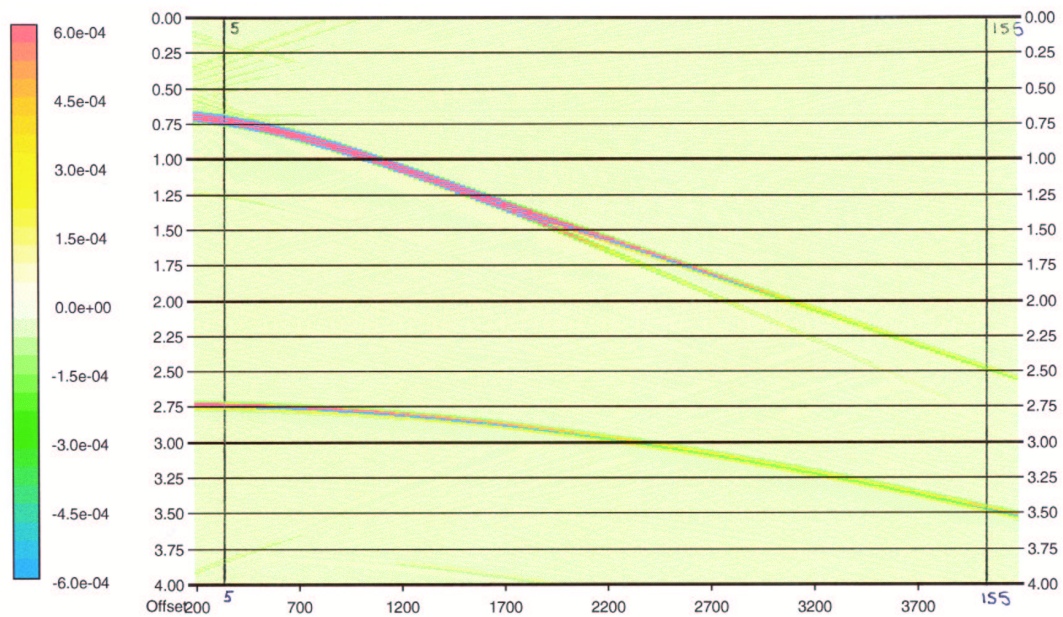
Figure 4.4: *A synthetic seismogram exploring earth model 1E, from table 1.1. Traces 5 and 155 are marked on the plot.*

compared to trace 5 from the seismogram based on 1B, and so on.
The comparison methods are explained earlier in section 4.2.3.

Trace 5   Figure 4.5 shows the comparison between three different scenarios. The images on the left shows the two wavelets of interest overlayed, while on the right side the overlaying amplitude spectras of the same wavelets are displayed. On top, two wavelets passing through a reservoir where the Q_p-factor equals 200 and 150, respectively (models 1A and 1B), are compared to each other (*Case A*). In the center, the wavelet from model 1A above is used, where as the other one is extracted from a model where the value of Q_p-factor in the reservoir is set to 30, model 1E (*Case B*). The image on the bottom displays wavelets extracted from reservoirs where Q_p-factor equals 50 and 30 (models 1D and 1E), respectively (*Case C*).

That differences in the wavelets shape and amplitude spectra are very small is also illustrated in figure 4.5. The greatest difference is found in the center model, case B, where also the difference between the two values of Q_p are the greatest; 170 units. For the top and the bottom model the differences are limited to 50 and 20 units, respectively.
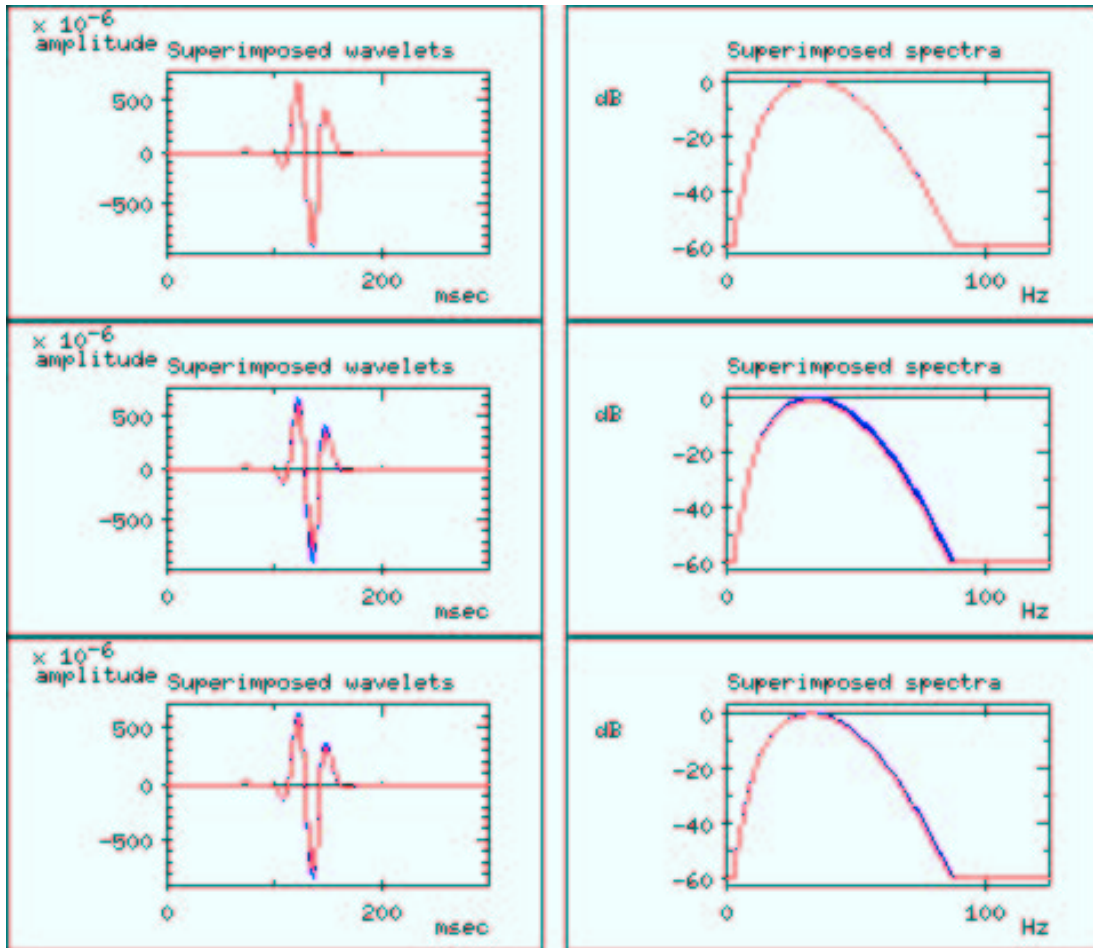
Figure 4.5: *On the left side two and two wavelets are overlayed; superimposed wavelets. While on the right side, the same wavelets' amplitude spectras are overlayed; superimposed spectras.*

These wavelets are extracted from trace 5 from the seismograms generated for the initial models. On top, models 1A and 1B are compared. In the center models 1A and 1E, and on the bottom, models 1D and 1E are compared.

The blue wavelets represent the reservoir with the highest value of Q_p, while the red wavelets represent the lowest Q_p values.

It is an important observation to see that there is a greater difference for case C than for case A, even though the difference in Q_p is bigger for case A. This is a general trend for all the comparisons made. The lower the Q_p-values are for the two scenarios compared, the greater relative difference there are in the shapes of the wavelets.

When comparing the phase spectras obtained from the Wiener filters generated (described under section 4.2.3), the same tendency is revealed.

Figure 4.6 illustrates the phase spectrum of the Wiener filters generated to compare the wavelets described as case A, B, and C.
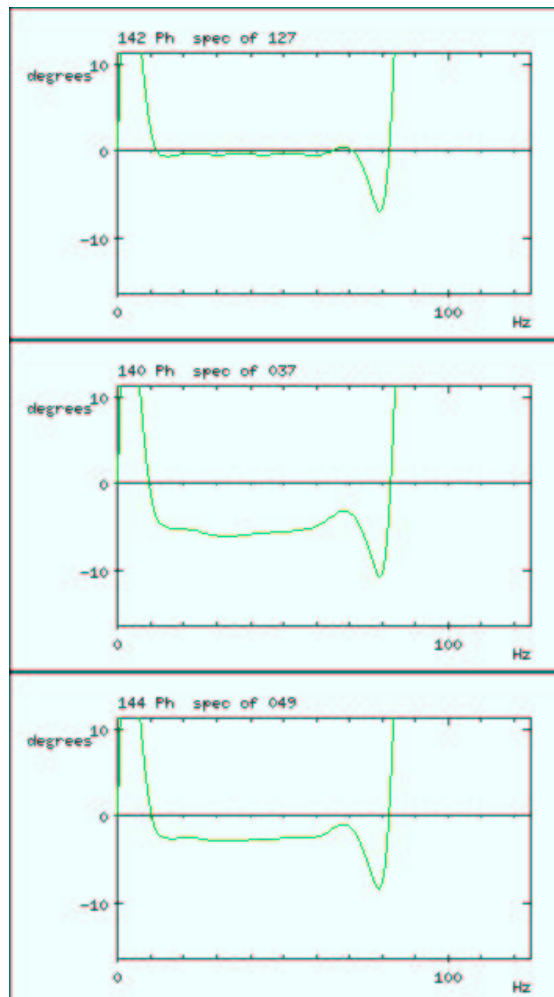
Figure 4.6: *The phase change of different Wiener filter generated. From the top down, the results from cases A, B and C, respectively, are displayed. These wavelets are extracted from trace 5.*

The phase change for case A is extremely small. It is measured to equal approximately 0.5 deg.

As demonstrated in figure 4.5, and thus also expected for the change in phase, the largest change between the two wavelets investigated is found in case B. Here the phase rotation from the first to the second wavelet is about 5.5 deg.

And another similarity between the two figures displayed, figures 4.5 and 4.6, is that there is found a larger rotation of phase in case C than for case A. The change in phase for case C, approximates 3.0 deg. 6 times greater than for case A. This supports the assertion that the lower the initial values are of the two wavelets compared, the larger the differences between them will be.

To control that the phase change found graphically was correct, calculations are performed to see if the theoretical result coincide with result measured from the plots. These calculations are based on equation 4.3, and the actual execution of the computation is displayed in Appendix B.

The conclusion to this operation is that the results are the same for both calculations and measurements of the plots.

An interesting aspect found when analyzing the phase rotation for these models, is that it is totally independent of the thickness of the overburden. Since the attenuation is identical for the two wavelets compared through out the whole overburden, the phase rotation for e.g. from Q_p=200 to Q_p=30, is the same for all cases studied.

But there is a difference between the first groups of models made, and the second group, due to the fact that the thickness of the reservoir was increased from 50 m at first, to 100 m for the following models. This gives that the phase rotation undergoes a doubling as a consequence of the doubling in thickness.

This can also be verified through simple calculations.

The phase rotation, $\Delta\varphi$, is given by the formulae

$$\Delta\varphi = 2\pi f \Delta t, \tag{4.1}$$

where f is the frequency of the source signal, and Δt is the difference in travel time, t, between the two wavelets compared.

Further, the travel time for the each of the two wavelets is given by

$$t = \frac{2d}{c(f,Q)},$$ (4.2)

where d is the thickness of the reservoir, c is the velocity of the wave, and f and Q are frequency and Q-factor.

From equation 4.2 one can easily see that if doubling the thickness of the reservoir, thus the traveltime will also double. Which further on will double the phase rotation.

Trace 155   The same scenarios; cases A, B and C, are further analyzed by comparing the wavelets from trace 155 (which equals an offset of 4.100 meters).

Figure 4.7 displays the same as in figure 4.5, but only this time with reference to the trace of current interest.

The effects of attenuation at larger offsets are still very small. But they are nevertheless larger than what is the case for near offsets (demonstrated through trace 5). A closer look at the wavelets shows that the distortion of the signal is almost twice as large as it was when considering trace 5. Meaning that e.g. the relative difference between the two wavelets in case B is twice as big when comparing them at trace 155 than for trace 5.

Beyond that, the results in figure 4.7 are very similar to what is shown in figure 4.5. Case B has the largest difference between the two wavelets compared, and the wavelets in case C, despite a smaller difference in Q_p-value between them, still has a larger difference in amplitude than what is illustrated in case A.

The phase rotations of the wavelets for trace 155 give surprising results. The phase rotation is increasing with diminishing thickness of the overburden. The exact opposite tendency is the expected outcome. E.g. the rotation between two compared wavelets, from reservoirs where Q_p equals 200 and 30, and where the thickness of the overburden is 2.000 meters, shows a lot smaller value than for the same case but where the overburden is 500 metes thick (found in further modelling).

But the results obtained are not results of attenuation. Through a further investigation of these results it is found that this effect is caused by the equations founding the 1-D Reflectivity modulus in Nucleus.
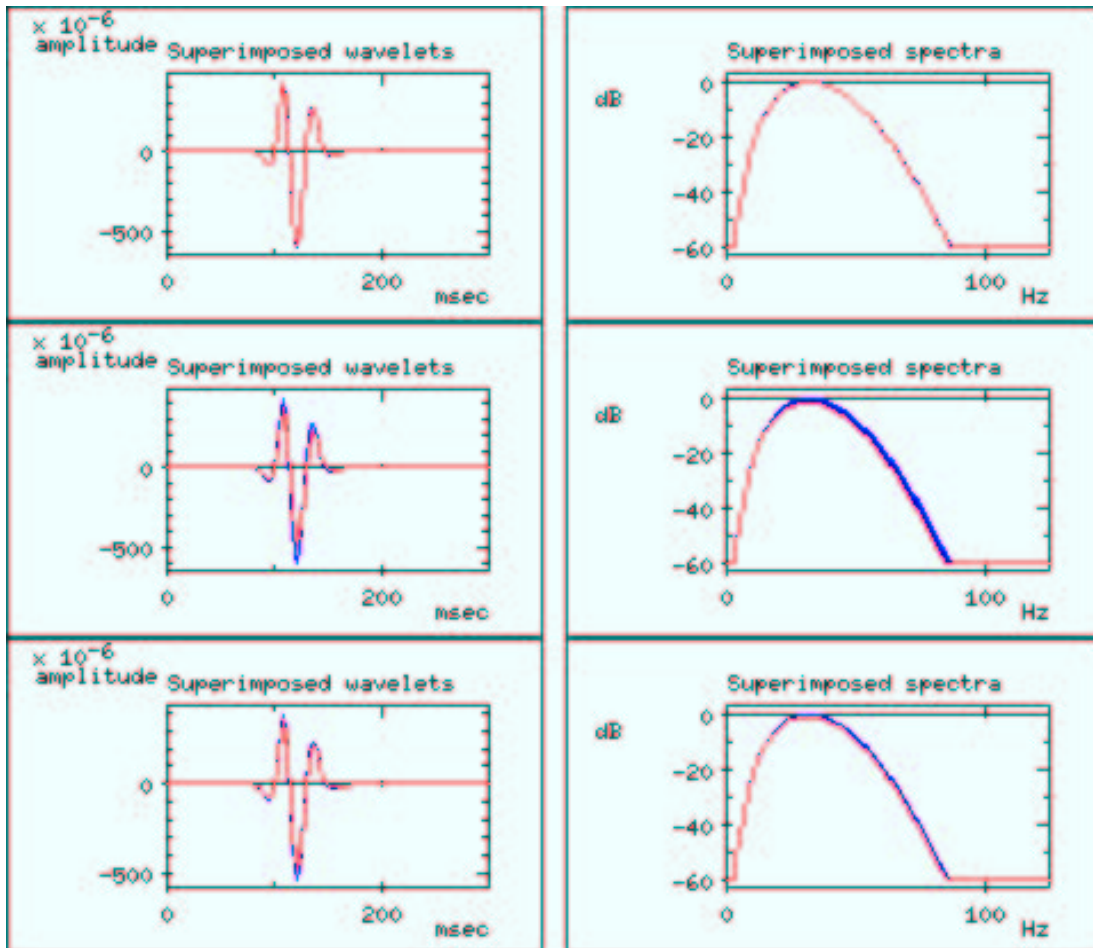
Figure 4.7: *Superimposed wavelets and their amplitude spectras.*
The wavelets are extracted from trace 155 from the different synthetic seismograms
to show the results of case A, B and C. On top, models 1A and 1B are compared.
In the center models 1A and 1E, and on the bottom, models 1D and 1E are
compared.
The blue wavelets represent the reservoir with the highest value of Q_p, while the
red wavelets represent the lowest Q_p values.

The attenuation effects are introduced by using complex velocities. The definition of the complex velocities used, is as follows;

$$c(f, Q) = c(f_0) \left(1 + \frac{1}{\pi Q} \ln \left(\frac{f}{f_0} \right) - \frac{i}{2Q} \right),$$ (4.3)

where $c(f, Q)$ is the complex phase velocity, and $c(f_0)$ is the (real) phase velocity. f is the frequency set by the user, while f_0 is the reference frequency in Nucleus (100 Hz).

Reflectivity modelling is done in 3 steps:

1. Calculations of scattering matrices for all interfaces (reflection and transmission coefficients).

2. Wave propagation.

3. Conversion from a plane wave representation to spherical/cylindrical wave.

In Nucleus, the complex velocities are introduced after step 1. I.e. reflection/transmission coefficients are calculated from real velocities. In other words the coefficients are calculated for elastic media. The wave propagation (step 2) however takes phase and amplitude changes induced by attenuation into account.

So when traces of lager offsets (e.g. trace 155) are analyzed as described above, total reflection might occur. This will result in a phase change in the reflection coefficient. And since the angle of incidence will increase with decreasing thickness of the overburden, the effect of this phenomena will thus increase with increasing angle; with diminishing overburden thickness.

As mentioned above, this is exactly the result obtained when comparing and investigating the phase changes obtained for trace 155. This is also illustrated in figure 4.8 (notice the scaling on the y-axis).

Second set of models

After the first set of models has been carried out, small adjustments are made so that the effects of overburden would be clarified. This resulted in three new sets of models. These will all be processed under this section.

Other minor adjustments were also made. These are explained in section 4.2.1.
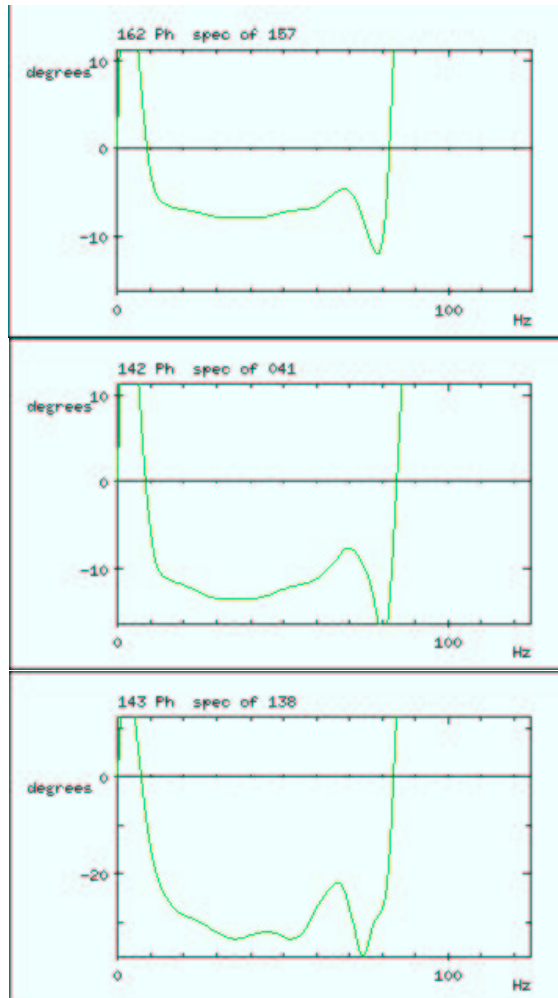
Figure 4.8: *Phase change between a wavelet travelling through a reservoir of $Q_p = 200$, and one travelling through a reservoir of $Q_p = 30$. Thickness of the overburden is the varying factor. On top the thickness is 2.000 m, in the center 1.500 m, and at the bottom 500 m.*
These wavelets are extracted from trace 155, which equals an offset of 4.100 meters.

All the seismograms for these models resembles. But since the thickness of the overburden vary from 1.500 to 500 meters, there will automatically be a difference in amount of events and multiples included on the seismogram.
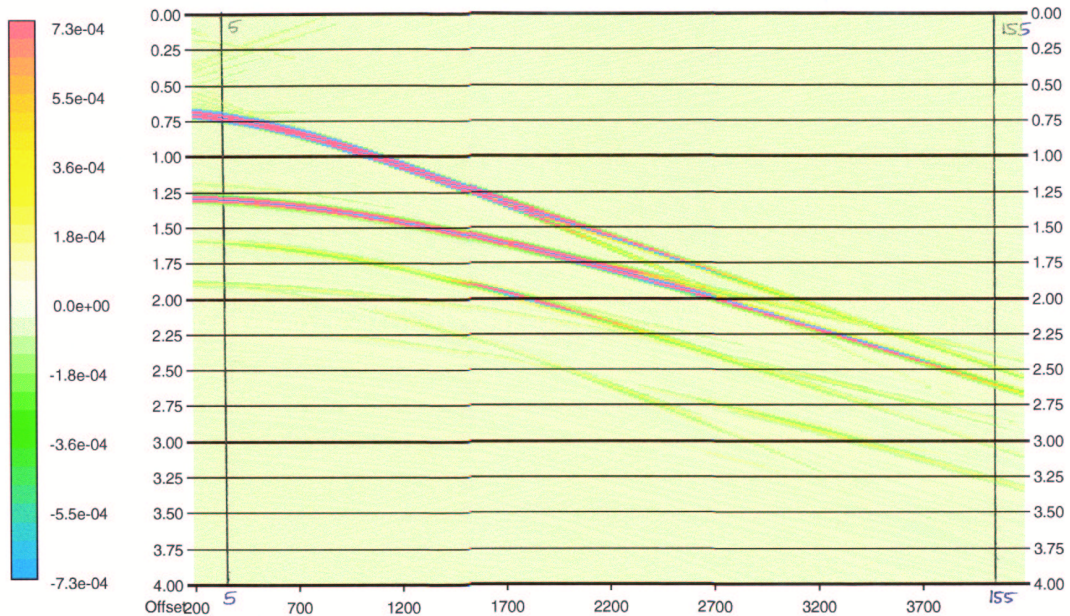
Figure 4.9: *Synthetic seismogram based on the initial model 1E, but the thickness of the overburden has been reduced to 500 m while the reservoir has increased to 100 m. Traces 5 and 155 are marked on the plot.*

Figure 4.9 shows the synthetic seismogram based on earth model 1E, specified in table 4.1. But in this case the thickness of the overburden is reduced to 500 meters, while the reservoir is increased to 100 meters. The thickness of the basement is also increased, from 2.000 to 3.000 meters, but this will not have any effect on the seismogram.

The synthetic seismogram displayed above shows several reflectors. The first break (at 0.68 sec) is the reflection of the sea bed. The following event (at 1.28 sec) is the PP-reflection of the bottom reservoir. At 1.58 sec the PS-reflection is visible. Then, at 1.88 sec, there are actually two events coming in at the same time; a PP-multiple within the overburden and the reservoir, and the SS-reflection. And at last, vaguely at 2.18 sec, a PP-multiple of the PS-reflection is displayed.

Multiples can both occur in the water layer (very common), and within the interbed. An illustration of multiples is found in figure 4.10.
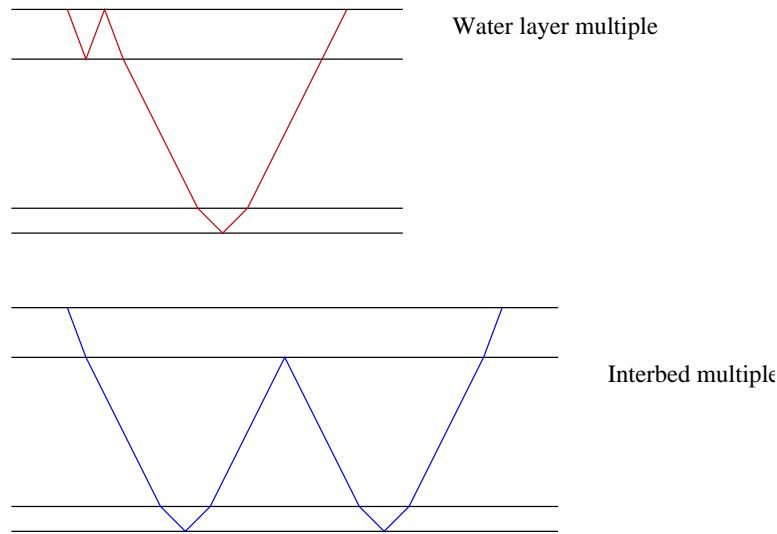
Figure 4.10: *Different kinds of multiples.*

This specific seismogram is chose because it shows to some extent parts of the problems likely to occur in real seismic surveys. The different events interfere, which makes it difficult to extract single wavelets for further studies. Events that are reflections from interfaces interfere with reflections from other interfaces, or with multiples. The wavelet needed for studies is therefore, to varying degree, influenced by other events that are unwanted in this case. This makes it impossible to determine how the amplitude and the phase has changed merely due to attenuation. Further examples on this kind of experimental derangement will be illustrated later.

Trace 5   There is a general trend that is common for all the initial models. Independent of the thickness of the overburden, all comparisons of wavelets shows that case B possesses the largest differences in amplitude between the two wavelets compared. Case A has the smallest difference, and case C demonstrates an average separation of the wavelets.

The wavelets compared in figure 4.11 are extracted from the seismogram shown in figure 4.9. It shows the superimposed spectras of the wavelets from trace 5, compared in the altered cases A, B and C, respectively.

It is a key point to be aware that the scaling on the y-axes is different in this figure than for figure 4.5. Considering this, one can see that the amplitude in

Figure 4.11: *Superimposed wavelets and their amplitude spectras.*
These wavelets are extracted from trace 5 in the seismogram based on an altered version of the initial earth models; where the thickness of the overburden is reduced to 500 meters, and the reservoir is increased to 100 meters.
On top, the altered models 1A and 1B are compared. In the center, models 1A and 1E , while at the bottom models 1D and 1E are compared.

this case is about 5 times larger than the amplitudes of the wavelets presented in figure 4.5. This fact can easily be explained by the much thinner overburden used when modelling the last figure. Here the overburden is 500 m, while it was 2.000 m in the first case.

This is a general trend for all the initial models. The thicker the overburden is, the greater is the reduction in amplitude for the signal. Since a thicker overburden causes a longer travel path for the signal, more energy will be lost, which makes the amplitude to diminish. This is an expected result of attenuation.

The same trends found for the attenuation of amplitudes are valid for the signals change in phase. Case B has the largest change, while C and A are second and third, respectively.

Figure 4.12 illustrates this coherence when displaying the phase change between the same wavelets as above (figure 4.11).

Trace 155   The same tendencies as obtained before are found when an analysis of the wavelets in cases A, B and C when the thickness of the overburden is reduced. The example of an overburden of 500 meters is here used to display the results for trace 155 (figure 4.13).

The largest difference between the two wavelets compared is found for case B, as in all the other examples displayed. Case C has a somewhat smaller difference, while case A has the least change in amplitude of the wavelets compared.

The amplitudes of the wavelets shown in figure 4.7 are half the size of the wavelets displayed in figure 4.13. This is a direct result of that the first signal has traveled through a much thicker overburden than the other signal. A corresponding result is also found in the cases of 1.500 and 1.000 meter thick overburden.

4.3   Realistic models

After the initial modelling is done more realistic models are made. Meaning that realistic values for different reservoir settings are the basis for the different models.

This part of the seismic modelling is also divided into two main groups, depending on the overburden used. The first group, Group 1, uses an overburden with a
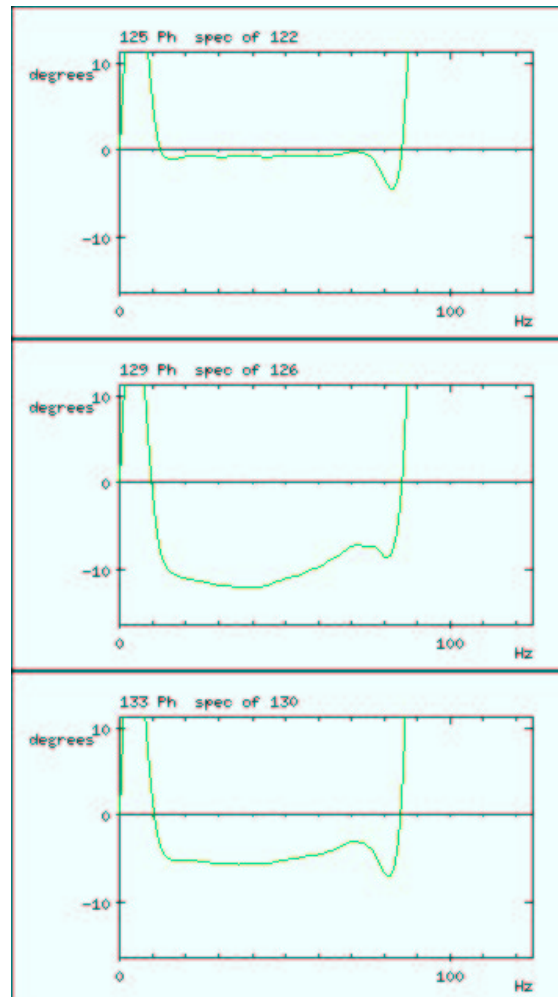
Figure 4.12: *The phase change of different Wiener filter generated. The wavelets are extracted form trace 5.*
From the top down, the results from cases A, B and C form the altered version of initial earth models. On top from the altered models, 1A and 1B are used to generate the Wiener filter. In the center, the altered models, 1A and 1E, and at the bottom the altered models, 1D and 1E are used.
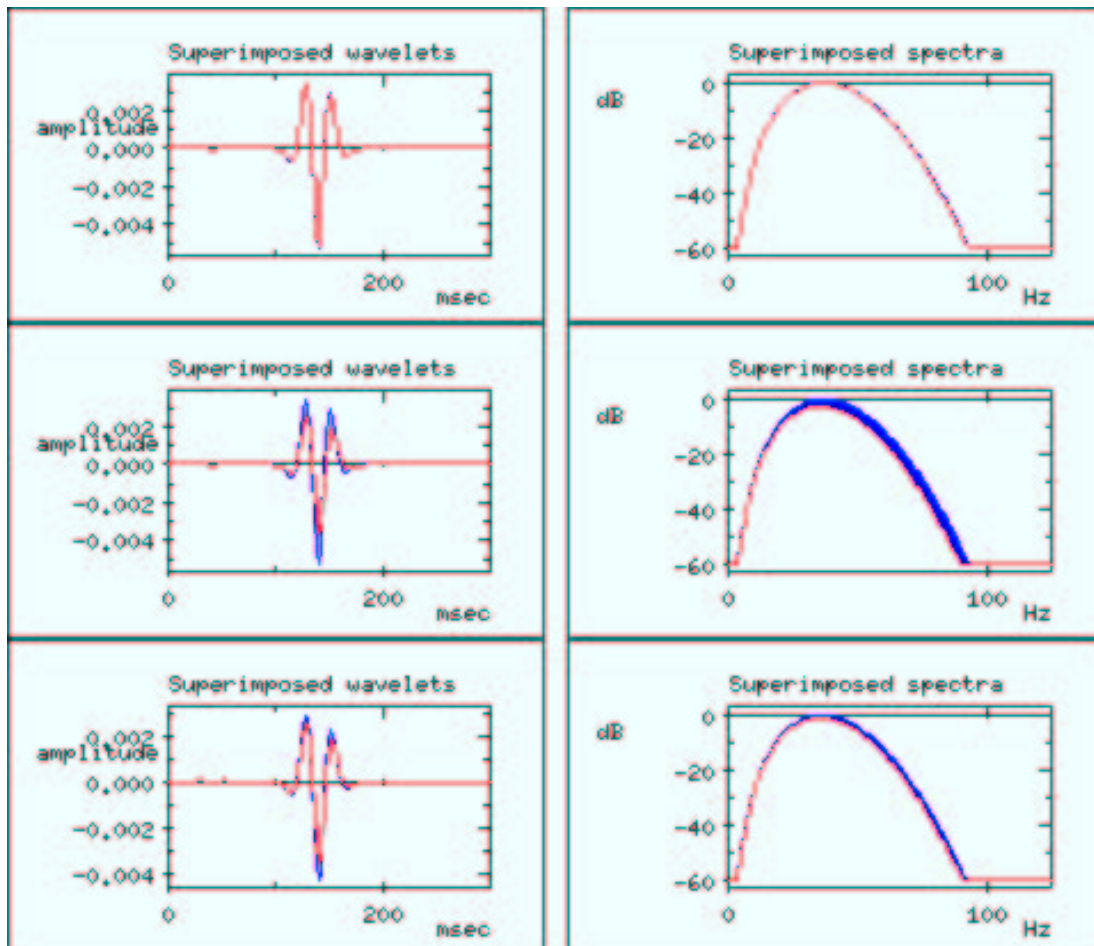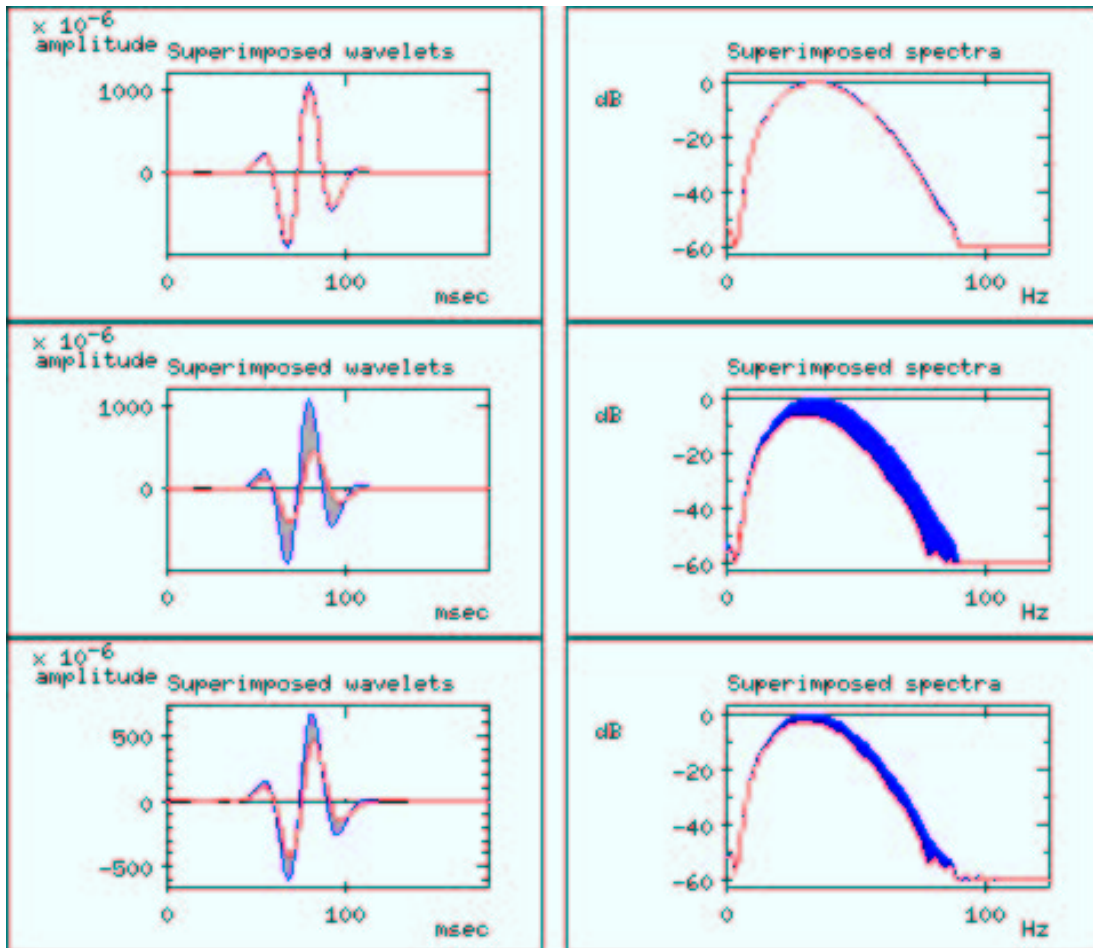
Figure 4.13: *Superimposed wavelets and their amplitude spectras.*
These wavelets are extracted from trace 155 in the seismogram based on an altered version of the initial earth models.
On top, the altered models 1A and 1B are compared. In the center the altered models 1A and 1E, and on the bottom, the altered models 1D and 1E are compared. The blue wavelets represent the reservoir with the highest value of Q_p, while the red wavelets represent the lowest Q_p values.

low degree of attenuation ($Q_p = 200$), whereas for the second group, Group 2, the overburden possesses a higher degree of attenuation ($Q_p = 100$).

Five different reservoir settings are then connected to each of these overburden conditions. The reservoir scenarios made are a dry reservoir, reservoirs with respectively 10, 50 and 90% saturation, and finally a fully saturated reservoir. Combining these options, ten models are made.

The numbers of layers are kept at four, to avoid too many interfering events, that would complicate the wavelet analysis.

The same vessel as used for the initial models is used for this modelling too.

4.3.1 Earth models

As already explained, this part of the modelling was divided into two groups based on the degree of attenuation in the overburden. The values of the parameters used in the two overburden models are listed in table 4.2. The reservoir settings

Models of overburdens						
	$d\,(m)$	$V_p\,(m/s)$	$V_s\,(m/s)$	$\rho\,(kg/dm^3)$	Q_p	Q_s
Overburden 1	1500	2390.0	980.0	2.124	200	150
Overburden 2	1500	2733.4	1261.9	2.280	100	60

Table 4.2: *Parameters defining the two overburdens used in the realistic modeling.*

are described by the parameters listed in table 4.3. The thickness of the reservoir is not included in this table, since this parameter vary. Three different values are used for each reservoir model. 150, 100 and 20 m are explored, to see how the thickness of the reservoir itself will influence the signal.

Reservoir Models						
		$V_p\,(m/s)$	$V_s\,(m/s)$	$\rho\,(kg/dm^3)$	Q_p	Q_s
I	Dry	4670.0	3060.0	2.51	500	375
II	10% saturation	2880.0	1860.0	2.10	50	110
III	50% saturation	2920.0	1830.0	2.15	30	60
IV	90% saturation	3000.0	1820.0	2.25	20	50
V	Fully saturated	4090.0	2410.0	2.37	100	50

Table 4.3: *Table defining the parameters used to simulate the desired reservoir settings.*

These values are extracted from literature. For the first of the two overburden models (Overburden 1), the parameters are an average of seismic parameters presented in an article by Johansen et al. (2002). The other overburden model (Overburden 2) is the shale used in modelling done by Koesoemadinata & McMechan (2001).

As for the reservoir models, the Q_p/Q_s-ratios used for all five cases are found in an article by Winkler & Nur (1982). The remaining parameters are for dry and for fully saturated reservoir defined in Mavko et al. (1998), while the reservoirs with different degree of saturation are given by Heggernes (1988).

The parameters defining the basement are given in table 4.4.

BASEMENT						
	$d\,(m)$	$V_p\,(m/s)$	$V_s\,(m/s)$	$\rho\,(kg/dm^3)$	Q_p	Q_s
Basement	2000	4000	2500	2.80	300	200

Table 4.4: *The parameters defining the basement for the realistic modelling.*

The earth model based on the parameters describing a 90% saturated, and 100 meters thick reservoir, underlying an overburden with high attenuation is illustrated in figure 4.14. Just as for the plot of the initial earthmodel, Q_p is used as the plot parameter.
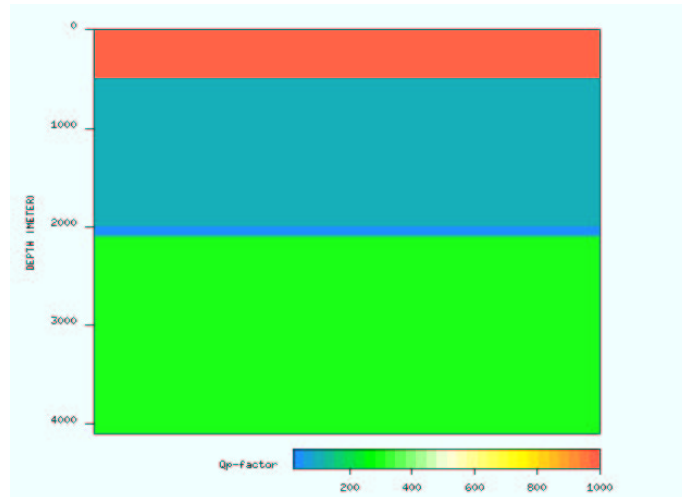
Figure 4.14: *Earth model of a highly attenuating overburden, and with a 100 meter thick reservoir with 90% saturation.*

To get an insight in how other physical effects, besides attenuation, affect the

seismic signal, *reference models* are made for each realistic earth model.

These reference models are completely identical to the original models, except that the attenuation is practically removed. Meaning that the Q_p- and Q_s-factors are given the value 10.000. This way it is possible to observe the effects of the propagation of the wave itself, without the loss of energy and rotation in phase caused by attenuation.

4.3.2   The modelling

The initial steps of the modelling are executed the same way as for the initial modelling (see section 4.2.3).

But the last steps had to be excluded for these models. More specifically; the generation of the Wiener filter, and its consecutive phase change has not been modelled for the realistic models. This is due to the fact that the signal are too distorted due to effects like AVO (Amplitude Versus Offset), reflection coefficients etc., so the phase change generated will be a result of several factors, and therefore not give a concrete estimate of the attenuation effects.

As mentioned above, reference models are made to demonstrate the effects of physical properties when Q-factor is insignificant. This was done for these models, opposed to the initial models, due to the complex construction the realistic seismograms possesses. This way, one can better clarify which effects are caused by attenuation, and which are not.

4.3.3   Results

The results from all the models made are very much alike, and they all show the same trends. Since the correlation between the different models is so large, the findings can easily be illustrated through displaying and commenting on a few of them.

To demonstrate the findings of this part of the modelling, two scenarios are used, plus the reference model to one of the.

Comparing different reservoirs

Both models are based on earth models using Overburden 1. By having the same overburden, and this way keeping the number of parameters varying down, makes it easier to identify the different effects. Models I and III (see table 4.3) and chosen as the reservoir models used to illustrate. Meaning that one dry and one 50% saturated reservoir will illustrate the results.

The reservoirs used are 100 meters thick. This specific thickness is chosen because it involves several of the potential difficulties one can be exposed to in this kind of analysis, without loosing the desired effects. For seismograms displaying a 20 meter thick reservoirs, the top and the bottom reflectors would not be separated enough to distinguish between the two. It is therefore impossible to see the effect on the signal caused just by the propagation through the reservoir. On the other hand, for the models displaying a 150 meters thick reservoir the separation of the two reflectors is too large to (in most cases) introduce the complications caused by interference between them.

To make specific comparisons three traces, at different offsets, are extracted from the seismograms. These are traces 5, 100 and 155, which are all marked on the seismograms.

Figure 4.15, shows the synthetic seismogram generated based on an earth model with a dry reservoir (Overburden 1 + Reservoir I). As mentioned above, traces 5, 100 and 155 are placed on their equivalent offsets.

The first break at 0.68 sec is the reflection of the sea bed, while the event at 1.93 sec is the PP-wave reflection of the top reservoir . The separation between the top and the bottom reflector of the reservoir is just 0.043 sec for a PP-wave, 0.054 sec for a PS-wave, and 0.065 sec for a SS-wave. Thus all of these events, plus their multiples will appear as one on the seismogram. The event of the PS reflection of the reservoir is found at 2.83 sec Finally, the PP-multiple reflector of the reservoir is represented by the event at 3.19 sec.

The synthetic seismogram, displaying the earth model with a 50% saturated reservoir (model III), is shown in figure 4.16. It is very similar to the seismogram displayed above (figure 4.15). The most evident difference is that on this second seismogram the separation between the top and the bottom of the reservoir is more distinguished. It is also easy to see that the loss of energy is greater in

Figure 4.15: *Synthetic seismogram based on the earth model constructed by Over-burden 1, which has a low degree of attenuation, and Reservoir I, which represents a dry reservoir.*
Traces 5, 100 and 155 are marked on the plot.

the 50% saturated reservoir, since the amplitudes are weaker. This is mainly caused by the much larger attenuation found here. The other differences will be commented later.

The seismogram in figure 4.16, shows that the events from the sea bed and the top of the reservoir are situated at the same time as they were in figure 4.15, which is inevitable since they shear the same water layer, and overburden. The bottom of the reservoir, however, is situated 0.07 sec underneath the top reflector, which makes it possible to distinguish between the two reflectors.
The PS-reflection of the top of the reservoir is to be found at 2.83 sec, as is the case for the dry reservoir. But once again the bottom is separated from the top, and this event is at 2.90 sec.

Wavelets from the three traces specified and marked on the seismograms above, are extracted and compared. This procedure is the same as performed for the initial modelling. The overlayed wavelets, and their overlayed amplitude spectras, are shown in figure 4.17.

The blue wavelet represents the dry reservoir, while the red one represents the
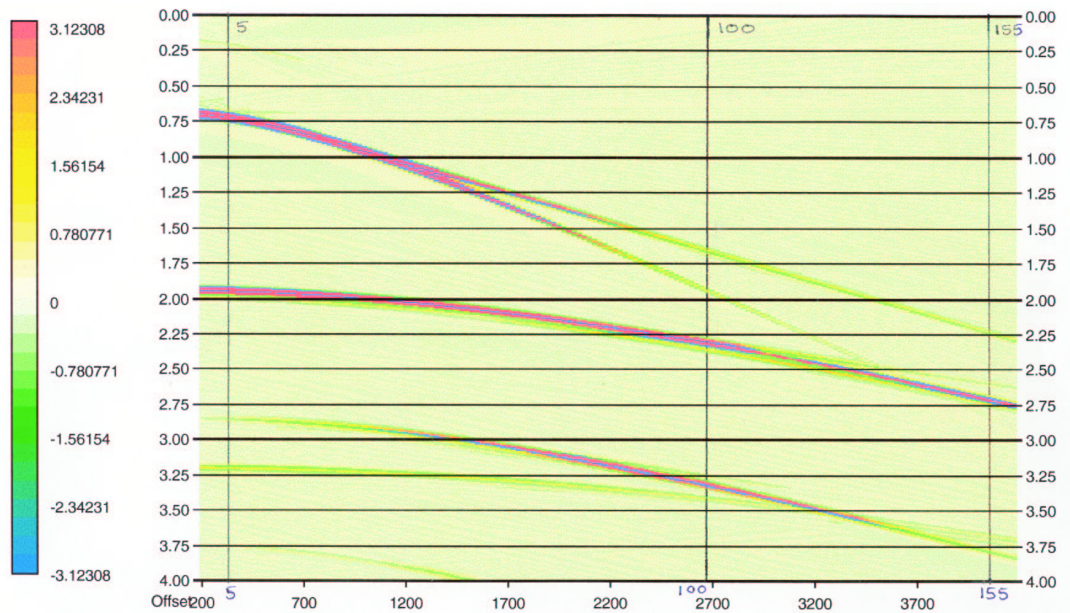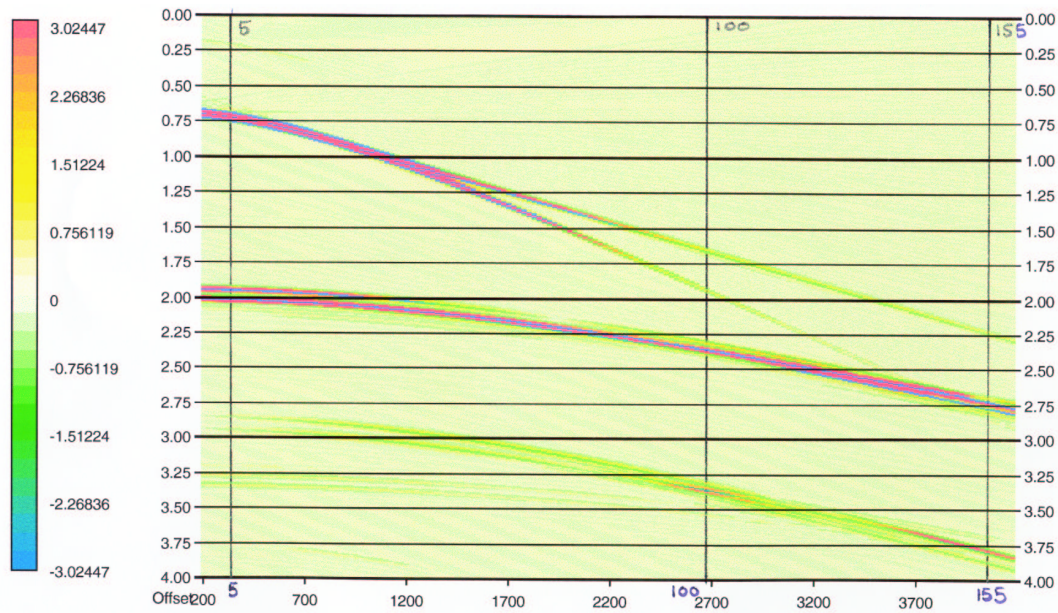
Figure 4.16: *Synthetic seismogram based on the earth model constructed by Overburden 1, which has a low degree of attenuation, and reservoir III, which represents a 50% saturated reservoir.*
Traces 5, 100 and 155 are marked on the plot.

reservoir that is 50% saturated.

Trace 5   The upper part of figure 4.17, gives the comparison between the two wavelets at a near offset. More specifically, at trace number 5. In both cases the wavelet come in at the same time, as remarked earlier. The separation between the two reflectors is more marked for the 50% saturated reservoir, than for the dry one. This is because $V_p\,(dry) \succ V_p\,(50\%\,saturation)$. This gives an interference between the two reflections in the case of the dry reservoir, which might cause the amplitude of the signal to increase significantly (figure 4.17).
Interference between two wavelets, and how this can both increase and decrease the amplitude of the signal is illustrated in figure 4.18.

This effect of interference can also be seen in the comparisons between traces 100 and 155.

The difference in amplitudes for the two cases can also be explained through other physical properties.
Acoustic impedance, I, is defined as seismic velocity, V, multiplied by density ρ
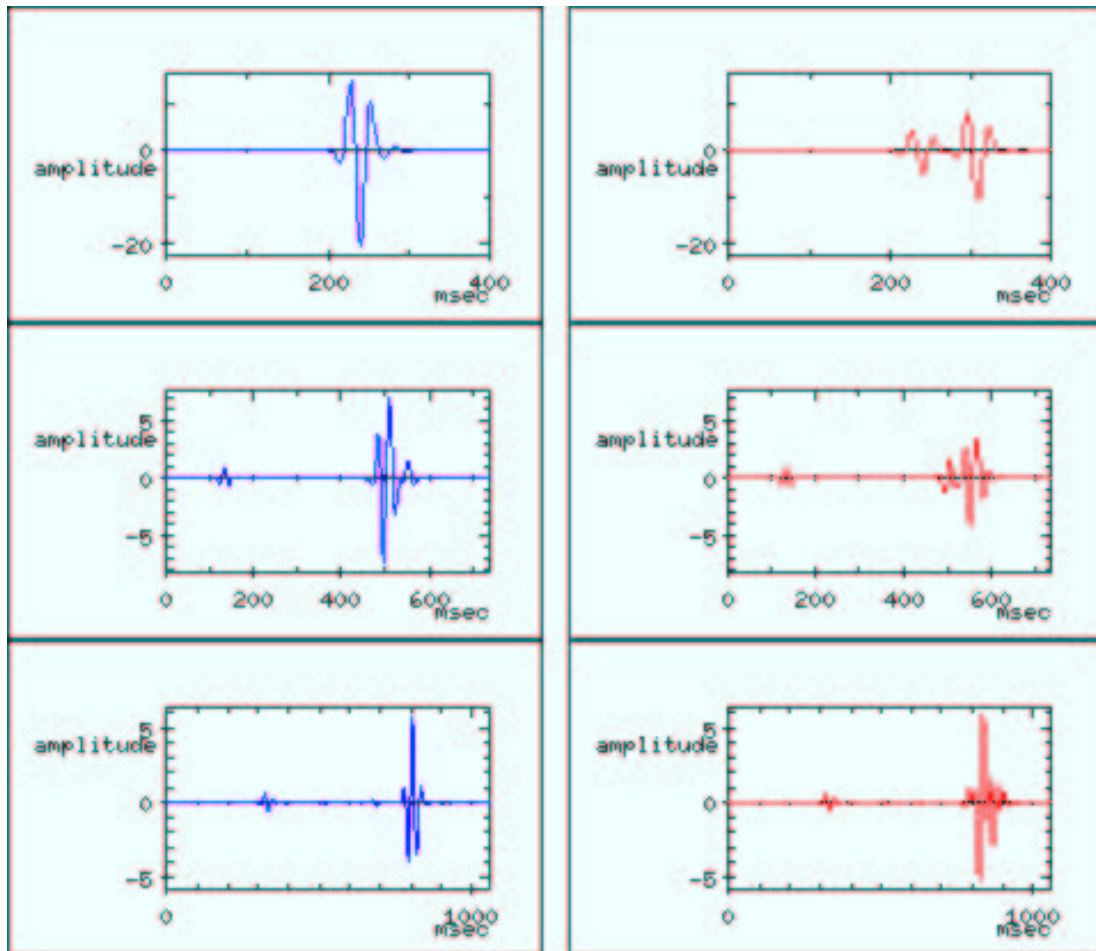
Figure 4.17: *Superimposed wavelets and their amplitude spectras.*
These wavelets are extracted from the seismograms based on the earth models constructed by Overburden 1, which has a low degree of attenuation, and Reservoir I (a dry reservoir) and III (a 50% saturated reservoir).
The illustration on top shows the wavelets extracted from trace 5, the one in the center; trace 100, and on the bottom, trace 155.
The blue wavelets represent the dry reservoir, while the red wavelets represent the saturated reservoir.
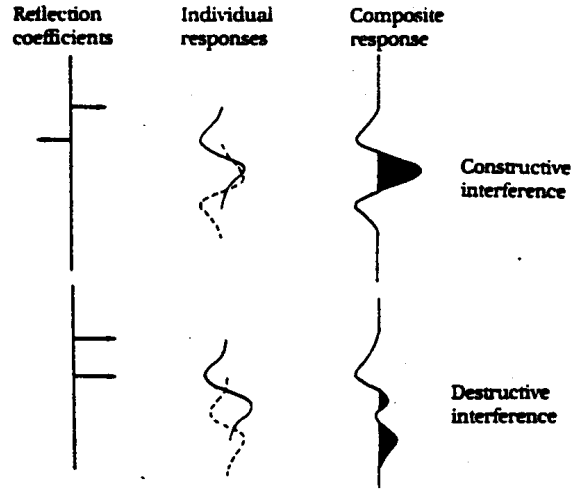
Figure 4.18: *Constructive and destructive interference for a signal with minimum phase and normal polarity.*

(Mavko et al., 1998);

$$I_p = \rho V_p, \tag{4.4}$$

$$I_s = \rho V_s. \tag{4.5}$$

The acoustic impedance further defines the reflection coefficient, and has therefore a great influence on the amplitude.

The reflection coefficient is defined in equation 3.9, and combining this with equations 4.4 and 4.5, gives the following definition;

$$R = \frac{\rho_2 V_2 - \rho_1 V_1}{\rho_2 V_2 + \rho_1 V_1} = \frac{I_2 - I_1}{I_2 + I_1}, \tag{4.6}$$

where the notation $_1$ and $_2$ indicate the first and second layer.

An other aspect of the impedance is that the greater the contrast in impedance between two layers, the greater the angle of refraction.

Calculating the acoustic impedance using the P-wave velocity for overburden 1, the two reservoirs I and III, and the basement, gives the following;

$$I_{Overburden\,1} = 5.076,36 \left(kg/dm^3\right)(m/s),$$
$$I_{dry} = 11.721,70 \left(kg/dm^3\right)(m/s),$$

$$I_{50\% \, sat.} = 6.278,00 \left(kg/dm^3\right) (m/s),$$
$$I_{Basement} = 11.200,00 \left(kg/dm^3\right) (m/s).$$

These numbers indicate that the contrast between the overburden and the dry reservoir is relatively big which gives a large amplitude at the top reservoir reflector, as opposed to what is found between the overburden and the 50% saturated reservoir. The exact opposite is the result when the two reservoirs are compared to the basement.

Looking at trace 5 in figure 4.17, one can see that the synthetic seismogram gives the same effect.

But in addition to the effects caused by interference between top and bottom reflectors, and the results from difference in impedance for the different layers, the attenuation in the two reservoirs has quite a contribution the the shape of the signal as well. The attenuation on a 50% saturated reservoir is a lot higher than for a dry reservoir, as displayed in table 4.3. This gives a greater loss of energy when a seismic wave passes trough a saturated reservoir. There will therefore be a considerable decrease in amplitude for this signal.

This effect is also clearly demonstrated for the near trace in figure 4.17.

Trace 100 & 155 Regarding trace 100, it is obvious that there is a higher degree of interference between the two reflectors, for both reservoirs settings. The same goes for trace 155, and with an even higher effect. This phenomenon is caused by the diminishing influence the thickness of the reservoir has on the total travel path. The separation between the two, will therefore be reduced with increasing offset.

There seems to be a change in phase for the top reflector in the case of the 50% saturated reservoir, while as for the dry reservoir the bottom reflector has a phase change. This leads to a difference in phase for the two reflectors, for both reservoirs, and for both trace 100 and 155. This results in a destructive interference between the two reflectors, and a decrease in amplitude for the signals.

Regarding the scaling of the amplitudes in figure 4.17, this reduction is very clear.

For trace 100 one can still see the effect of difference in impedance between the different layers involved. Due to a greater degree of interference for trace 155, this is no longer visible.

The amplitudes for the two different reservoirs are approximately equal at both trace 100, as well as trace 155. This is the result of the way the reflectors interfere with eachother (caused by offset, phase changes etc.). But from the near trace to these two traces at larger offsets, there is still an evident reduction in amplitude, which is most likely caused by the attenuation the wave has been exposed to throughout its travel path.

Comparing with a reference model

The get a better realization of the influence all the physical effects discussed above have on a seismic signal, reference models with minimal attenuation were simulated. Meaning that the models used had parameters identical to the once listed in tables 4.2, 4.3 and 4.4, except that Q_p and Q_s for all layers are given the value 10.000 to simulate an attenuation equivalent to non existing.
This way, when comparing the traces from two models representing the same scenario, the only thing causing their differences will be attenuation.

To illustrate the findings obtained, the synthetic seismogram showing a 50% saturated reservoir (figure 4.16) is compared to its equivalent reference seismogram. This synthetic seismogram is shown in figure 4.19.

Comparing these two seismograms shows a clear difference in amplitude. There is by far much more energy in the reflections in the reference model. Especially the PP- and the PS-reflections of the reservoir are much stronger indicated in the reference model. The lack of attenuation is evident.

To get a better illustration of just how large the effect of attenuation is, traces 5, 100 and 155 are extracted and compared (figure 4.20). The blue wavelets extracted from the reference model, while the red once represents the attenuating model.

The general trend for all traces is that the signals compared are more or less identical in shape when referring to phase and relative amplitude. The only difference is the absolute value of the amplitudes. The plots of the overlayed amplitude spectras shows this clearly; the difference between the wavelets if the loss of higher frequencies from the reference model to the model where attenuation is included. There is a loss of about 15-20 Hz for all traces.
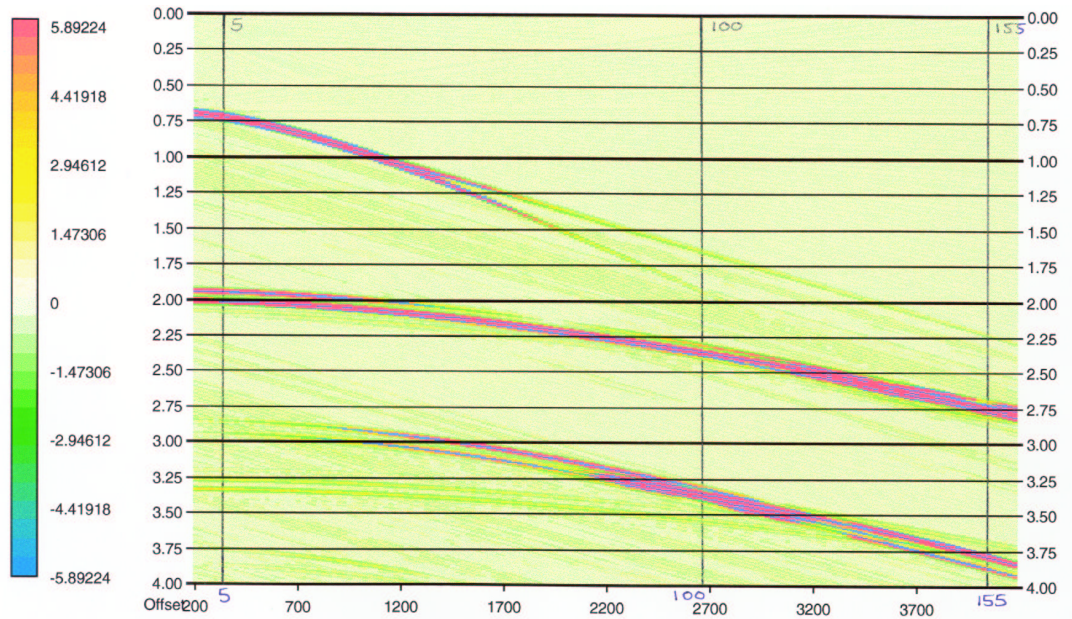
Figure 4.19: *Synthetic seismogram based on the reference model for the earth model constructed by Overburden 1 and reservoir III (50% saturated). The reference model means that the attenuation is set to be minimal. Traces 5, 100 and 155 are marked on the plot.*

Trace 5   Considering the traces one by one, the physical effects discussed earlier can be pointed out.

For trace 5, one can see the separation between the top and the bottom reflector. The shape of the two signals are very alike, except for the absolute values in amplitude.

The amplitude for the first reflector, the top reflector, is smaller for both models then the second one. This can be explained by the difference in impedance between the layers, as discussed earlier. And since this effect is present for both models, one can with certainty confirm that the difference in size for the two wavelets is in no way related to attenuation.

Trace 100   Trace 100 shows the same tendencies as trace 5. The shape is identical, and the loss of frequencies is approximately the same. The amplitudes has been reduced fairly considerably compared to trace 5, as one can see from the scaling of the $x-axis$. This may be explained by regarding the seismograms. These show that the top and the bottom reflectors have the opposite phase at
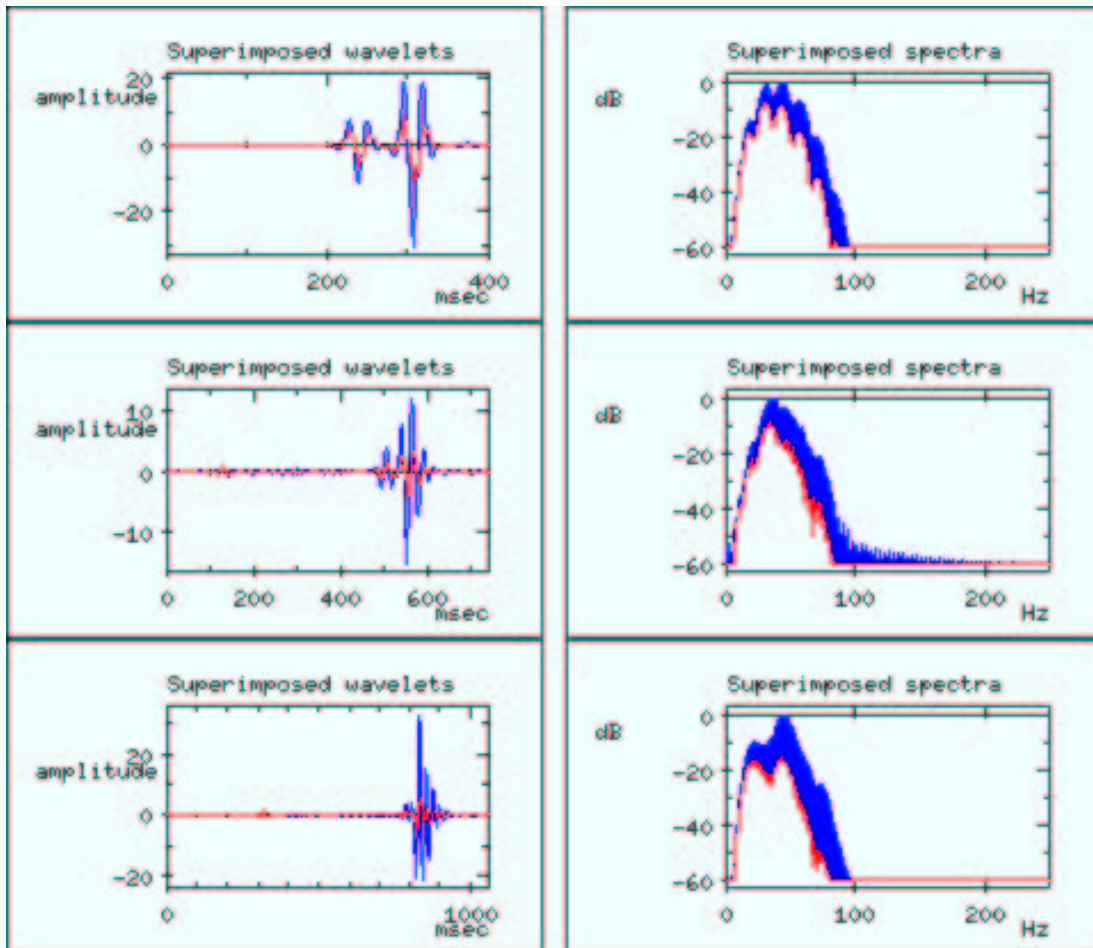
Figure 4.20: *Superimposed wavelets and their amplitude spectras.*
These wavelets are extracted from the seismograms based on the earth model constructed by Overburden 1 and Reservoir III (50% saturation), and its reference model.
On the top wavelets extracted from trace 5 are compared. In the center, wavelets from trace 100, and on the bottom wavelets from trace 155 are compared.
The blue wavelets represent the reference model with approximately no attenuation, while the red wavelets represent the realistic model.

this offset. This results in a destructive interference between the two wavelets, which further on causes a reduction of the amplitude.

Trace 155 Finally, trace 155 will be analyzed. Once again, one can see the great resemblance between the two wavelets. The shape is still very similar, but the difference in amplitude for the two models is larger than before. This might be explained by the fact that the top and bottom reflectors at the reference model has the same phase polarity, and will therefore interfere constructively, while the opposite is the case for the attenuating model. This explains the increase in amplitude for the reference model compared to trace 100.

The model with attenuation, however, shows a constant reduction in amplitude with offset, which most likely can be explained by attenuation.

4.4   Chapter summary

Throughout the modelling process, several different kinds of models have been generated and analyzed. They have been regarded as isolated models, and they have been compared to each other. To get a precise evaluation of the different effects wavelets are extracted, and then compared to other wavelets. This way it is possible to describe the changes of the signal from one setting to the next fairly accurate.

There is not enough room to show all the results obtained through all the modelling. Some examples have therefore been selected to illustrate the general tendencies found.

One of the first strong general trends found in the initial modelling is that one will see a larger difference, in both amplitude and phase rotation, between two wavelets compared, the larger the difference is in the Q_p-values in the settings these wavelets are extracted from. This is the reason why *case B* in the initial models always reveals the largest difference between the wavelets.

And another interesting observation made when analyzing these first and simplest models, is that the differences between the wavelets are considerably larger when both wavelets are exposed to a high degree of attenuation, opposed to if the attenuation has been low. This is totally independent of the relative difference in

Q_p-values between the wavelets. This is illustrated by the fact that for all initial models, *case C* showed a larger difference in amplitude and phase between the two wavelets, then what is the case for *case A*. And this is despite the fact that the relative difference in Q_p-factor for the wavelets in *case C* is smaller than for *case A*.

From the initial modelling it is also found that the 1-D Reflectivity modulus in Nucleus can not be used to analyze possible phase rotations between the two wavelets at large offsets, as it is done for the near traces.
The reason for this is, due to the equations used as foundation in Nucleus, that when the wave propagation is calculated, phase and amplitude is considered. This results in a phase change when the signal is being reflected at large offsets, due to the angle of incidence. So if one analyses the phase change, by using a Wiener filter generation, the resulting phase rotation will not merely be an effect of attenuation, but also the calculations made.

Problems with interference between the desired signal and crossing events like multiples etc. is found in both the initial and more realistic modelling. Due to a more complex composition of the realistic seismogram, this is a more common problem for these models. The interference makes it harder to extract only the signal of interest for further analysis.
In real seismic surveys this is a inevitable problem, which is one of the reasons it is so hard to regard attenuation as a isolated effect.

When analyzing the results from the more realistic models, it is evident to see that the attenuation of a seismic wave is larger when traveling through a partially saturated reservoir, than if traveling through a dry or a fully saturated reservoir. The attenuation is also quite higher for a fully saturated than for a dry reservoir. This is illustrated clearly through displaying the results obtained when comparing a wave traveling through a dry reservoir with a wave that has traveled through a 50% saturated reservoir.
But by performing this analysis, one will also be aware of other effects influencing the amplitude and the phase polarity of the signals.
Effects that is pointed out in this context, is e.g. the effect of contrast in impedance. If this contrast is large the amplitude of the reflecting signal will be equivalent large; and vise versa.
If the separation between two reflectors is small, these might not be separable due

to interference. And such a interference between wavelets might be constructive or destructive. Constructive interference will give an increase in amplitude, while destructive interference will give a reduction which must not be confused with attenuation.

Considering the comparison of one model with its reference model (which has approximately no attenuation), shows that a signal will go through identically changes in amplitude relative and phase despite the degree of attenuation found in the medium where it propagates.
Almost the only difference between these two models compared was the absolute value of amplitude. This shows that the changes in relative amplitude and phase caused exclusively by attenuation are minimal when compared to effects caused by other physical properties a signal is exposed to when propagating trough a medium.
But the loss off energy, displayed as reduction in absolute amplitude, caused merely by attenuation, is quite significant. For the example used here, the signal lost about 15-20 Hz in the higher frequency band.

Chapter 5

Attenuation effects in the overburden: Numerical examples

5.1   Introduction

In this chapter, an examination of the attenuation effects of the overburden is performed. Basic earth models containing a gas-cloud in the overburden are made, and synthetic seismograms obtained. Scenarios with different degree of saturation are executed.
An evaluation of the resolution powers of P- and S-waves is also done.

These synthetic seismograms are cross correlated with plots of the theoretically calculated reflection coefficients of the different wave types, to study effects on the amplitude due to the reflection coefficient. Obtaining a better understanding of these effects makes it possible to disregard AVO effects etc. when considering the effects of attenuation on a seismic signal.

Models with identical rock parameters, except for the Q-values, are in the following explored to better see the isolated effects of attenuation due to a gas-cloud in the overburden.

At the end, an analysis of the effect of attenuation is performed. This is done the see if the trends found for these models coincides with the conclusions made from previous modeling.

5.2 Modelling of seismic waves through a gas-cloud

The first part of this chapter is dedicated to the examination of the correlation between the seismograms and the plots of the reflection coefficients. One wants to find out it is possible to point out the changes in the seismic signal that are caused directly by the variations in the coefficients. This way these changes will not be mistaken for attenuation effects.

Further, based on the theory concerning resolution of seismic waves presented in section 2.7, experiments will be performed to appraise these powers for the different kinds of seismic waves.

The main focus is kept on finding the isolated effect of attenuation caused by the presence of a gas-cloud in the overburden. Models where only the values of Q_p and Q_s vary, according to the degree of saturation, are compared and evaluated.

5.2.1 Earth models

The earth models used here are kept simpler than the previous models. They only have three layers; a 500 m thick water layer, a 1.500 m thick overburden containing a gas-cloud, and finally a basement layer which is set to obtain a reflector underneath the gas-cloud.

The parameters used to specify the reservoirs of different degree of saturation (table 4.3) are in this case used to define different saturation scenarios for the gas-cloud situated in the overburden.
The bottom layer is defined by the parameters listed in table 5.1.

BASEMENT UNDER GAS-CLOUD						
	$d\,(m)$	$V_p\,(m/s)$	$V_s\,(m/s)$	$\rho\,(kg/dm^3)$	Q_p	Q_s
Basement	1000	2000	1000	2.31	200	100

Table 5.1: *The parameters defining the basement underneath the gas-cloud. Defined simply to obtain a reflector under the gas-cloud.*

One of the models is shown in figure 5.1. This model is based on the parameters used to simulate a gas-cloud with 10% saturation.
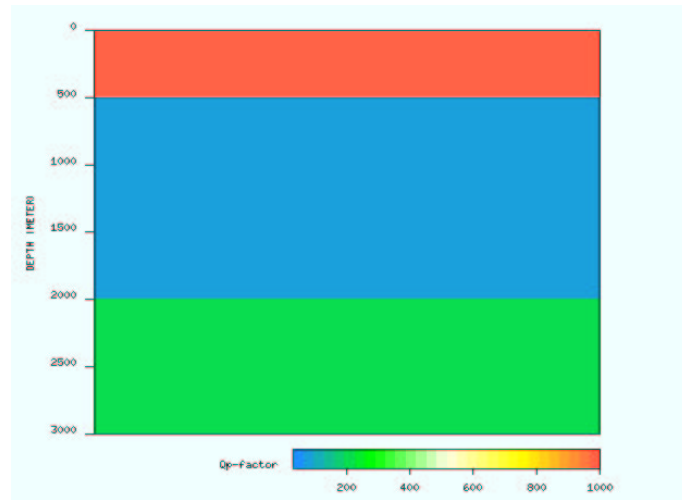
Figure 5.1: *Earth model used for modelling a gas-cloud with 10% saturation. Q_p is the plot parameter.*

5.2.2   The modelling

The first steps of the modelling are as explained under section 4.2.3, until the generation of the synthetic seismograms. The following wavelet analysis is not executed for the modelling performed in this chapter.

A plot of the reflection coefficients for both PP-, PS-, and SS-waves is made to be able to compare the events on the synthetic seismograms to the theoretical effects of AVO etc. Based on this analysis, conclusions concerning resolution powers of the different waves can be made.

The illustration of these coefficient is also made in *1-D Reflection* module in *Nucleus*; by using the option $Analysis \rightarrow Reflection/transmission\, coefficients$. Reflection from the top of the third layer is chosen. All combinations of wave reflection are desired; $P - P$, $P - S$, and $S - S$. The maximum angle of incidence is set to 89.9 degrees, meaning that the whole spectra is included. The maximum value for plotting is 1.0. Both modulus and phase is plotted.

5.3 The results

5.3.1 Observations

Synthetic seismograms

The objective for this modelling is to observe the effects attenuation in the overburden will have on the seismic signal. The focus is more specifically placed on how this will influence the amplitude and the phase distortion of the waves.
Further the results are explored to find whether the PP-, PS-, and SS-waves will be attenuated as outlined in section 2.7. Namely, that the PP-waves will have the best resolution at near offsets, while PS-waves give the best resolution for mid distance offsets. The SS-waves are expected to have the best resolution powers at larger offsets.

The results acquired from the modelling can be demonstrated clearly in figures 5.2 and 5.3.

Figure 5.2, shows the synthetic seismogram based on the earth model with a dry overburden. For this model the parameters are as follows; $V_p = 4.670\,m/s$, $V_s = 3.060\,m/s$, $Q_p = 500$, $Q_s = 375$, and finally $\rho = 2.51$.
To be able to evaluate whether the changes in energy of the seismic waves are caused by attenuation or by AVO effects etc., the different events on the seismogram needs to be identified, and explored.
As for the previous seismograms, the first break at 0.68 sec. is the reflection of the sea bed. The PP-, the PS-, and the SS-events from the top reservoir are found at 1.32, 1.49 and 1.66 sec., respectively.
At about 1.98 sec. there are two events coming in at approximately the same time; the PP interbed multiple, and the water multiple of the PP-wave. The PS-water multiple is located at 2.16 sec., while a new double event (the PS-multiple and the SS-water multiple) is found at 2.32 sec. Finally, at 2.64 sec., the SS-multiple is registered.

The synthetic seismogram of the earth model simulating a 50% saturated gas-cloud is displayed in figure 5.3. For this model the parameters are as follows; $V_p = 2.920\,m/s$, $V_s = 1.830\,m/s$, $Q_p = 30$, $Q_s = 60$, and finally $\rho = 2.15$.
The events on this seismogram are as follows; the reflection of the sea bed is

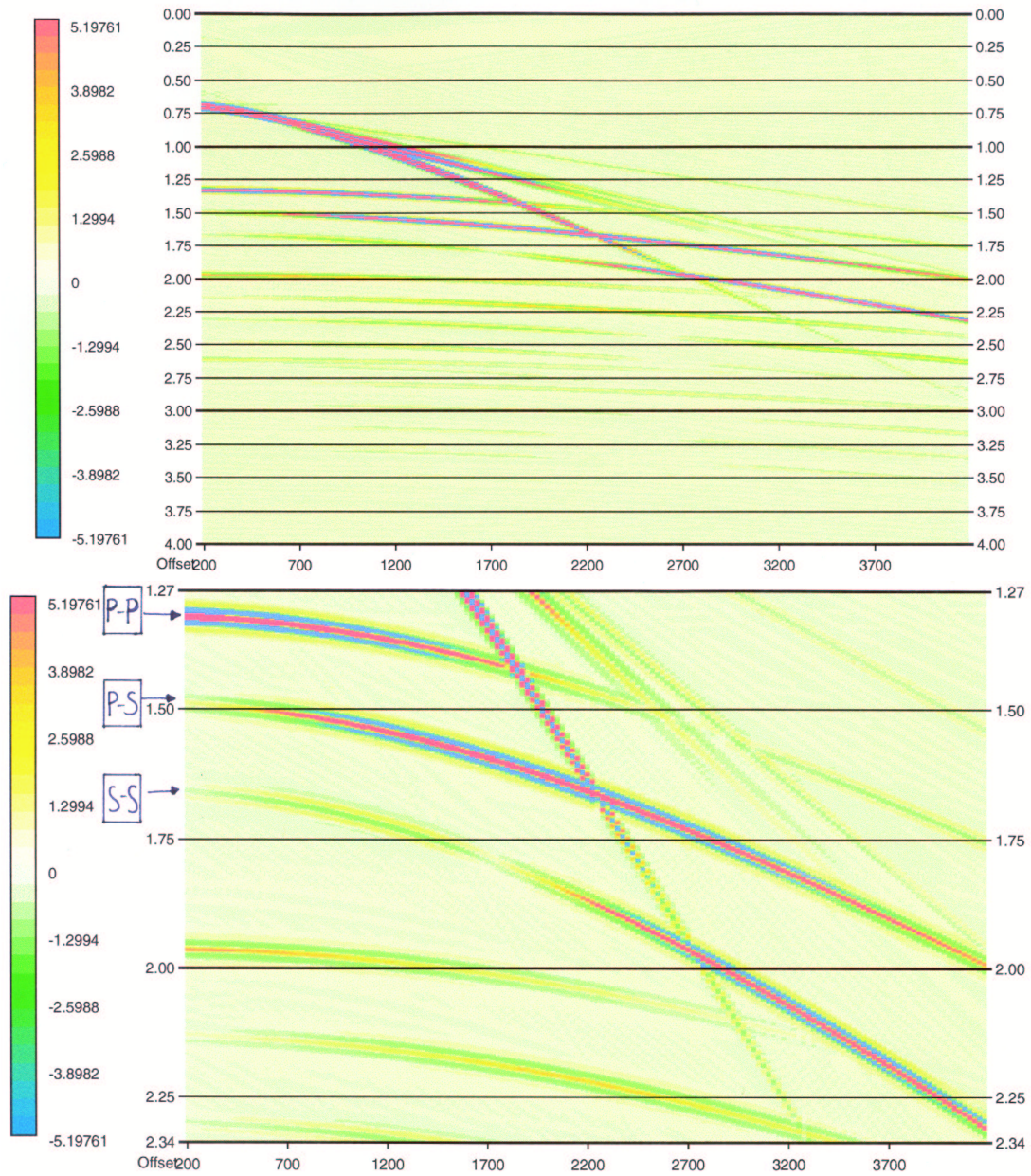Figure 5.2: *On top; the synthetic seismogram of an earth model illustrating a dry overburden. Under; the enlargement of the P-P, P-S and S-S reflections from the seismogram above.*
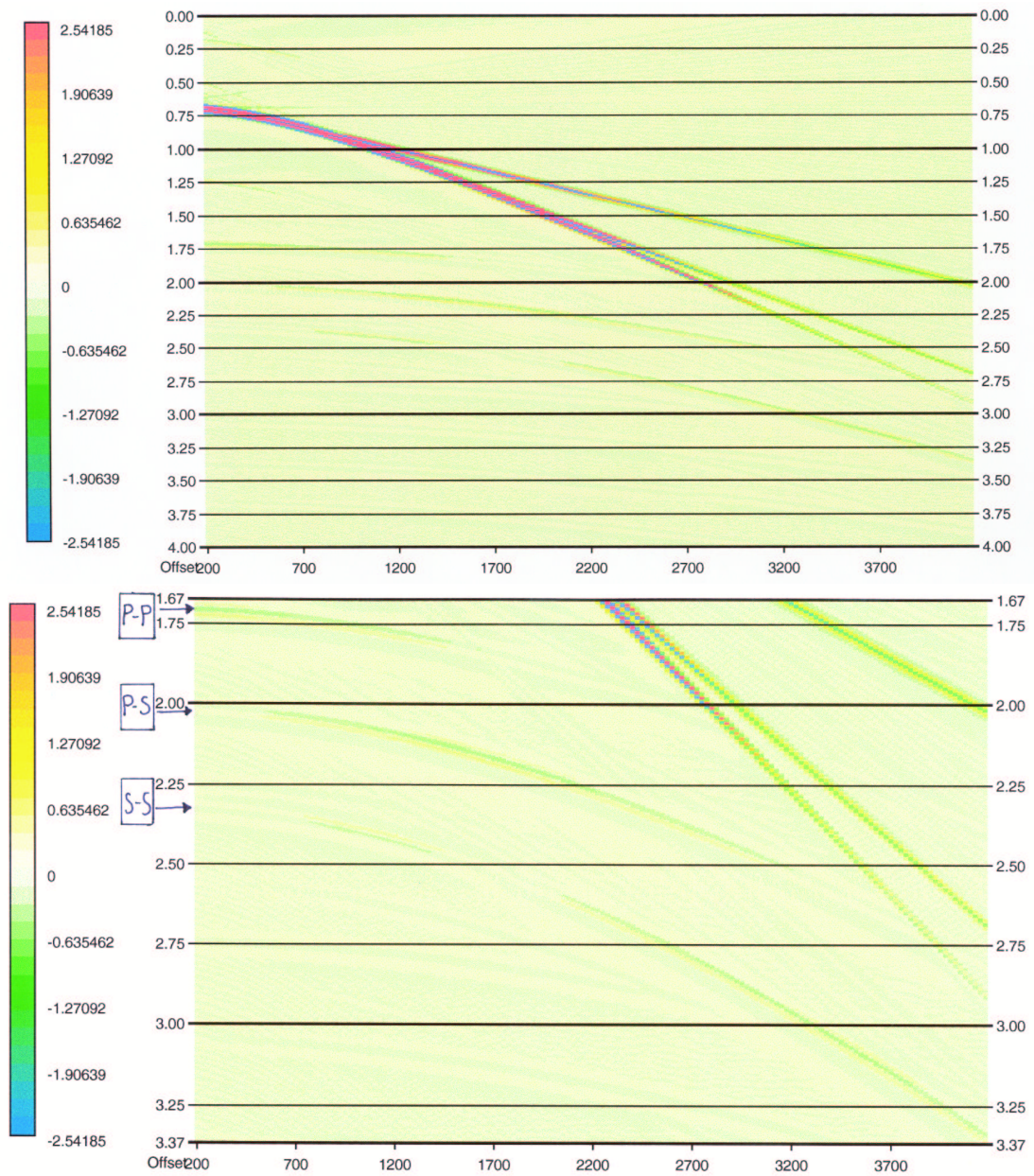
Figure 5.3: *On top; the synthetic seismogram of an earth model illustrating an overburden containing a 50% saturated gas cloud. Under; the enlargement on the P-P, P-S and S-S reflections from the seismogram above.*

as before, the first break at 0.68 sec. The events at 1.70, 2.01 and 2.31 are the reflections of the PP-, PS-, and SS-waves. Due to lower velocities, the events are displayed at larger travel times.

Reflection coefficient plots

When plotting the reflection coefficients, both modulus and phase are displayed. This gives the opportunity to evaluate the correlation between the changes in the absolute value for the amplitude, and the rotation in phase with offset on the seismograms.

Figure 5.4 gives the wave reflection coefficients for the model where the gas cloud in the overburden is dry, while figure 5.5 gives these coefficients for a model where the overburden contains a 50% saturated reservoir.
The different kinds of waves are identified through color-codes, which are defined in the top left corner of the plot. While the parameters V_p, V_s and ρ for the layers over and under the interface of interest are specified in the opposite top corner.

Comparing the seismograms and the plot of their respective reflection coefficients for these two scenarios, will give an idea of the reflection coefficients impact on the amplitude of the seismic signal. And due to this information, it is possible to separate these effects from the changes in the signal caused merely by attenuation. When examining the attenuation effects in the overburden, it is important to be aware of such factors that might influence the magnitude and the shape of the signal. If all changes in a signal is regarded as a direct result of the attenuation, this miss-interpretation leads to conclusions based on false assumptions. The variations in amplitude caused by the reflection coefficients are one of the factors that easily can be mistaken.
A thorough presentation of the correlation between these coefficients and the amplitudes at the seismograms is therefore given in the following.

Correlation

To correlate the synthetic seismograms to the reflection coefficients plots means that they are examined to evaluate the resemblance between the two. This way

Figure 5.4: *The reflection coefficients, both modulus and phase, for the P-P,P-SV,and SV-SV waves propagating through a dry overburden. Color codes for the different waves are defined on the top of the plot.*
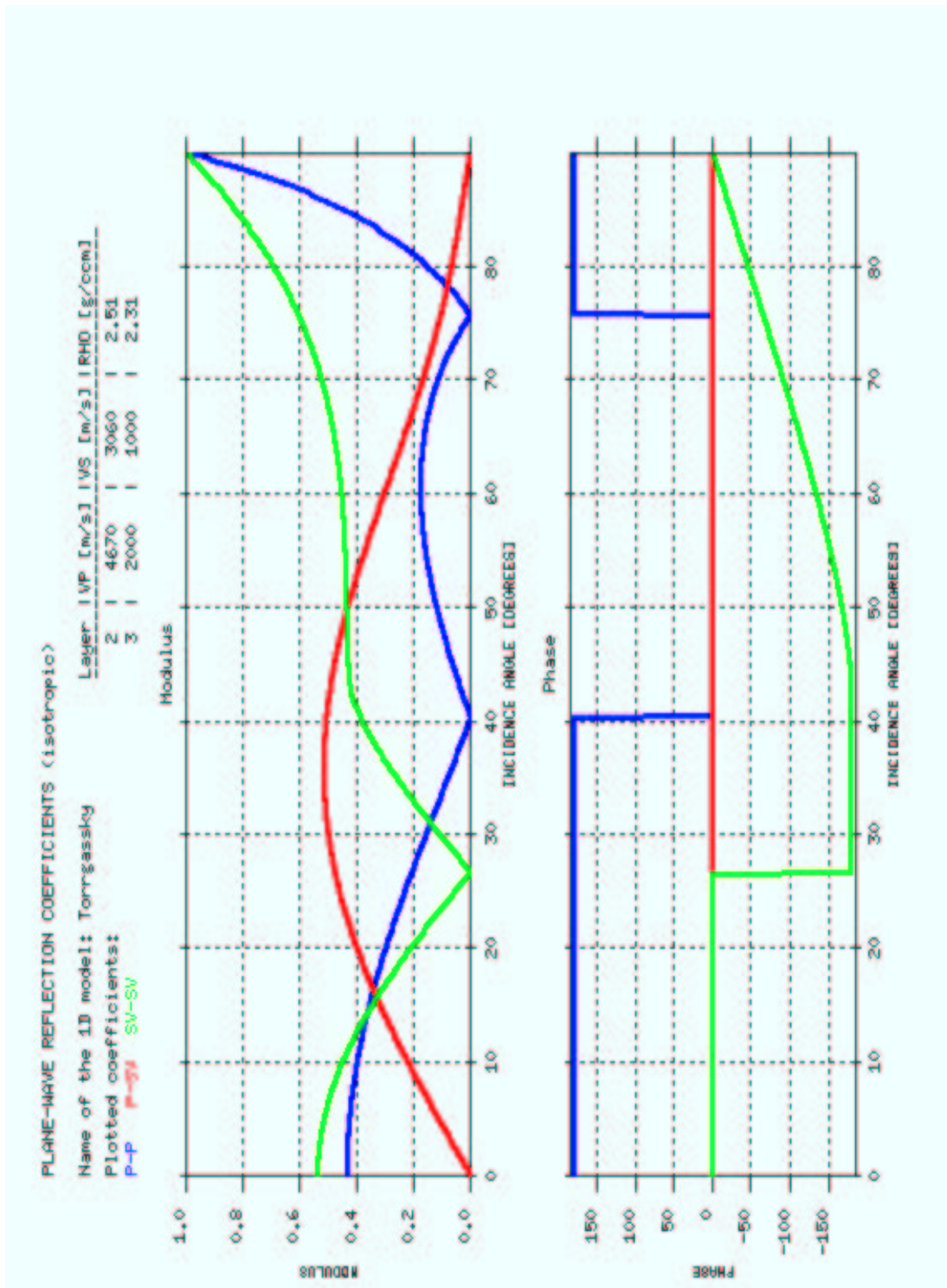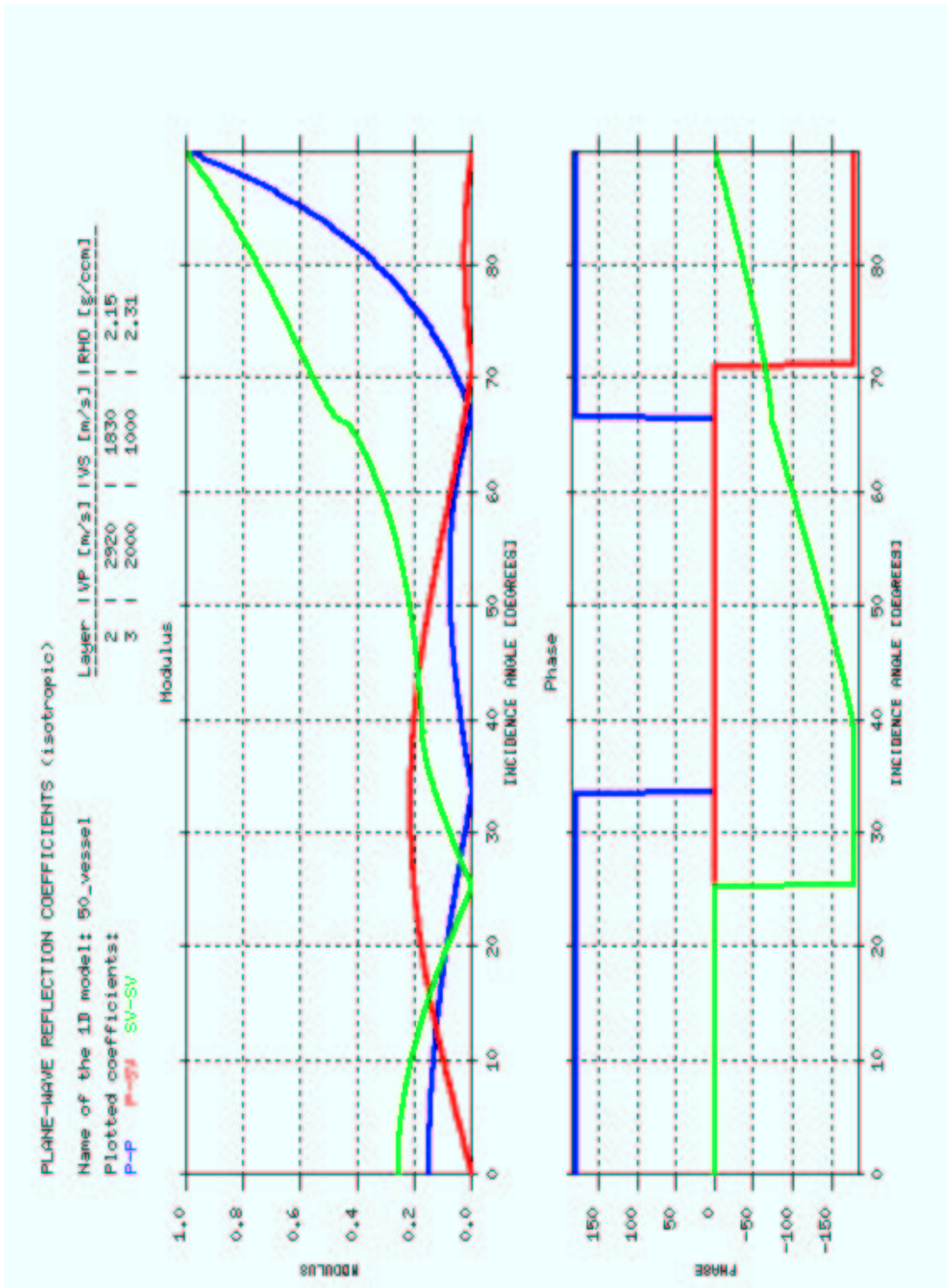
Figure 5.5: *The reflection coefficients, both modulus and phase, for the P-P,P-SV, and SV-SV waves propagating through an overburden containing a 50% saturated gas cloud. Color codes for the different waves are defined on the top of the plot.*

it is possible to find how much the events on the seismogram are controlled by the reflection coefficients.

Since the offset at the seismograms is given in meters (m), and in angle of incidence (deg) for the reflection coefficients, a conversion from one to the other is generated. The software *NORSAR - 2D ray modelling* is used for these calculations.

The graphs that illustrates the cross plots of offsets in kilometers and in angle of incidence are displayed in Appendix C.

Dry overburden

> **The P-P wave** reflection at the seismogram is at near offsets the strongest event of the three reflectors. It loses its energy rather fast, and at about $2.850\,m$ ($\sim$ 40 deg) the signal is hardly visible. After this point the phase changes polarity, and the amplitude starts to increase. The seismogram ends at an offset of $4.200\,m$ (52.7 deg), when the energy level of the amplitude is still weak.
>
> These results are exactly the same at the once found on the reflection coefficient plot.
>
> Initially **the P-S wave** reflection starts of with no energy at the seismogram. The amplitude equals zero at zero offset. This can only be illustrated in the coefficient plot, since the seismogram starts at an offset of $200\,m$ (4 deg).And the coefficient plot shows that at an incidence angle of 4 deg the signal will possess a small amount of energy, which coincides with what is found on the seismogram.
>
> With increasing offset the amplitude increases in magnitude, up until an offset of $2.000\,m$ at the seismogram which equals an incidence angle of 37.5 deg. At this offset the P-S reflection has its maximum amplitude. From there the magnitude decreases gradually. When the angle of incidence is 90 deg, the amplitude once again reaches zero. Since the seismogram only shows an offset up until $4.200\,m$ ($\sim$ 62 deg), this can evidently not be seen at the seismogram. But the tendency is clearly demonstrated.
>
> The phase stays at constant polarity for all offsets.

The findings found at both the synthetic seismogram and the coefficient plot show the same changes at the same offsets for the P-S wave.

Finally, a correlation of **the S-S wave** is done. At first is seems as is these two illustrations do not match. The plot of the reflection coefficients indicates that the S-S wave should have the highest initially energy level. But regarding the seismogram the exact opposite result is illustrated. Here the S-S event demonstrates the weakest initial amplitude of them all.

The reason for this phenomenon can easily be explained. These waves are all converted from the P-wave that travels through the water layer. This means that at zero offset, only P-waves will be transmitted down through the overburden. There will be no S-wave energy present. As soon as the P-waves has a certain incidence angle some of the energy will be converted to S-waves. Very little initially, but with increasing angle more and more energy will be converted. And this explains the lack of S-wave energy for small offsets at the seismogram.

At about $1.700\,m$ ($\sim$ 26 deg), the S-S reflection coefficient drops to zero. At this point the phase will also change its polarity. This can be observed at both the seismogram and the plot of the coefficients. The two illustrations also coincide on the fact that after this point the magnitude of the amplitude increases gradually with offset.

Overburden with a 50% saturated gas-cloud

Regarding the P-P wave reflection at the seismogram shows that the amplitude is absolutely strongest at very near offsets. Up until about $700\,m$ ($\sim$ 10 deg) the signal is quite strong. The magnitude of the amplitude decreases gradually until it equals zero at $2.300\,m$, which is equivalent to an angle of incidence of 33.5 deg. From there to larger offsets the magnitude of the energy increases slightly and the polarity of the phase changes. The increase in amplitude is barely visible at the seismogram.

At the maximum offset at the seismogram ($4.200\,m$, or $\sim$ 51.5 deg)

there is almost no energy left in the signal.

What is described above is found for both the synthetic seismogram and the reflection coefficients plot. The similarity is as good as perfect.

The magnitude of the P-S wave reflection starts of as zero for zero offset. But as mentioned above, the seismogram does not display the events from zero offset. The seismogram starts at a $200\,m$ offset, which equals an angle of incidence at ~ 4 deg. But the tendency that the amplitude is initially very weak, and that it increases in magnitude with offset until it reaches its maximum at $1.800\,m$ (~ 33 deg) is found in both the seismogram and the coefficient plot.

From this point the amplitude decreases with offset until it reaches zero at an incidence angle of about 71 deg. The total effacement is not illustrated at the seismogram since it is only made for an offset of $4.200\,m$ (~ 61 deg), but up until this point the tendencies are identical for the two illustrations.

The phase stays constant throughout for all the offsets displayed on the seismogram.

Initially, the magnitude of the reflection of the S-S wave at the seismogram does not coincide with the magnitude shown in the reflection coefficients plot. This is for the same reasons as described under the section analyzing the dry overburden.

At an offset of $1.800\,m$ (~ 25.5 deg) the amplitude equals zero. For larger offsets the magnitude of the amplitude increases gradually. The phase also changes its' polarity after this point. This is found for both the synthetic seismogram and the coefficient plot.

As described above the correlation between the changes in the seismic signal found in both the seismogram and the reflection coefficients plot is very good. This leads to the conclusion that the parts of a seismic signal where the amplitudes are reduced in magnitude is not merely a result of attenuation. In fact, it seems as if the local value of the reflection coefficient controls the energy level of the signal just as much.

The initial assumption that attenuation alone is the reason why PP-waves has a higher resolution power at near offsets, while SS-waves gives the best resolution

at far offsets seems therefore to be wrong. Attenuation will give the same tendencies, but the values of the reflection coefficients seems to highly control this phenomenon too.

5.3.2   Comparison of gathers with and without attenuation

Not only the values of Q_p and Q_s vary in the models displayed above. Along with the Q-factor, velocities and densities are also changed from one model to the next.

As a direct consequence of such multi-variations, affecting both the amplitude and the phase of the signal, it is extremely difficult to extract the changes of the signal caused only by attenuation. But now that the reflection coefficients effect on a signals amplitude has be acknowledged, it is easier to explore the isolated effect of the attenuation in the overburden.

For the following two models, the velocities and the densities are kept at the same values as for an overburden containing a 50% gas saturated gas-cloud ($V_p = 2.920 \, m/s$, $V_s = 1.830 \, m/s$, and $\rho = 2.15$). But the Q_p- and Q_s-values are changed for both cases.

For the first model (figure 5.6) the attenuation is practically eliminated. Both Q_p and Q_s is set to equal 10.000. This model can be regarded as a reference model, to see how the events would behave without the influence of attenuation in the overburden.

The second model (figure 5.7) has "adopted" the Q-values from a 10% saturated gas-cloud ($Q_p = 50$ and $Q_s = 110$). A study of the events displayed in this figure will reveal if there are detectable differences in the signal caused merely by attenuation, large enough to differ between to degrees of saturation.

Both figures illustrate only the enlargements of the PP-, PS- and SS-events from the top reservoir.

Figure 5.6 shows the seismic events from the seismogram based on the same velocities and density as a model containing a 50% saturated gas-cloud in the overburden, but without attenuation.

One can clearly see that the tendencies of amplitude variations with offsets are

Figure 5.6: *The PP-, PS- and SS-events from a seismogram based on a earth model with both velocity and density parameter values as for an overburden containing a 50% saturated gas-cloud, but with Q-values set to equal 10.000.*

the same as for the events at the seismogram showing a 50% saturated overburden in figure 5.3.

But still, the most striking observation when comparing the two plots is that the amplitudes are a lot stronger in the figure displaying the events from the model with practically no attenuation in the overburden. And this difference is in all reality caused by attenuation alone. The changes with offset can be explained through e.g. AVO effects, as demonstrated in the section treating *correlation*.

The phase polarity seems to be identical for the two, meaning that the attenuating effect is limited to a massive loss of energy, and practically no visible change in phase.

Figure 5.7 shows the seismogram based on the same velocities and density as a model containing a 50% saturated gas-cloud in the overburden, but with *Q*-factors corresponding to a 10% saturation. When comparing the events on this seismogram to the PP-, PS- and SS- events in figure 5.3, the amplitude variations with offsets are still in accordance with eachother.

And even though the modulus of the amplitudes for the events displayed in figure

5.7 are quite a lot weaker than for those displayed in the reference model (figure 5.6), they are still stronger than those in figure 5.3. The absolute difference in amplitude between the model representing an overburden with a 50% saturated gas-cloud, and the one using Q_p and Q_s values corresponding to a 10% saturation, is of such a magnitude that is is visible for the bare eye on a seismogram.

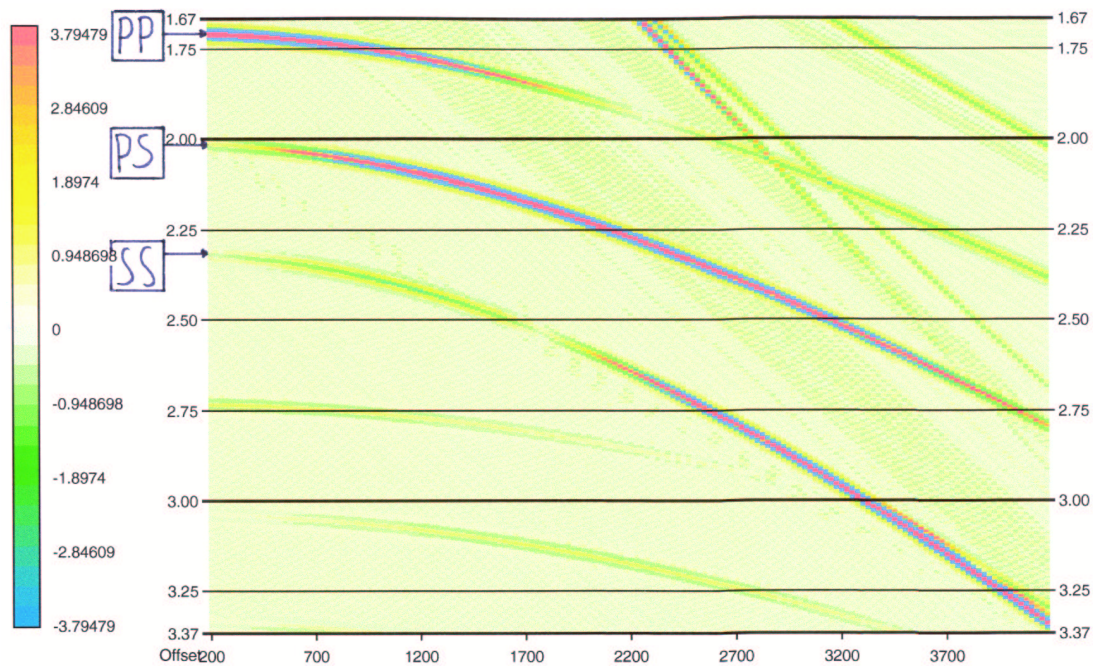In this case it also seems as if the phase polarity is the same for both cases.
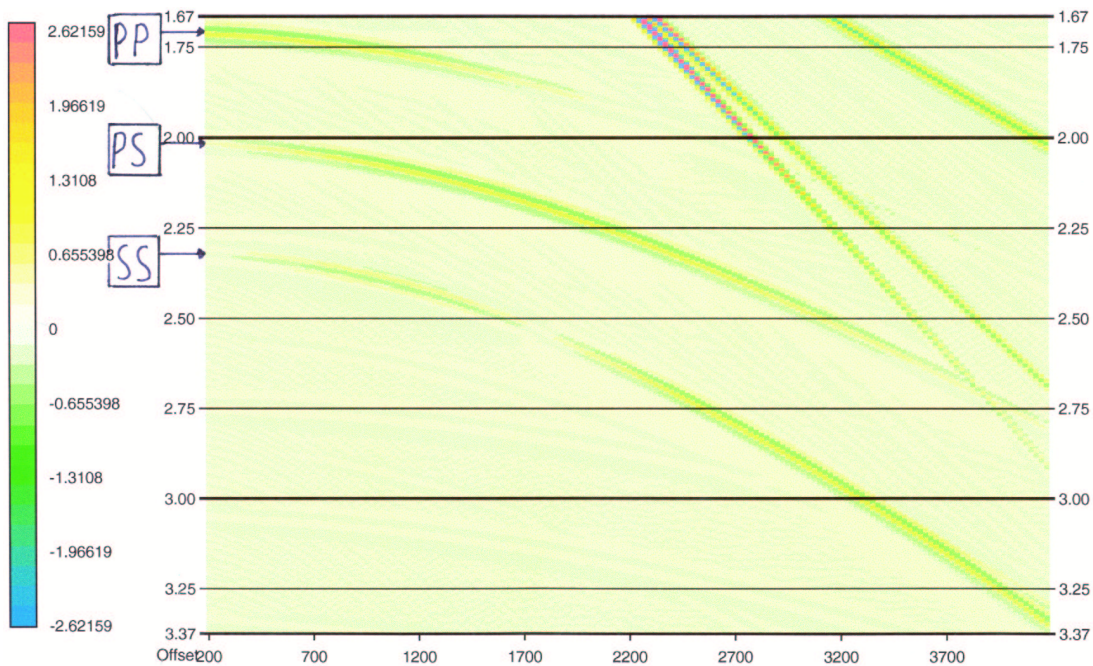
Figure 5.7: *The PP-, PS- and SS-events from a seismogram based on a earth model with both velocity and density parameter values as for an overburden containing a 50% saturated gas-cloud, but with Q-values representing a 10% saturated gas-cloud.*

These two comparisons clearly illustrates the magnitude of the attenuation a gas-cloud in the overburden has on the seismic signal.

This reduction of energy from one scenario to the next is through these illustrations proven to be so pronounced that it is even possible to separate different degrees of saturation apart when examining seismograms.

A further verification of these results will be presented in the following chapter.

5.3.3   The effect of the presence of a gas-cloud

To evaluate the attenuating effect caused by the presence of a gas-cloud in the overburden it is necessary to compare more than just the two initial models generated. Due to the fact that several rock physic properties differ in these scenarios makes it impossible to conclude anything about the sole effect of attenuation on the signal. The changes in the other parameters, such as velocity and density, along with varying offsets, will also effect the signal.

The examination of these models, and the correlation with their reflection coefficients, is therefore mainly performed to give an understanding of *other* effects that will influence the seismic signal.

It is by regarding models which basically are identical, where only the value of Q varies one truly can observe the effects of attenuation. This is what is done in the second part of this chapter. The attenuating effects caused by the presence of a gas-cloud is therefore best illustrated in these explorations.

The most conspicuous attenuating effect is the massive loss of amplitude found when a gas-cloud is inserted into the overburden.

By regarding the seismograms illustrated in figures 5.3, 5.6 and 5.7 it is evident that there is a large difference in energy level for the PP-, PS- and SS-events. It is also worth noticing that the scaling of the colors is not the same for the three plots. This means that the amplitudes from the reflector are even stronger in magnitude for the case of no attenuation ($Q = 10.000$) in the overburden than what it seems at first glance.

An other effect that is caused by the attenuation due to the presence of a gas-cloud is that the seismic waves are exposed to a stronger reduction of energy with offset, than what is found when attenuation is eliminated. This is basically an effect caused by a longer travel path when the offset increases. This can also be seen if comparing only the two initial models; a dry overburden with a 50% gas-saturated overburden. Since Q_p and Q_s are a lot lower for the saturated overburden than for the dry overburden, one can see that the signal loses its energy at nearer offset when a gas-cloud is present than what is the case for a dry overburden.

It seems as the attenuation in the overburden caused by the presence of a gas-cloud does not result in detectable phase distortion. The phase seems to stay

more or less constant.

5.4   Chapter summary

This chapter treats questions concerning the resolution powers of P- and S-waves. As concluded in section 2.7, theoretically the P-waves should have the best powers since $\lambda_p \succ \lambda_s$, and attenuation is defined as loss of energy per cycle. For the same distance the S-wave will have more cycles than a P-wave, and thus undergo a larger degree of attenuation. But when traveling through a medium saturated with liquid this will change.

A P-wave will, when traveling through a fluid saturated rock, be strongly attenuated by the fluids (chapter 2.5). While a S-wave on the other hand, who is not able to propagate through the fluid, will only travel in the rock frame and therefore not undergo the same massive attenuation as the P-wave does. The S-waves will thus keep its energy for larger offsets.

The focus in this part of the modeling was to see if this theory actually coincides with what is found in seismic. The results obtained in the synthetic seismograms generated, correlated with plots of the reflection coefficients for each case, shows very clearly the same results as expected from a theoretical point of view. But whether or not this is caused solely by attenuation is questionable. Through the examinations performed in this chapter, it seems as if the value of reflection coefficients highly influence the energy level of the waves, and that the variation in resolution powers therefore can be explained by these effects as well. S-S waves will for larger offsets possess a higher resolution power for larger offsets than both P-P, and P-S waves. And if the source is placed on the sea bed itself these waves will give the best resolution for all offsets.

A demonstration of the attenuation effects in general, to support the findings in previous chapters is also done in this chapter. A massive loss of energy as a direct consequence of higher attenuation (lower values of Q) is found through these explorations. The amplitude is heavily reduced when attenuation is present, as in this case due to a gas-cloud. It is also found that the energy loss is sensitive to the degree of attenuation the signal is exposed too. Meaning that it seems possible to be able to distinguish between different saturation degrees.

As for attenuation causing changes in the seismic signals phase, no visible effect is found. This coincides with assumptions made based on the findings in chapter 4.

The isolated effect of varying attenuation in the overburden will be treated further in the next chapter.

Chapter 6

Attenuation modelling from well data - the Jotun field

6.1 Introduction

To verify the validity of the results found in the previous modelling, this last part of the thesis is dedicated to a real set of seismic data. These data originates from the Jotun field in the North Sea.

To better be able to compare the results with models made in the previous chapter, it has been tried to keep the structure of the models a similar to the once already explored . The models are therefore constructed with a gas-cloud in the overburden over a reservoir.

This exploration was initially conducted with parameters that were identical or very close to identical to those found in wells at the field or obtained from check shots.

The complexity of these initial models made it necessary to make a smoothing over the earthmodel.

These steps are explained more in section 6.3.

Depending on the results obtained from these models, previous work will either be verified or enfeebled.

103

6.2 The Jotun field

6.2.1 General information

The Jotun field was first discovered in 1994, and it is located about 200 km west of Stavanger, Norway. More specifically on the Utsira High in the South Viking Graben between the Balder and Heimdal fields (figure 6.1). The Jotun field consists of the three geological structures; Elli, Elli South and Tau West, with Elli being the main reservoir (Drottning et al., 2002).
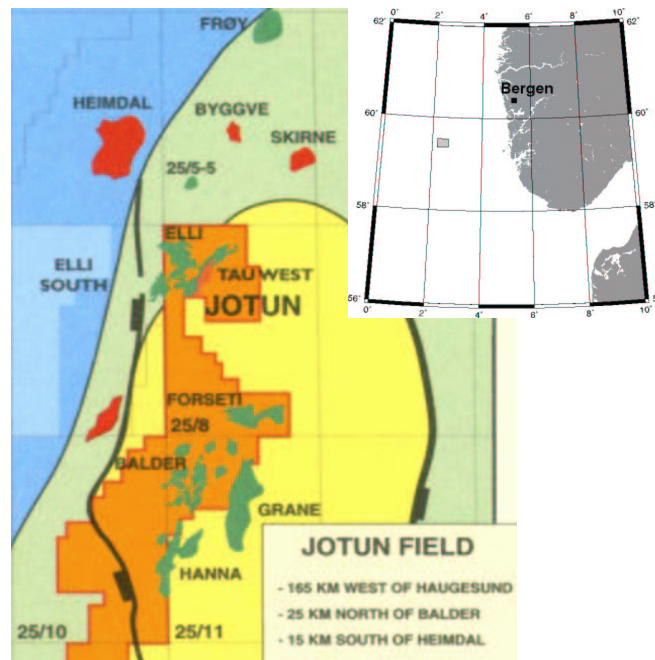
Figure 6.1: *Jotun is located on the Utsira Hitra between the Balder and Heimdal fields, approximately 200 km west of Stavanger (Drottning et al., 2002).*

Jotun is operated by Esso Norge AS, in blocks 25/8 and 25/7. Esso holds about 45% of the total reserves, while Enterprise, Conoco, Statoil and Amerada Hess hold the remaining interests.

It is developed by the floating producing and storing unit *Jotun A*, and the wellhead/drilling platform *Jotun B* (figure 6.2).

The ships arrived at the Jotun field in August 1999, and the production started the 25th of October the same year.

Figure 6.2: *Jotun is developed by a wellhead platform, tied back to a floating production vessel. Oil will be exported by shuttle tankers (Dick & Guargena, 2002).*

The 4×5 km Jotun reservoir lies in a paleocene basin where the turbidite sands from the Shetland Platform sequentially onlap onto the Utsira High. The average water depth in this area is 126 m, and the oil/water contact is located to 2.091 m below the seabed. The oil-column thickness in the exploration wells ranges from 18 to 46 m, with a small gas gap being presented in the Tau structure only.

The well log data used in this modelling are provided from well $25/8 - 6T2$. This well is an appraisal well, situated on the Elli structure.

The reservoir in Elli is good Upper Heimdal sand (porosity $\approx 27\%$, permeability ≈ 4 D), deteriorating in the Tau structure. Shales are few, but may be correlated over the whole basin until they pinch out on east Tau.

Recoverable reserves are estimated at approximately 200 million barrels of oil (32 million m^3) and a billion m^3 of gas.

6.2.2 Description of the data

This modelling is based on data extracted from well $25/8 - 6T2$, and from check-shots done at the top of this well. The physical parameters obtained from these data are listed in table D.1 in D.

The log data are sampled at intervals ranging from about 5 to 25 cm along the well trajectory beneath the starting depth at about 1.000 m. The P- and S-velocities, bulk density and gamma ray logs are parameters obtained from the data to describe the scenario at the location (figure 6.3). Additional parameters such as porosity, clay content and water saturation are provided in conjunction to the reservoir zone interval only.
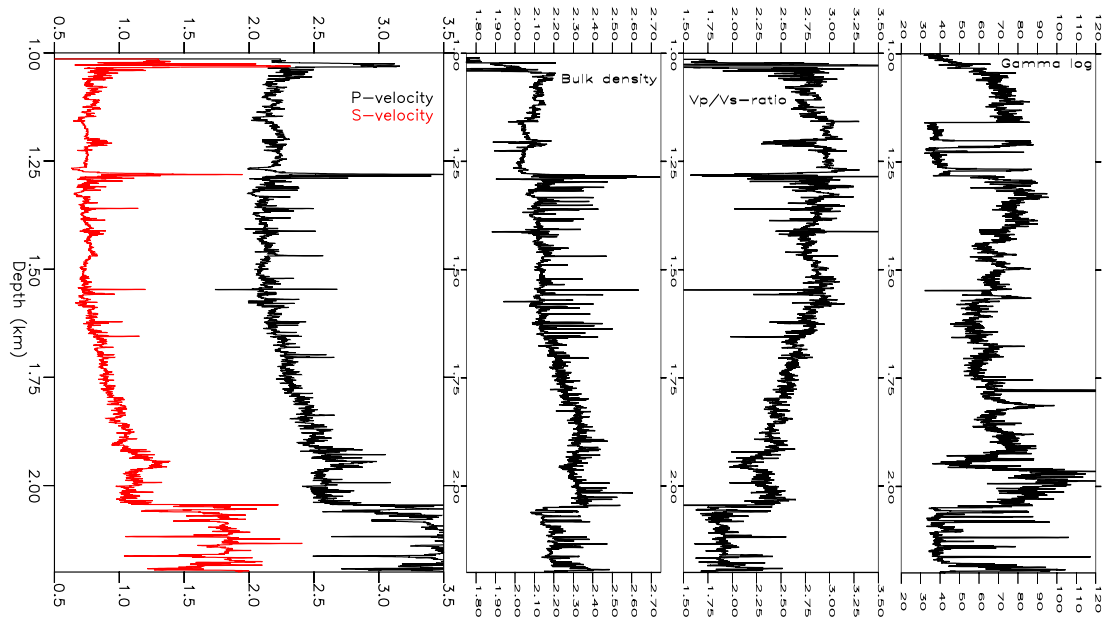
Figure 6.3: *Well logs from the $25/8 - 6T2$ well on the Jotun field.*

6.3 The modelling

In this part of the modelling, the receiver used to record the information from the survey is not a streamer as used in the previous modelling. In this case OBSs are made use of instead.

The reason for this is that in the top layers of the earth, the sediments are not fully consolidated. Thus the very little of the energy of the upward S-waves will be transmitted to P-waves through the water layer. The weak transmission coefficients due to the low S-velocities in these layers are the reason for this. An OBS placed on the seabed will therefore better register the P-S and the S-S converted waves, than what a streamer will.

The initial earthmodel made, based on the data from well $25/8 - 6T2$, and its check-shots, was a rather complex model with thin layers and in some cases small differences between the rock physics parameters (table D.1 in Appendix D). Because of this, it was very hard to both identify, and separate the different events on the seismogram (figure 6.4). Especially the reflector of the top reservoir (layer 25 in table D.1), which is the main focus for this modelling, is hard to indicate. The layers are particularly thin in the reservoir zone, which means that all the reflections and multiples from these interfaces will interfere on the synthetic seismogram.

This situation is extremely common, and as mentioned earlier, this is one of the reason why studying the effects of attenuation is nearly impossible on real data.

Figure 6.4: *The synthetic seismogram generated from the initial earth model made from the well data and the check-shots.*

Necessary adjustments are therefore made, so that it is possible to observe the effects of a partially saturated gas-cloud has on attenuation and resolution powers on the different waves.

To be able to get a better understanding of the attenuation effects in real data, a new earth model is made where the number of layers is reduced.

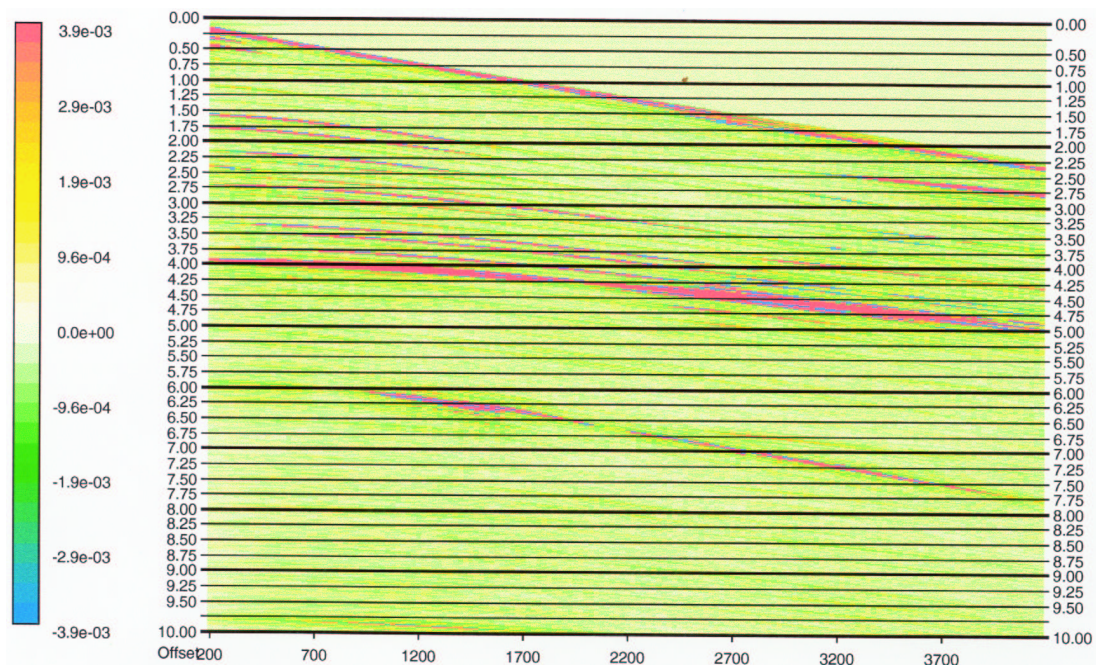A smoothing of the initial earthmodel is the basis of this reduction. 3 or 4 layers are combined and made to one in the overburden. The velocities and density for each of the new layers are found by taking the arithmetic average of the original values (table 6.1).

The parameters for the water layer is keep the same. But all the thin layers forming the reservoir (layers 25-36) are combined to one; layer 8 in table 6.1. And since the top reservoir reflector is the target event of this modelling, the basement is omitted.

Smoothed version of well $25/8 - 6T2$						
	$d\,(m)$	$V_p\,(m/s)$	$V_s\,(m/s)$	$\rho\,(kg/dm^3)$	Q_p	Q_s
Layer 1	128	1476	0	1.04	10.000	10.000
Layer 2	107	1807	446	1.95	10.000	10.000
Layer 3	409	1935	547	2.05	10.000	10.000
Layer 4	380	2108	686	2.18	10.000	10.000
Layer 5	314	2196	756	2.26	10.000	10.000
Layer 6	319	2124	714	2.20	10.000	10.000
Layer 7	307	2434	948	2.39	10.000	10.000
Layer 8	200	3289	1726	2.19	10.000	10.000

Table 6.1: *The parameters used to define the smoothed version of the original earth model.*

The Q_p and Q_s values are both set to equal 10.000 in both the initial earth model (parameters listed in table D.1) and in the altered model (table 6.1). This is because both these models work as reference models, and for these kinds of models it is desired to know how the results would be without the influence of attenuation. This way it is easier to find the effect and impact attenuation due to saturation has on seismic waves.

These values of Q_p and Q_s are varied for each model. The value of these parameters in the overburden is changed to simulate the attenuating effects found in the overburden due to the presence of a gas-cloud. Meaning that the values of Q_p and Q_s used to describe different saturation degrees in reservoirs listed in

table 4.3, are inserted into the earthmodel based on the real Jotun data. If e.g. we want to simulate the effects of a 50% saturated gas-cloud in the overburden in these real data, $Q_p = 30$ and $Q_s = 60$ are used values for the attenuation in layers 2 to 7 in the altered earth model from the Jotun data. The velocities and the densities are keep the same as in the reference model despite varying degree of gas saturation.

The steps for creating this earth model and the synthetic seismograms are as described in section 4.3.2. The recording length for the vessel is increased to 8.000 ms, to ensure that the SS-event will also be included on the seismogram. To be able to see the PP-, PS- and SS-reflections from the top reservoir more clearly, these events are zoomed in.

Since the velocities and the densities are kept constant and independent of the degree of gas saturation in the overburden, the reflection coefficients are the same for all the models explored.
The plot of these reflection coefficients are made as described in section 5.2.2.

6.4   The results

6.4.1   Description of the observations

Synthetic seismograms   The object of using real data and conduct the same explorations as done in chapter 5 is to see if the tendencies found in the results of modelling based on fictitious data are the same as for real data. In other words, to see if it is possible to apply the conclusions made on a theoretical level, on real seismic data.

Seismic resolution powers are primarily explored in this modelling. This is performed in the same manner in the previous chapter (chapter 5).
Synthetic seismograms are studied visually, and correlated with plots of the reflection coefficient for the reflection of interest. In this case that is the top reservoir reflector.

Due to the complexity of the events on the seismogram, it is found necessary to enlarge the PP-, PS- and SS-events from the top reservoir reflector. This way it

is easier to study the variations in amplitude with offsets, and to correlate these findings with the plot of the reflection coefficients.

The main object is still to explore how attenuation due to the presence of a gas-cloud effects the seismic signal in real data, and to see if the results coincide with the findings from chapter 5

In this chapter models with overburdens saturated with 10% and 50% gas, and a reference model with approximately no attenuation ($Q = 10.000$) will be illustrated. These models are chosen since the same scenarios are presented in the previous chapter, and the results will therefore be easier to compare.
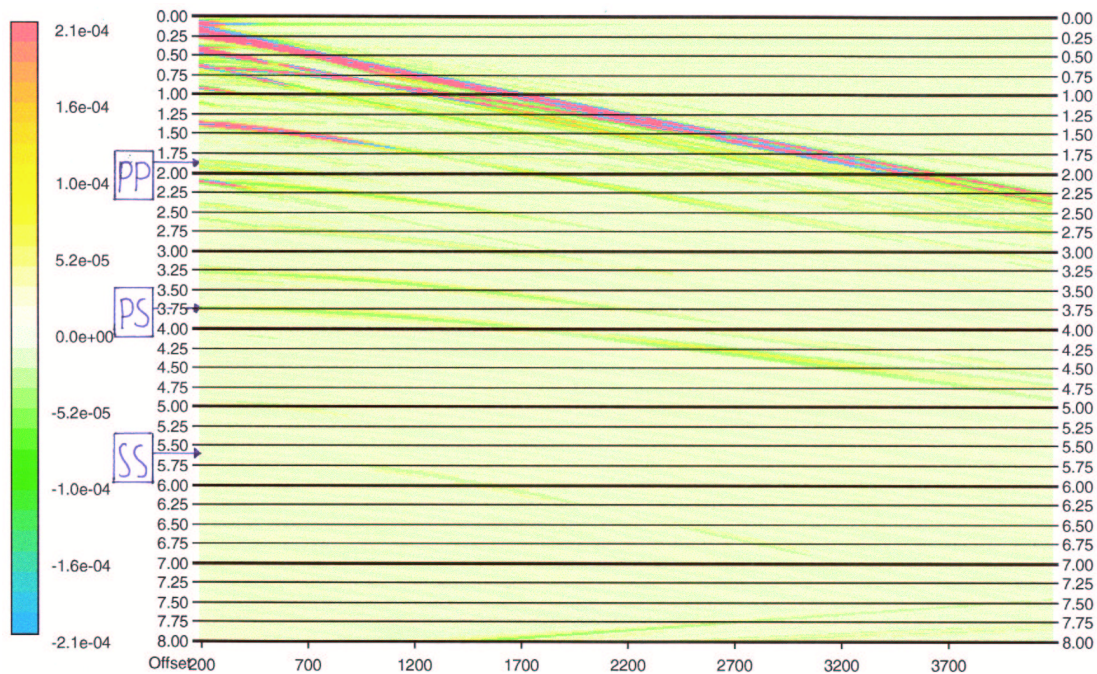
Figure 6.5: *The synthetic seismogram based on the altered version of data extracted from well $25/8 - 6T2$ from the Jotun field. The Q_p and Q_s values used for the layers in the overburden represents a 50% saturated overburden.*

Figure 6.5 shows the synthetic seismogram based on the modified well parameters describing the Jotun data, but with Q-factor values representing a 50% saturated gas-cloud present in the overburden; meaning $Q_p = 30$ and $Q_s = 60$.
The seismograms displaying the other scenarios are very similar. The only difference is the amplitudes magnitude for the events. For this reason, figure 6.5 is the only complete seismogram from these models displayed in this chapter. In

the following, only the enlargements of the events of interest will be displayed.

The seismogram displayed in figure 6.5 shows several events. Due to the complexity of reflections, multiples, different conversions between P- and S-waves, and interference between these, it is rather difficult to identify all the events.
But through calculations it is found that the PP-reflection from the top reservoir is the event at 1.83 sec. The PS-reflection is found at 3.68 sec, and the SS-reflection at 5.54 sec.
As mentioned above, the events of interest are enlarged from the synthetic seismograms, and displayed separately. Figure 6.6 shows the PP-, PS- and SS-reflections from the top reservoir of the model simulating an overburden containing a 50% saturated gas-cloud ($Q_p = 30$ and $Q_s = 60$).

Reflection coefficient plot   Since the velocities and the density of the layers are kept equal for all models explored, the reflection coefficients will also be identical for the different models.
The reflection coefficients plot valid for all the Jotun models is displayed in figure 6.7.

In this chapter, as for the reflection coefficients plots displayed in chapter 5, both modulus and phase of the reflection coefficients are displayed. This gives better foundation for a more thorough comparison between the coefficients plot, and the top reservoir reflections on the synthetic seismogram.
The reflection coefficients plotted are as mentioned the coefficients representing the top reservoir reflection, more specifically the reflection coefficients from the top of layer 8 (table 6.1).

Correlation   In chapter 5, the problem concerning that the offsets at the seismograms are given in meters, while they for the reflection coefficients plots are given in angle of incidence is brought up. This is still the case, and once again this makes the correlation between them more difficult.
Therefore *NORSAR - 2D ray modelling* is used to calculate the conversion from one unit to the other. The cross plot illustrating these two ways of defining the offsets is displayed in figure E.1 in the Appendix E.
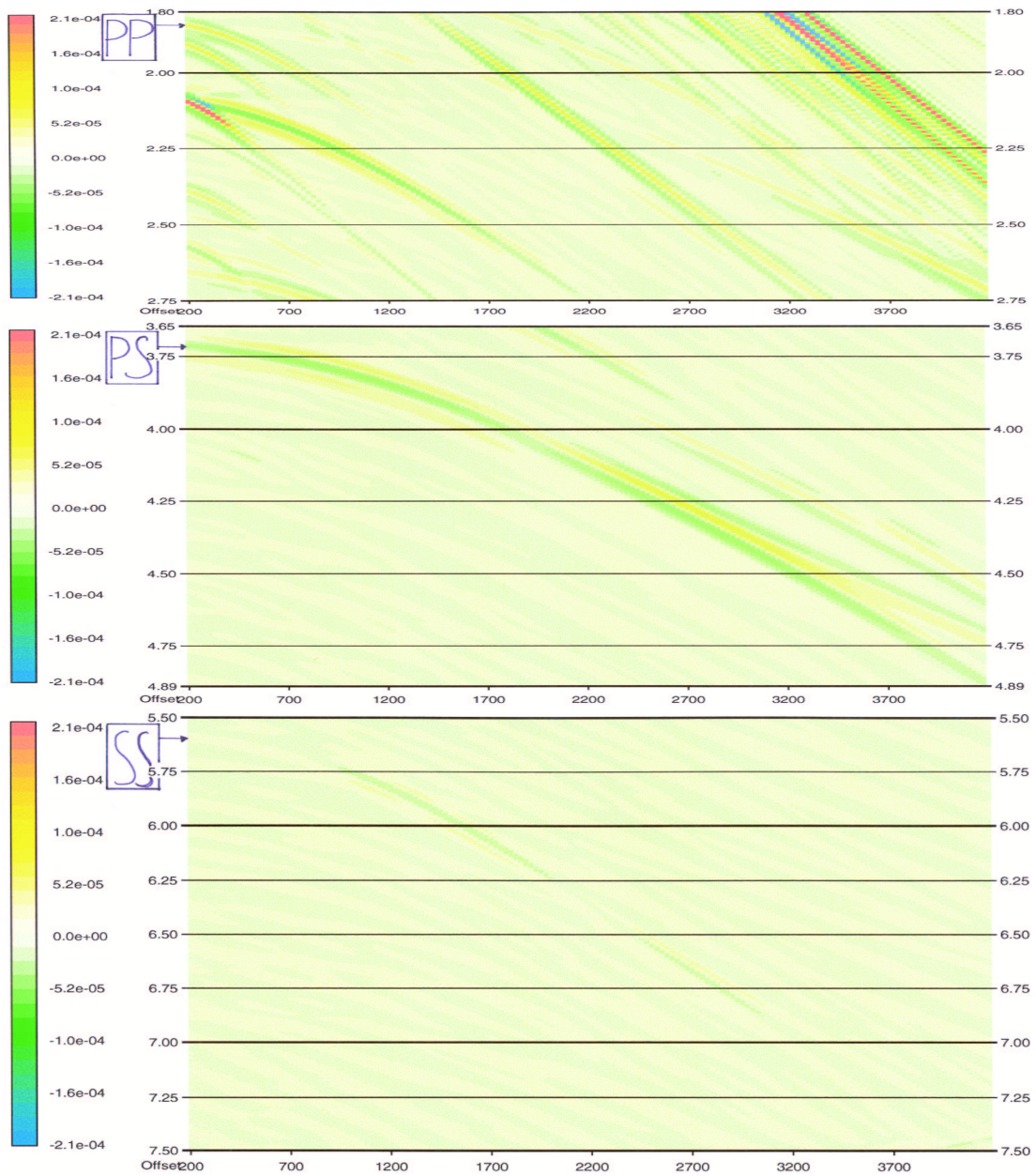
Figure 6.6: *The PP-, PS- and SS-reflections from the top of the reservoir from the synthetic seismogram displaying an altered version of the parameters extracted from well 25/8 − 6T2 in the Jotun field. The attenuation in the layers above the top reservoir reflector represents a 50% saturated overburden.*
The PP-reflection is displayed on top. The PS-reflection in the middle, and the SS-reflection at the bottom.
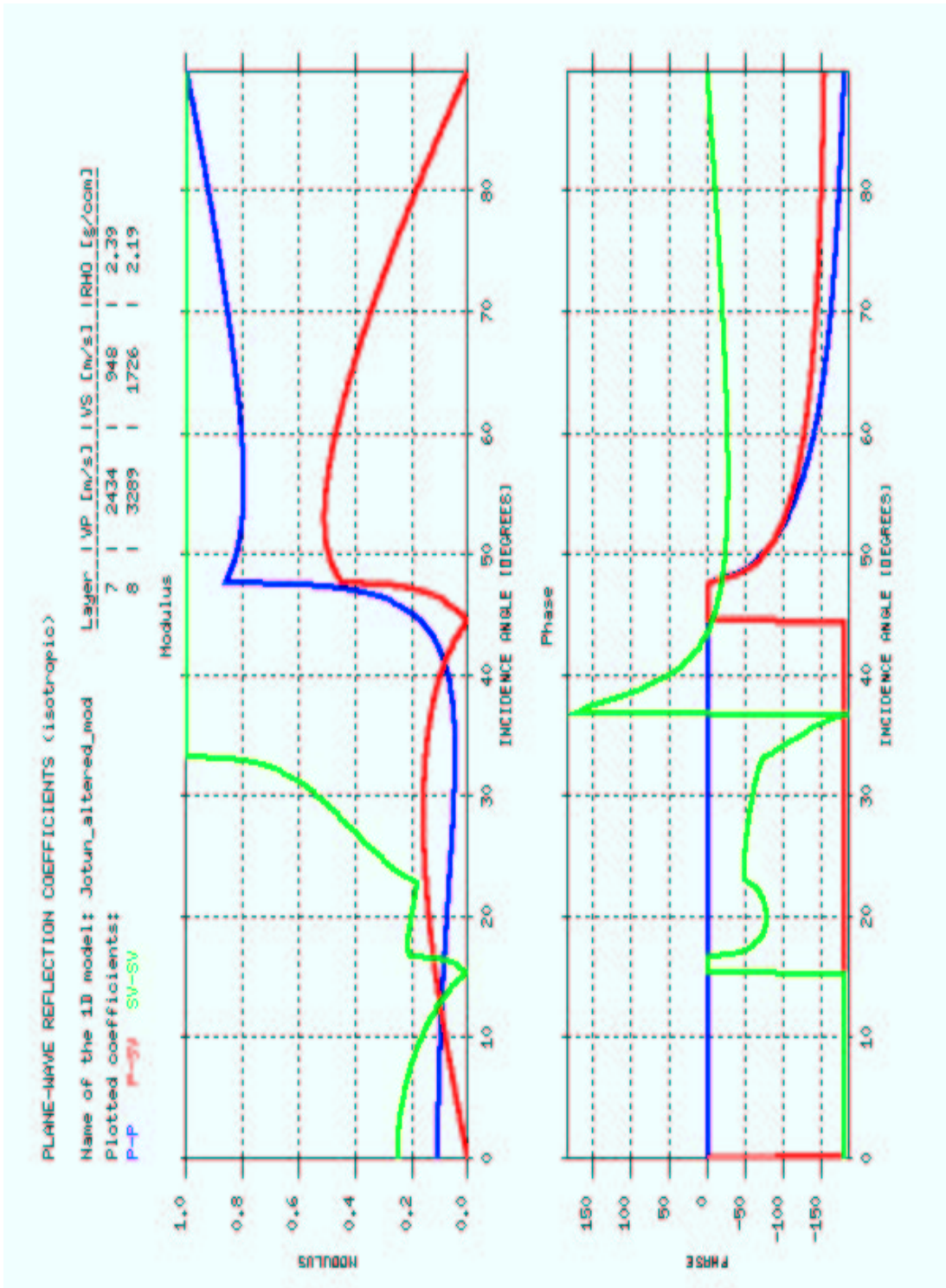
Figure 6.7: *The reflection coefficients, both modulus and phase, for the P-P, P-SV and SV-SV waves propagating through the altered version of a scenario at the Jotun field. Color codes for the different waves are defined on the top of the plot.*

Overburden simulating a 50% saturated gas-cloud

The PP-wave event is barely visible up until an offset of 3.100 m
(44 deg) on the seismogram. This is as expected based on the initial
small value of the reflection coefficient for this wave. After this point
the signal increases in energy, and becomes more visible. This is also
in accordance with the plot of the coefficients.

Due to the weak signal, it is difficult to evaluate the polarity of the
phase for this event.

As for when the models evaluated in the previous chapter, the re-
flection of **the PS-wave** is initially weak on the seismogram. This
corresponds with the fact the reflection coefficient equal zero at zero
offset. Further the amplitude increases, reaches a local maximum at
1.200 m (30 deg), before it once again is reduced to zero at an offset
of 1.900 m (44.5 deg). The phase of the signal has a negative center
peak in the amplitude. This result is displayed in both presentations.
For larger offsets the modulus of the amplitude increases rapidly
again, before it gradually reduces once more. This is also i coher-
ence with what is found when regarding the PS-reflection coefficient.
Further, the amplitude on the seismogram is increased additionally
around the offset of 2.700 m due to interference with the refracted
wave from the reservoir.

The reflection of **the SS-wave** is very weak. Due to the directivity
of the energy, the signal has no energy for near offsets as previously
explained (section 5.3).

The SS-event is not clearly visible at the enlarged seismogram until
an offset of 950 m (17.5 deg) has been reached. This is after the point
of zero offset on the reflection coefficient plot at 15.5 deg, when the
modulus of the amplitude increases rapidly.

From this point the amplitude on the event increases until the maxi-
mum value on the seismogram is obtained at 1.700 m (31 deg). From
here the amplitude gradually lose its energy, except for around 2.200
m ($\sim$ 47.5 deg) where the signal vanishes from the seismogram. This
is most likely caused by interference with a crossing event. This grad-

ual loss of modulus is not in correlation with the behaviour of the reflection coefficient, which is constantly at its maximum from 33 deg (about 2.000 m). This is most likely due to total reflection.

It seems as if the phase is constantly negative for both presentations.

Both the synthetic seismogram and the reflection coefficient plot demonstrate the same variations in the amplitude modulus. The correlation between the two is high.

As for chapter 5, this indicates that the changes in a seismic signals amplitude can not solely be explained by attenuation. Once again the models show that the reflection coefficients highly influence the amount of energy the signal possesses. That the PP-waves gives the best resolution at near offsets, while SS-waves are best for larger offsets can therefore mainly be explained by the values of each waves reflection coefficients.

6.4.2 Comparison of gathers with and without attenuation

Throughout the modelling based on the altered well data performed in this chapter, Q_p and Q_s are the only parameters allowed to vary. The values of Q are chosen to simulate different scenarios where the overburden is partially gas-saturated. This way the effects of attenuation on the seismic signal can more or less be isolated, and therefore easier to investigate.

In this section the results of two other models are displayed.

Figure 6.8 shows the PP-, PS- and the SS-reflections from the top reservoir from the reference model based on the Jotun well data.

Comparing the PP-, PS- and SS-events displayed in this figure with the events displayed in figure 6.6 one can clearly see the difference in magnitude of the signals amplitudes. The reference model, which has an overburden practically free of any attenuating effects, shows that the seismic evens possess far more energy than what is the case for the model containing a 50% saturated gas-cloud in the overburden (figure 6.6).

The phase polarization for the events in these two illustrations seems on the other

Figure 6.8: *The PP-, PS- and SS-reflections from the top of the reservoir from the synthetic seismogram displaying an altered version of the parameters extracted from well $25/8 - 6T2$ in the Jotun field. The attenuation in the layers above the top reservoir reflector is approximately zero. This is used as a reference model. The PP-reflection is displayed on top. The PS-reflection in the middle, and the SS-reflection at the bottom.*

hand to be identical. If there is a variance between them, it is not an effect visible to the naked eye.

All three events shown in figure 6.8, are clearly visible for all offsets. This on the other hand is not the case in figure 6.6, where the events at some areas are barely visible. And since the only parameter that changes between these two models is the Q-factor, one can quite firmly confirm that this massive loss of energy is due to the attenuation caused by the gas-cloud present in the overburden in figure 6.6.

The other model displayed here to support the findings on the effect of attenuation is constructed with the simulation of a 10% saturated gas-cloud in the overburden ($Q_p = 50$ and $Q_s = 110$). The PP-, PS- and the SS-reflections from the top reservoir in this model is shown in figure 6.9.

When comparing the events on this figure to those in figure 6.6, the difference between the two scenarios are not as striking as for the case studied above.
One can still fairly clearly see that the reflections from underneath a 10% saturated gas-cloud (figure 6.9) possess a stronger magnitude of amplitude than those underneath a 50% saturated gas-cloud (figure 6.6). And since there is an established connection from such a loss in amplitude to the amount of attenuation in the overburden, this is an expected result. A 50% saturated gas-cloud gives lower Q-values than a a 10% saturated gas-cloud.
The phase polarity seems to be identical in this case as well.

Regarding figure 6.9 and figure 6.8 illustrates that a 10% saturated gas-cloud present in the overburden also result in a massive loss of energy compared to the ideal scenario where there would be no detectable attenuation.

The examination of these two additional models emphasize the validity found in the results presented in the previous chapter.
As a direct consequence of the attenuation caused by gas-clouds in the overburden, the seismic signal undergoes a massive loss of energy. The magnitude of the amplitude is therefore strongly reduced. However, it seems as if the signals phase stays more or less unaffected by the attenuation. It is at least not visible without further examination.
And once again it is also demonstrated that it is possible to make a distinction between different degrees of saturation in the gas-clouds.
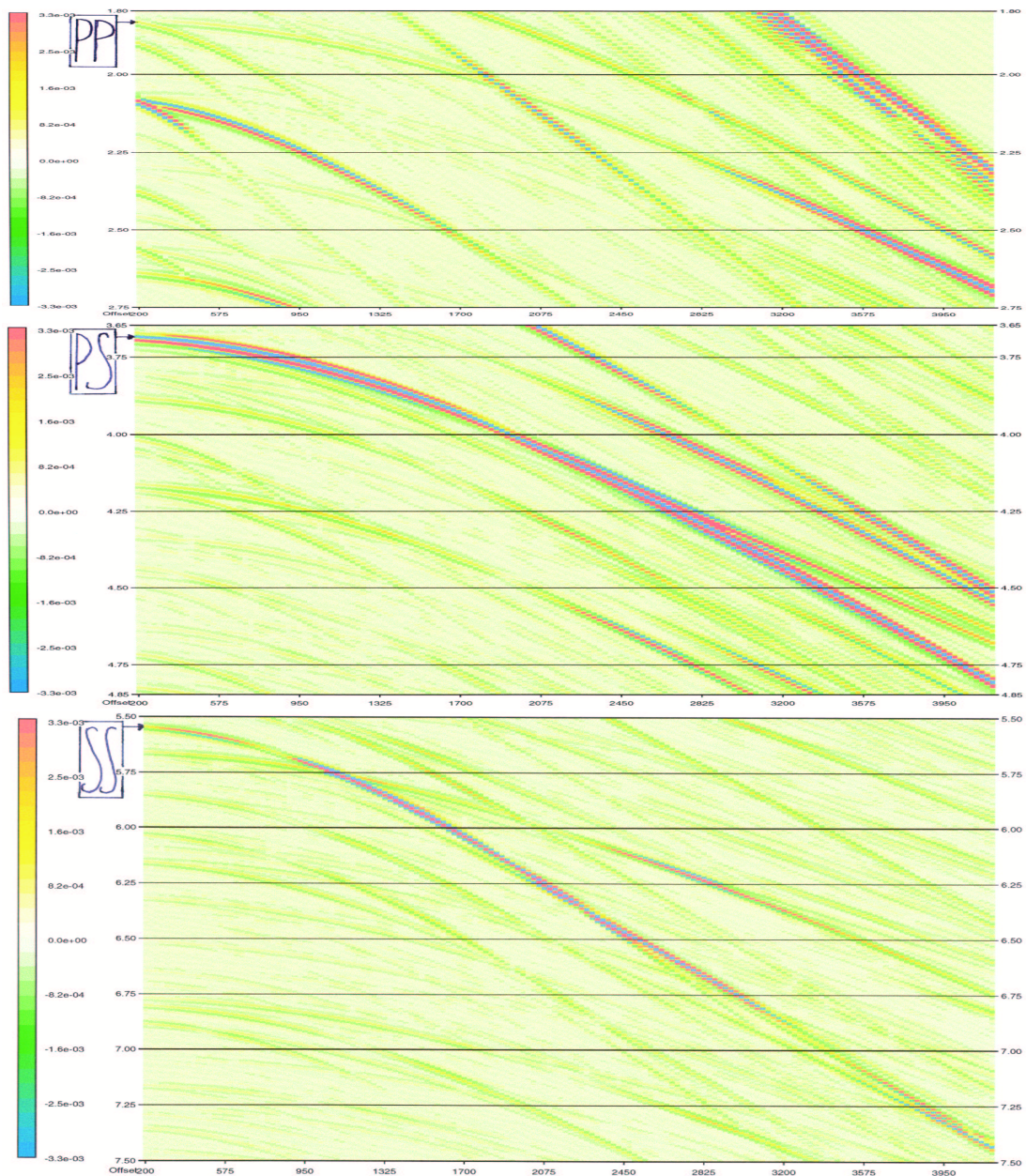
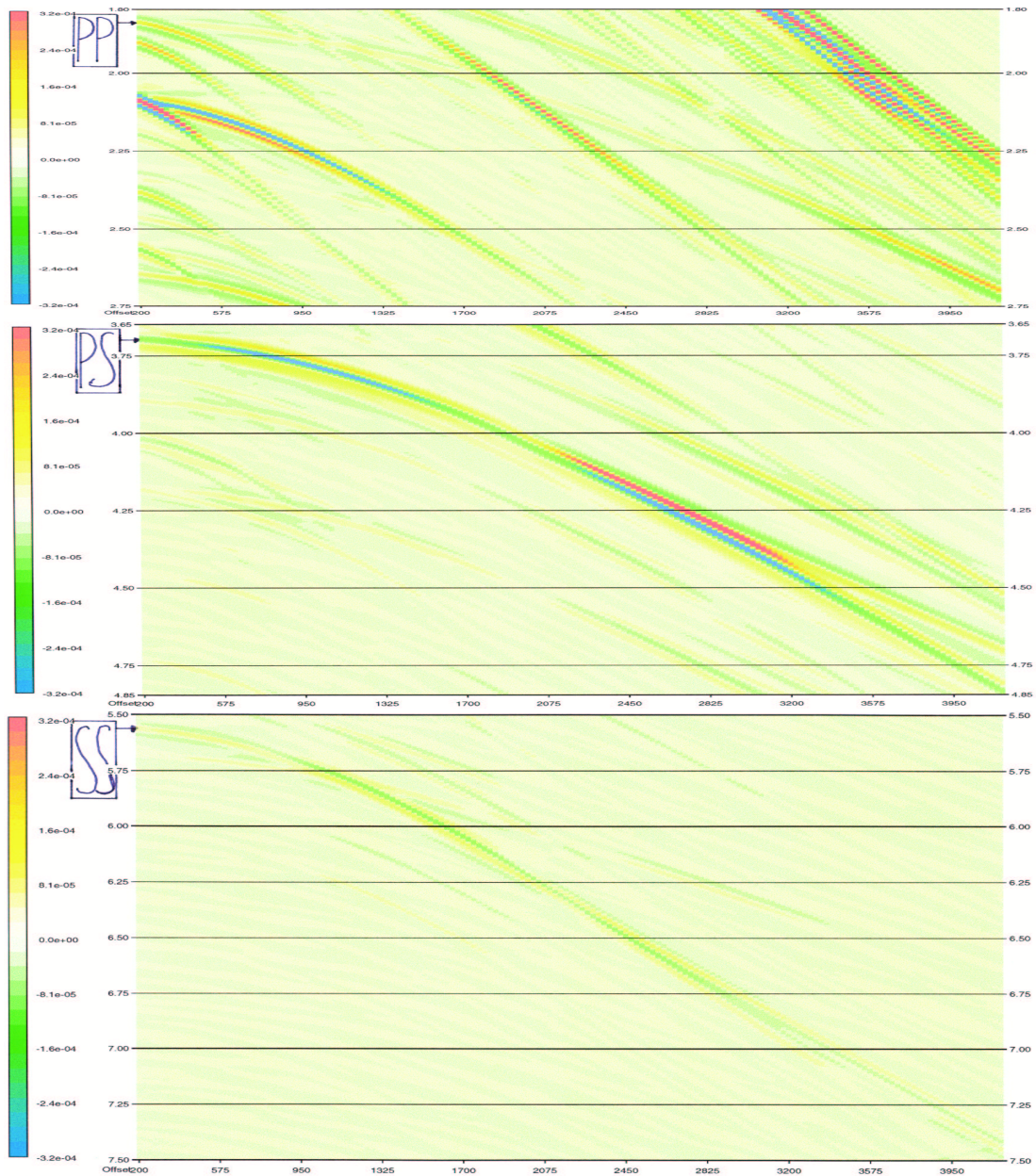Figure 6.9: *The PP-, PS- and SS-reflections from the top of the reservoir from the synthetic seismogram displaying an altered version of the parameters extracted from well 25/8 − 6T2 in the Jotun field. The attenuation in the layers above the top reservoir reflector represents a 10% saturated overburden.*
The PP-reflection is displayed on top. The PS-reflection in the middle, and the SS-reflection at the bottom.

6.4.3   The effect of the presence of a gas-cloud.

To illustrate the isolated attenuating effect of the presence of a gas-cloud, the best way is to compare models where only the values of Q_p and Q_s varies. And this is the case for the modelling performed in this chapter.

Through the correlation between the synthetic seismogram and the plot of the reflection coefficients done in section 6.4, one is able to identify the changes of the signal caused merely by the effects of AVO etc. This is considered a method to eliminate deceptive alteration of the signal, not caused by attenuation.
And as an other result of this correlation, it is found that what initially seemed as a clear demonstration of the effect attenuation had on seismic resolution power may not mainly be caused by attenuation after all. It seems as if the reflection coefficients control these tendencies to a much larger degree.

The presence of a gas-cloud in the overburden causes the Q-values to drop considerably, meaning that there will be an increased attenuation of the signal. Through the models illustrated in this chapter the effects of such a phenomenon is clearly demonstrated.
A massive loss of energy leading to a reduction of the amplitude magnitude is proven. The results obtained here also suggest that it is possible to even distinguish between different degrees of saturation.
On the other hand, the presence of a gas-cloud does not indicate any phase rotation in the signal.

6.5   Fictitious vs. real data

The models generated and presented in this chapter are based on well data from the Jotun field. The results obtained here will therefore be considered to be *real* data.
The models generated and presented in chapter 4 and 5 on the other hand are based on earth models constructed by fabricated rock parameters. These models will therefore represent fictitious data.

The object of making models based on real well data is to verify the justness of the results obtained when modelling with fictitious data. The results concerning

the effect of attenuation on the seismic signal is of main interest.

The modelling done in this, and the previous chapter (chapter 5) uses the same initial setup with a very simple earth model containing a partially saturated gas-cloud in the overburden. Due to the great resemblance between these models they can easily be compared.

The tendencies these models show are the same for both real and fictitious data. When a seismic wave travels through a medium with high attenuation, here represented by an overburden containing a gas-cloud, its signal will be affected and altered. And throughout this study, all the models explored, real and fictitious, give the same result. Namely that the attenuation due to a gas-cloud causes the seismic wave to undergo a massive loss of energy. The amplitudes are reduced significantly, making the reflections from underlying boundaries weaker and therefore not as visible. The signals phase on the other hand does not seem to suffer from any major changes.

If regarding the findings from the initial modelling performed in chapter 4 too, the same trends are revealed there as well.
The signals amplitude is drastically reduced in these basic models as well. The phase is also found not to undergo major distortions. Some changes are however detected, but these are so small that they cannot visibly be detected.

It is found the both fictitious and real data gives the same results, and can therefore be said coincide very well.
This substantiate the validity of the findings made in these studies.

6.6   Chapter summary

In this final modelling chapter, the effects of attenuation is explored in synthetic seismograms generated on the basis of rock parameters extracted from well $25/8-6T2$ on the Jotun field.
The construction of the earth models made here is similar to that of those made in the previous chapter. An overburden containing a gas-cloud overlying a reservoir zone are the main features for these models. The goal is therefore to evaluate the effect the attenuation, as a direct consequence of the presence of gas, will add to the seismic waves signal as it propagates through the overburden.

The results obtained indicate that seismic waves undergo a massive loss of energy, and therefore reduction of amplitude, when traveling through a gas-cloud. The attenuating effects due to the presence of gas in the overburden is thus proven to clearly be of great influence on the magnitude of a signals amplitude.

But even though the loss of energy caused by this phenomenon is so large, attenuation does not seem to have any significant influence on the signals phase. No evident phase rotation can be detected on these seismograms.

As demonstrated in section 6.5, these findings clearly coincide with what is found in the previous chapters. It is therefore reasonable to believe that these results reflect the real world.

The resolution powers of the different wave types has also been investigated through these models. The correlation between the synthetic seismogram and the reflection coefficients plot is used to explore this topic.

It is found that these two illustrations show the same changes, meaning that the changes in the signal displayed on the seismogram can highly be explained by the values of the reflection coefficients for the waves. This indicates that the fact that PP-waves possess the most energy at near offsets, while SS-waves have the most energy at far offsets cannot merely be explained through the effects of attenuation. The energy level for the different kinds of waves is highly dependent on the values of the reflection coefficients. It is therefore hard, from this study to make a firm conclusion concerning how the effects of attenuation affect the resolution powers of the seismic waves.

Chapter 7

Remarks and conclusions

The object of this thesis is to explore the effect of seismic wave attenuation, given by the Q-factor, in fluid saturated rocks. This is a phenomenon that is difficult to interpret, mainly due to the complexity of the physical processes involved. The models explored in this study is therefore kept rather simple. This way the number of parameters varying is limited, and chances of possible misconceptions are reduced.

In chapter 4, the initial conceptual modelling is performed. The results from these models indicate that a seismic signals amplitude is considerably reduced as a result of attenuation. The models show that the signals are very sensitive to the degree of attenuation present in a medium. The higher the degree (the lower value of Q), the more will the amplitude decrease in magnitude. This is as expected. Further, it is found that the reduction in amplitude between two wavelets propagating through highly attenuating medium (e.g. $Q = 50$ and $Q = 30$) is larger than for wavelets traveling through a medium with a lower degree of attenuation (e.g. $Q = 200$ and $Q = 150$). This shows that attenuation can be described as an exponential function. As for distortions in the seismic signals phase, no noteworthy changes is found. The little alterations that might occur will be insignificant when it comes to interpret seismograms.

The modelling performed in chapter 5 can be considered as a prolongation of the previous work. To make the models more realistic, real parameter values for different saturation conditions are used. A partially saturated gas-cloud in the overburden is the basis for these models. The main effect of the attenuation

caused by the gas-cloud is a massive loss in the magnitude of the seismic signals amplitude. It is also found that it is even possible to distinguish between different degrees of saturation. No evident distortion of the signals phase can be detected in the models explored in this chapter either. The results obtained in this chapter is in accordance with the tendencies outlined in chapter 4. Focus is also put on trying to draw conclusions about attenuating effect on the resolution powers of the different waves. But no clear connection between the two is found. However, it is found a strong correlation between the waves variations in amplitude, and thus energy level, and their reflection coefficients. So what was initially thought to be evident attenuation effects turned out to be a direct result of AVO effects etc. No clear conclusions concerning resolution powers can therefore be made based on these models.

To make an evaluation whether or not the conclusions drawn based on the modelling in chapter 4 and 5 coincide with real data, chapter 6 is dedicated to more realistic modelling. These models are based on parameters obtained from well $25/8 - 6T2$ on the Jotun field.

The similarity between the results obtained from *fictitious* and *real* modelling is striking. This supports previous modelling. The exact same conclusions are made; attenuation causes a massive decrease in the amplitudes magnitude, while there is no evident phase distortion. And for the evaluation of resolution powers, this modelling could not prevail more answers than before. No conclusions can be made.

As a whole, the results obtained from the work done in this thesis give an increased understanding of the effect of attenuation. It seems as the reduction of a seismic signals amplitude potentially can provide information about the fluid saturation in rocks. The signals phase on the other hand, appears to be of limited use. Very small changes has been proven, and considering the increased complexity of the seismogram when treating real data makes it more or less impossible to detect such distortions.

A recommendation for further work is as follows ;

- more profound examination of the attenuating effects on P- vs. S-waves,

- establishing a connection between the degree of reduction in amplitude and the saturation conditions,

- further investigation of the effect attenuation has on the resolution powers of seismic waves.

Bibliography

ARMSTRONG, B. H. (1980). Frequency-independent background internal friction in heterogeneous solids. *Geophysics*, **45**(6), 1042–1054.

BERKHOUT, A. J. (1984). Seismic Resolution. *Geophysical Press.*

BERRYMAN, J. G. (1980). Long-wavelength propagation in composite elastic media I. Spherical inclusions.. *J. Acoust. Soc. Am.*, **68**(6), 1809–1819.

BIOT, M. A. (1956a). Theory of propagation of elastic waves in a fluid saturated, porous solid. I. Low-frequency range.. *J. Acoust. Soc. Am.*, **28**, 168–178.

BIOT, M. A. (1956b). Theory of propagation of elastic waves in a fluid saturated, porous solid. II. Higher-frequency range.. *J. Acoust. Soc. Am.*, **28**, 179–191.

BORN, W. T. (1941). The attenuation constant of the earth materials. *Geophysics*, **6**, 132–148.

BOUCHON, M. AND AKI, K. (1977). Discrete wavenumber representation of seismic source wave field. *Bull. Seism. Soc. Am*, **67**, 259–277.

CLARK, R. A., CARTER, A. J., NEVILL, P. C., AND BENSON, P. M. (2001). Attenuation measurements from surface seismic data - Azimuthal variation and time-lapse case studies. .

DAVIS, G. H. AND REYNOLDS, S. J. (1996). *Structural geology of rocks and regions* (2 edition). John Wiley and Sons, Inc.

DEFFENBAUGH, M., SHATILO, A., SCHNEIDER, B., AND ZHANG, M. (2000). Resolution of Converted Waves in Attenuating Media. In *70th Annual Internasjonal Meeting*, pp. 1178–1180.

DROTTNING, A., RUUD, B. O., BAKKE, R., AND JOHANSEN, T. A. (2002).
Jotun field study: Presentation of data and preliminary results. Tech.
rep. SRC Report No. 01-005, Institute of Solid Earth Physics, University
of Bergen.

DUTTA, N. C. AND OD, H. (1979a). Attenuation and dispersion of compressional waves in fluid-filled porous rocks with partial gas saturation (White model) - Part I: Biot theory.. *Geophysics*, **44**(11), 1777–1788.

DUTTA, N. C. AND OD, H. (1979b). Attenuation and dispersion of compressional waves in fluid-filled porous rocks with partial gas saturation (White model) - Part II: Results.. *Geophysics*, **44**(11), 1789–1805.

FOWLER, C. M. R. (1998). *The Solid Earth; An introduction to Global Geophysics*. Cambridge University Press.

GASSMANN, F. (1951a). Elastic waves trough a packing of spheres. *Geophysics*, **16**, 673–685.

GASSMANN, F. (1951b). Uber die Elastizat Poroser Medien. *Vierteliahrsschrift der Naturforschenden Gesellschaft in Zurich*, **96**, 1–23.

HEGGERNES, R. (1988). Absorpsjonsmekanismer og relativ dempning av p- og s-blger i vske- og gass-fylte porse media. Master's thesis, Institutt for den faste jords fysikk, Universitetet i Bergen.

JACKSON, D. D. AND ANDERSON, D. L. (1970). Physical Mechanisms of Seismic-Wave Attemuation. *Reveiws of Geophysics and Space Physics*, **8**(1), 1–63.

JOHANSEN, T. A. (1997). Seminarserie: Bergartsfysikk. .

JOHANSEN, T. A., DROTTNING, A., LECOMTE, I., AND GJOEYSTDAL, H. (2002). An approach to combined rock physics and seismic modelling of fluid substitution. *Geophysical Prospecting*, **50**(2), 119–137.

JOHNSON, D. L. AND PLONA, T. J. (1982). Acoustic slow waves and the consolidation transition. *J. Acoust. Soc. Am.*, **72**(2), 556–565.

JOHNSTON, D. H., KOPLIK, J., AND DASHEN, R. (1987). Theory of dynamicpermeability and tortuosity in fluid-saturated porous media. *J. Fluid. Mech.*, (176), 379–402.

JOHNSTON, D. H., KOPLIK, J., AND SCHWARTZ, L. M. (1986). New Pore-Size Parameter Characterizing Transport in Porous Media. *Phys. Rev. Lett.*, **57**(20), 2564–2567.

JOHNSTON, D. H., TOKSK, M. N., AND TIMUR, A. (1979). Attenuation of seismic waves in dry and saturated rocks: II. Mechanisms. *Geophysics*, **44**(4), 691–711.

JOHNSTON, D. H. AND TOKSZ, M. N. (1981). Definitions and Terminology. In Johnston, D. H. and Toksz, M. N. (Eds.), *Seismic Wave Attenuation*, No. 2, pp. 1–5. Geophysics reprints series.

JONES, T. D. (1992). Pore fluids and frequency-dependent wave propagation in rocks. In Nur, A. M. og Wang, Z. (Ed.), *Seismic and Acoustic Velocities in Reservoir Rocks*, No. 10, pp. 349–363. Geophysical reprints series.

KANESTRØM, R. (1982). Seismologi. Jordskjelvstasjonen, Universitetet i Bergen.

KELDER, O. AND SMEULDERS, D. M. J. (1997). Observation of the Biot slow wave in water-saturated Nivelsteiner sandstone. *geophysics*, (62), 1794–1796.

KENNETT, B. L. N. (1983). *Seismic wave propagation in stratified media*. Cambridge University Press.

KJARTANSSON, E. (1979a). *Attenuation of seismic waves in rocks and applications in energy exploration*. Ph.D. thesis, Standford University.

KJARTANSSON, E. (1979b). Constant Q - Wave Propagation and Attenuation. *Journal of Geopysical Research*, **84**(B9), 4737–4748.

KLIMENTOS, T. AND MCCANN, C. (1988). Why is the biot slow compressional wavw not observed in real rocks?. *Geophysics*, **53**, 50–73.

KLIMENTOS, T. AND MCCANN, C. (1990). Relationships among compressional wavw attenuation. porosity, cly content, and permeability in sandstones. *Geophysics*, **55**(8), 998–1014.

KOESOEMADINATA, A. P. AND MCMECHAN, G. A. (2001). Sensitivity of viscoelastic reflection amplitude variation with angle to petrophysical properties. *Journal of Seismic Exploration*, (9), 269–284.

KUSTER, G. T. AND TOKSZ, M. N. (1974). Velocity and attenuation of seismic waves in two-phase media: Part I: Theoretical formulations. *Geophysics*, **39**(5), 587–606.

LAY, T. AND WALLACE, T. (1995). *Modern global seismology*. Academic press.

LIU, H. P., ANDERSON, D. L., AND KANAMORI, H. (1976). Velocity dispersion due to anelasticity: Implications for seismology and mantle composition. *Geophys. J. Royal Astronom. Soc.*, **47**, 41–58.

LOKSHTANOV, D. (1993). Seismic modelling with transverse isotropy and attenuation. Norsk Hydro Report; R-065961, Norsk Hydro.

MAVKO, G., MUKERJI, T., AND DVORKIN, J. (1998). *The Rock Physics Handbook: Tools for seismic analysis in porous media*. Cambridge University Press.

MAVKO, G. M. AND NUR, A. (1979). Wave attenuation in partially saturated rocks. *Geophysics*, **44**, 161–178.

O'CONNELL, R. J. AND BUDIANSKY, B. (1977). Viscoelastic Properties of Fluid-Saturated Cracked Solids. *Journal of Geophysical Research*, **82**(36), 5719–5736.

PGS Seres (2001). *Nucleus User Manual*.

PRANDIT, B. I. AND SAVAGE, J. C. (1973). An experimental test of Lomnitz's theory of internal friction in rocks. *J. Geophysical. Res*, **78**, 6097–6099.

SHEARER, P. M. (1999). *Introduction to seismology*. Cambridge university press.

SHERIFF, R. E. (1980). Nomogram for Fresnel zone calculation. *Geophysics*, **45**(5), 968–972.

SHERIFF, R. E. (1999). *Encyclopedic Dictionary ofExploration Geophysics* (3 edition). Society of Exploration Geophysicists.

SUNDVOR, E. (1989). Tolkning av marinseismiske data. Del 1: Refleksjonsseismikk. Jordskjelvstasjonen. Universitetet i Bergen.

TATHAM, R. H. (1982). Vp/Vs and lithology. *Geophysics*, **47**(3), 336–344.

TORGERSEN, E. (1999). Integrert geologisk og seismologisk modellering. .

UDAS, A. (1999). *Principles of Seismology*. Cambridge University Press.

WALSH, J. (1966). Seismic Wave Attenuation in Rock Due to Friction. *Journal of Geophysical Research*, **71**(10), 2591–2599.

WATERS, K. (1981). *Reflection seismology*.

WHITE, J. E. (1975). Computed seismic speeds and attenuation in rocks with partial gas saturation. *Geophysics*, **40**(2), 224–232.

WHITE, J. E. (1983). *Underground sound - Application of Seismic Waves*. Methods in geochemistry and geophysics. Elsevier Sience Publishers B.V.

WIDMAIER, M. (1999). *Vertical resolution of PS-convertend waves*. PGS Seres AS. Report for PGS Reservoir.

WINKLER, K. AND NUR, A. (1982). Seismic attenuation: Effects of pore fluids and frictional sliding. *Geophysics*, **47**, 1–15.

ZENER, C. (1938). Internal Friction in Solids: 2. General Theory of Thermoelastic Internal Friction. *Physical Review*, 90–99.

Appendix A

Biot's theory

Gassmann published in 1951 his theory on how to calculate the effect of the properties of a pore fluid on the elastic characteristics and the seismic velocities of a porous, fluid saturated rock (Gassmann, 1951b, 1951a). The solid material is assumed to be isotropic, and all pores are assumed to be connected. This theory is static and applies to low frequency waves. For the equations Gassmann used, the P- and S-velocities are given by;

$$V_p = \left(\frac{K_b + 4G/3 + n^2 M}{\rho_{sat}} \right)^{1/2} \tag{A.1}$$

and

$$V_s = \left(\frac{G}{\rho_{sat}} \right)^{1/2}, \tag{A.2}$$

where K_b and G denotes the bulk density and the shear modulus of the dry porous rock, respectively. The density of the saturated rock is $\rho_{sat} = \phi \rho_f + (1 - \phi) \rho_s$, where ϕ denotes the porosity, ρ_f the density of the fluid saturating the porous rock and ρ_s the density of the solid matrix material. And by using $n = (1 - K_b/K_s)$, M will be given by the equation:

$$M = \frac{1}{[\phi/K_f + (1 - \phi)/K_s - K_b/K_s^2]}, \tag{A.3}$$

where K_f denotes the bulk modulus of the saturating fluid, and K_s the bulk

133

modulus of the solid rock matrix material.

The model Gassmann used was meant for static or low frequency pressure variations, meaning that if the frequency would increase, these calculations would not be valid. Biot (1956a, 1956b) considered Gassmann' s theory, and found that for higher frequencies, such as ultrasonic frequencies used in laboratorial experiments, two of the assumptions Gassmann made for his model would be violated. The pore fluid would no longer be frictionless (no longer a low-viscosity fluid), and the relative motion between fluid and solid during the passage of an elastic wave could not be neglected. Due to this, Biot made the necessary adjustments of the theory so that it would be possible to apply for higher frequencies as well. The result of this revision was 5 assumptions used on the Biot (1956a, 1956b) model. These assumptions are as follows:

1. The grains and the pore fluid are both individually homogeneous and isotropic.

2. The grains are interconnected.

3. The pores are open and interconnected (no isolated pores).

4. The pore fluid is evenly distributed in the pores (fully saturated by one kind of pore fluid).

5. The pores and grains are a lot smaller than the wavelength of the seismic waves deforming the rock.

But also Biot's theory has an upper bound for the frequency, when the wavelength becomes of the order of the pore size.

Biot modelled the elastic response possible to obtain when a solid was exposed to tension variations from both low and high frequencies. The main difference between these two cases is that when high frequency waves passes through a fluid saturated rock, friction occurs between the fluid and the solid rock. The effects of such friction depends on both the characteristics of the pore fluid and of certain geometrical features of the pore itself.

To combine the low- and high- frequency response, Johnston et al. (1987) introduced some additional rock parameters to Biot's model. The new parameters are dynamic, i.e. dependent on frequency.

In the following Johnston et al. (1987)'s three parameters will be further presented. The list of all general parameters used in Biot's model is presented in

table A.1.

Properties of a dry rock		
PARAMETER	SYMBOL	UNITS
Bulk modulus - mineral	K_s	GPa
Bulk modulus - solid	K_b	GPa
Shear modulus - solid	μ	GPa
Density - mineral	ρ_s	g/cm^3
Porosity	ϕ	$(0 \leq \phi \leq 1)$
Infinite tortuosity[1]	α_∞	$(\alpha_\infty \geq 1)$
Dynamically cemented porosity[1]	Λ	μm
Static permeability[1]	k_0	$D\,(D = 10^{-12}\,m^2)$

Properties of pore fluid		
PARAMETER	SYMBOL	UNITS
Bulk modulus	K_f	GPa
Density	ρ_f	g/cm^3
Viscosity[1]	η	$cP\,(cP = 10^{-3}\,Pa\,s)$

[1] only relevant for high frequencies

Table A.1: *The parameters used in Biot's model (Johansen, 1997).*

Infinite tortuosity, α_∞. This parameter gives the coupling between the fluid and the solid. Geometrically the infinite tortuosity is a measure of the sinuosity, or the curve, of the pores. One definition of α_∞ in a solid filled with pores of constant radius, is given by the equation (Klimentos & McCann, 1988);

$$\alpha_\infty = \left(\frac{L_e}{L}\right)^2, \tag{A.4}$$

where L_e is the actual length of the pore (measured along the pore) in a porous medium of length L.
Berryman (1980) has given another definition of this parameter;

$$\alpha_\infty = 1 - r\left(1 - \phi^{-1}\right), \tag{A.5}$$

where r is a factor that needs to be evaluated in the context of the geometrical properties of the solid. Biot's theory implies the existence of two P-waves in a fluid saturated rock; the *fast* and the *slow* P-wave. The definition and physical aspects of these waves will be explained later.

Klimentos & McCann (1988) showed that this parameter could be defined by the slow P-wave and the P-wave in the pore fluid. Their definition is as follows;

$$\alpha_\infty = \left(\frac{V_{p,\,fluid}}{V_{p-slow}} \right)^2.$$ (A.6)

Dynamically cemented porosity, Λ. The dynamically cemented porosity express the ratio between the volume of the pore, and the total area of the pore, where each element of the volume is weighted with its local value of potential microscopic fluid flow velocity (figure A.1). This function of weighting provides a certainty of that non-permeable pores (isolated pores) will have no influence on Λ. This parameter is consequently closely related to the potential of fluid transport the rock processes.
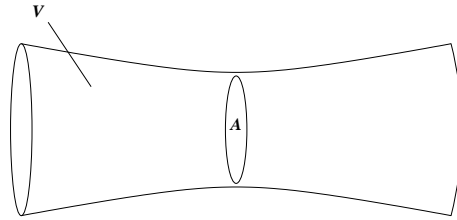

Figure A.1: Λ is defined as the ratio between the volume of the pore, V, and the total area of the pores. Each element of volume is weighted with its local value of potential microscopic fluid flow velocity.

Johnston et al. (1986) gives the following ratio between Λ, the porosity ϕ, and the diameter d;

$$\Lambda = \frac{2\phi d}{9\,(1-\phi)}.$$ (A.7)

This ratio is valid if the material is a so-called *suspension*, which means that the porosity is so high that the material has no shear modulus; $\mu = 0$. The dynamically cemented porosity can also be determined experimentally, by measuring the attenuation of high frequency P-waves. The quality factor, Q, is in this case related to Λ by;

$$\frac{1}{Q} = \frac{\delta}{\Lambda},$$

giving

$$\Lambda = \delta Q_\infty,$$

where δ is the *viscous skin depth* (which will be described below).

Static permeability, k_0. The last parameter Johnston introduced gives the capacity of fluid flow that the medium possesses. The *static permeability* is a connecting parameter between the fluid and the rock.

If a porous material is filled with a fluid, of viscosity η, and a constant pressure gradient, ΔP, is induced on the sample, there will be generated a fluid flow through it. The average fluid flow is expressed by ϕv, where v is the average flow velocity. ϕv is in this case given by the equation:

$$\phi v = - \left(\frac{k_0}{\eta} \right) \Delta P. \tag{A.8}$$

The three new frequency dependent parameters can all be related by what is called *the medium factor*. Johnston et al. (1986) define the medium factor, M, which through experimental research seems to be linked to Λ, k_0 and *the factor of formation*, F. They are all connected by

$$M = \frac{8Fk_0}{\Lambda^2}. \tag{A.9}$$

And by using equation A.5, this ratio can be converted to

$$M = \frac{8\alpha_\infty k_0}{\phi\Lambda^2}. \tag{A.10}$$

In the case of low frequency waves the fluid flow in the pores will be of the *Poiseuille* type. This means that the particles in the fluid moves parallel with the walls of the pore, but the greatest movement will occur in the center of the pore. This is due to the fact that the particles near the walls have a stronger viscous connection to the grains of the rock, and that is why they can not move as freely as the once in the center. Or in other words: the friction diminishes towards the center of the pore.

At higher frequencies a potential fluid flow will arise. This means that the movement of the fluid is a combination of compression and flow. A turbulent flow develops. The viscous forces between the fluid and the pore wall are in this case weaker than for Poiseuille flow. But the internal forces within the fluid gives it a more irregular 'flowing pattern'. The curl of the particles increases, and the

average fluid flow is no longer proportional to the *volume flow*, which as with Poiseuille flow.

In the case of Poiseuille flow, the attenuation of the seismic energy is dominated by the viscous drag, the friction, found between the grains and the fluid particles. Winkler & Nur (1982) explains the theory of wave propagation in fluid-saturated media as follows:

> In brief, when the rock frame is accelerated by an acoustic wave, shear stresses are generated within the pore fluid. These stresses decay exponentially away from the pore wall with a viscous skin depth that decreases with increasing frequency. At low frequencies the skin depth is much larger than the pore diameter, shear stresses are small, and viscous energy dissipation is minimal. At high frequencies the skin depth is very small, creating large shear stresses in a very small volume near the pore wall. Again, energy dissipation is small. However, at intermediate frequencies where the viscous skin depth is comparable to the pore size, moderate shear stresses exist throughout the pore volume and maximum energy dissipation occurs.

What kind of fluid flow that will be generated depends on the viscous skin depth, δ, and the width of the pore. The viscous skin depth is defined by (Johansen, 1997);

$$\delta = \left(\frac{2\eta}{\rho_f \omega} \right)^{\frac{1}{2}}, \tag{A.11}$$

where η is the vicsousity, ρ_f the density of the fluid and ω the frequency. When the viscous skin depth is greater or equal to half the pore width, $\delta \geq r$, the fluid flow will behave as a Poiseuille flow (figure A.2).

If a pore is shaped as a cylinder, half the width equals the radii of this cylinder. The total fluid flow will in this case be Poiseuille flow within the viscous skin depth, and potential flow on the outside.

Whether the frequency is defined as low or high depends on if the implied skin depth is small or large in regards to half the pore width. A critical frequency, ω_c, which makes it possible to distinguish between these two possibilities, is
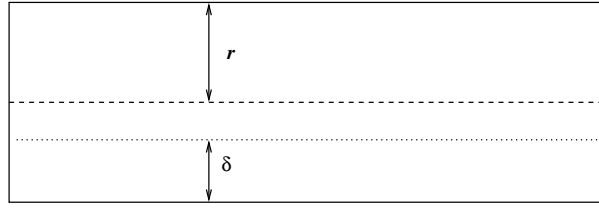
Figure A.2: *Poiseuille flow will occur when the viscous skin depth δ is greater or equal to half the pore width, r.*

introduced by Johansen (1997);

$$\omega_c = \frac{2\eta\phi}{\alpha_\infty k_0 \rho_f}. \tag{A.12}$$

In Biot's original model this issue is treated as two totally separate cases; one has either low- or high frequencies. But when Johnston et al. (1987) introduced the three frequency dependent parameters, it was possible to introduce a transitional zone between high- and low frequencies.

The attenuation of the waves is in some cases found dependent on the frequencies (the discussion about frequency dependency will be attended later). According to Johnston et al. (1979) the attenuation coefficient for the P-wave varies as the square of the frequency, $Q^{-1} \propto f$, when Poiseuille flow is valid. For higher frequencies Biot derived a correction factor to the fluid viscosity and found that α is proportional to $f^{-1/2}$; $Q^{-1} \propto f^{-1/2}$.

Biot's theory predicts the existence of three different volume waves; two kinds of compressional waves, and one shear wave. The two P-waves are referred to as *the fast P-wave* and *the slow P-wave*. Their velocities are given as follows (Johansen, 1997):

$$V_{P-slow} = \left(\frac{\Delta - [\Delta^2 - 4 \left(\rho_{11}\rho_{22} - \rho_{12}^2 \right) \left(PR - Q^2 \right)]^{\frac{1}{2}}}{2 \left(\rho_{11}\rho_{22} - \rho_{12} \right)} \right)^{\frac{1}{2}}, \tag{A.13}$$

$$V_{P-fast} = \left(\frac{\Delta + [\Delta^2 - 4 \left(\rho_{11}\rho_{22} - \rho_{12}^2 \right) \left(PR - Q^2 \right)]^{\frac{1}{2}}}{2 \left(\rho_{11}\rho_{22} - \rho_{12} \right)} \right)^{\frac{1}{2}}, \tag{A.14}$$

where Δ is a real constant, ρ_{11} and ρ_{22} are mass coefficients, and ρ_{12} is the mass

connecting coefficient. P, R and Q are often referred to as Biot's coefficients.
The mass coefficients are both complex and frequency dependent, and they are
often referred to as *Biot's dynamic coefficients*. They describe the effects of a
local increase/reduction of mass in a volume as it compresses or stretches by the
deformations caused by the wave. ρ_{12} is especially defined as a mass coupling
factor, and it expresses the mutual attraction between the grains and the pore
fluid. It is dependent on the degree of the fluids ability to flow in the rock, i.e ρ_{12}
is a function of the dynamic tortuosity. It is given by (Johnson & Plona, 1982):

$$\rho_{12} = (1 - \widetilde{\alpha}(\omega)) \phi \rho_f,,$$

where the dynamic tortuosity is given by (Johansen, 1997):

$$\widetilde{\alpha}(\omega) = \alpha_\infty + i\frac{\eta\phi}{k_0\omega\rho_f}F(\omega) = \alpha_\infty + i\frac{\eta\phi}{k_0\omega\rho_f}\left(1 - i\frac{4\alpha_\infty^2 k_0^2\omega\rho_f}{\eta\Lambda^2\phi^2}\right)^{\frac{1}{2}}.$$

The other two mass coefficients are defined as (Johansen, 1997):

$$(1 - \rho)\rho_s = \rho_{11} + \rho_{12}\phi\rho_f = \rho_{12} + \rho_{22}.$$

The fast P-wave represents the case of the porous matrix and the pore fluid
being compressed simultaneously. It travels mainly within the solid, and it is
being slowed down by (modified) by the pore fluid. The slow P-wave, on the
other hand, travels mainly within the pore fluid, and it is rapidly being slowed
down by the solid. It represents the case where one phase compresses, while the
other phase dilates. Due to the massive absorption of energy, the slower P-wave
is very difficult to detect in laboratory experiments. But even though several
workers has reported the existence of the second P-wave, it appears to be Kelder
& Smeulders (1997) who first observed its presence at ultrasonic frequencies in a
water-saturated sandstone. This research tends to establish the validity of Biot's
theory.

The equation for the S-wave can be found by calculating the rotation of *the equations of motion.* This will describe a wave whose velocity is given by (Johansen,

1997):

$$V_S = \left(\frac{\mu}{(1 - \phi)\, \rho_s + \left(1 - \widetilde{\alpha}\,(\omega)^{-1} \right) \phi \rho_f} \right)^{\frac{1}{2}}, \qquad (A.15)$$

where μ is shear modulus, and $\widetilde{\alpha}\,(\omega)$ is dynamic tortuosity.

Appendix B

Calculation of a phase change between two wavelets

To control that the phase change found graphically in chapter 4 was correct, calculations can be performed to get the theoretical values of this change, and then see if they coincide with result measured from the plot.

In this example two wavelet that have traveled through reservoirs where $Q = 200$, and $Q = 30$, respectively, are compared to each other. The thickness of the overburden is 2.000 meters.

The graphical display of the same comparison is shown in figure 4.6.

These calculations are based on equation 4.3, which states;

$$c(f, Q) = c(f_0) \left(1 + \frac{1}{\pi Q} \ln\left(\frac{f}{f_0}\right) - \frac{i}{2Q} \right). \qquad \text{(B.1)}$$

To calculate the phase rotation only the real part of this equation is used;

$$c(f, Q) = c(f_0) \left(1 + \frac{1}{\pi Q} \ln\left(\frac{f}{f_0}\right) \right). \qquad \text{(B.2)}$$

As mentioned in chapter 4, the default value for the reference frequency (f_0) in Nucleus is $100\,Hz$, while the center frequency of the Ricker wavelet used as the source signal (f) is $30\,Hz$. The phase velocity, $c(f_0)$, is $2.000\,m/s$.

Q=200

$$c_{200}(f, Q) = 2.000 \left(1 + \frac{1}{\pi * \times 200} \ln \frac{30}{100} \right) = 1.996, 17 \, m/s \qquad \text{(B.3)}$$

Q=30

$$c_{30}(f, Q) = 2.000 \left(1 + \frac{1}{\pi \times 30} \ln \frac{30}{100} \right) = 1.974, 45 \, m/s \qquad \text{(B.4)}$$

Further, one needs to calculate the travel time in the reservoir, by using the formula;

$$t = \frac{2d}{c_x(f, Q)}, \qquad \text{(B.5)}$$

where d is the thickness of the reservoir, and $c_x(f, Q)$ is the real part of the velocity denoted by the value of Q in the reservoir.

Q=200

$$t_{200} = \frac{2 \times 50}{1.996, 17} = 0.0500959 \, s \qquad \text{(B.6)}$$

Q=30

$$t_{30} = \frac{2 \times 50}{1.974, 45} = 0.0506470 \, s \qquad \text{(B.7)}$$

The difference in traveltime between the two cases is:

$$\Delta t = t_{30} - t_{200} = 0.0506470 - 0.0500959 = 5, 511 \exp -4 \qquad \text{(B.8)}$$

The phase rotation, when the change in time is a known factor, is defined by;

$$\Delta \varphi = 2\pi f \Delta t \qquad \text{(B.9)}$$

Using the calculated difference in traveltime, the phase rotation given in radii is:

$$\Delta \varphi = 2\pi \times 30 \times 5, 511 \exp -4 = 0, 10388 \qquad \text{(B.10)}$$

This converted into degrees will be:

$$\frac{\Delta \varphi \times 180}{\pi} = \frac{0, 010388 \times 180}{\pi} = 5.95$$

The phase rotation in this example equals 5.95 deg, which coincides very well with measured results (5.9 deg).

Appendix C

Offset vs angle of incidence - from chapter 5

In chapter 5 the modeled seismograms are compared to plots of the reflection coefficients for the P-P, P-S and S-S waves.

To be able to compare these figures carefully, it is necessary to find the correct conversion from the offsets given in meters to the offsets given in angle of incidence.

This is done by using the *NORSAR- 2D ray modelling* package.

The plots of these conversions are displayed in figures C.1 and C.2.

The figure C.1, illustrates the connection between the offsets in kilometers and the offsets in angle of incidence for the scenario where the overburden is dry

Figure C.2, illustrates the same connection, but for the scenario where the overburden contains a 50% saturated gas-cloud .
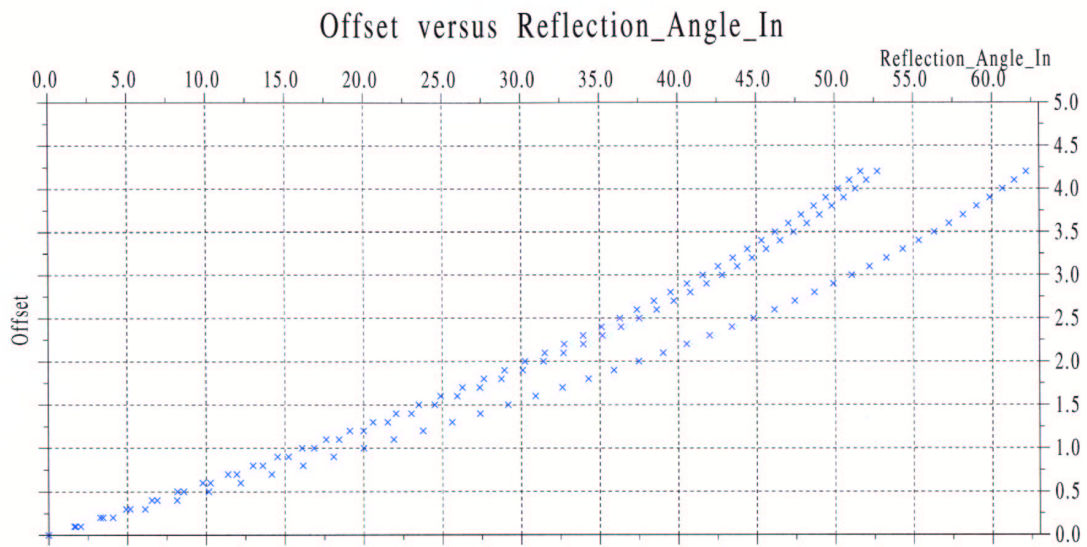
Figure C.1: *The offset in kilometers is plotted against angle of incidence for the case of dry overburden.*
The P-S wave is displayed farthest to the right, the P-P wave in the middle and the S-S wave is the one to the left.
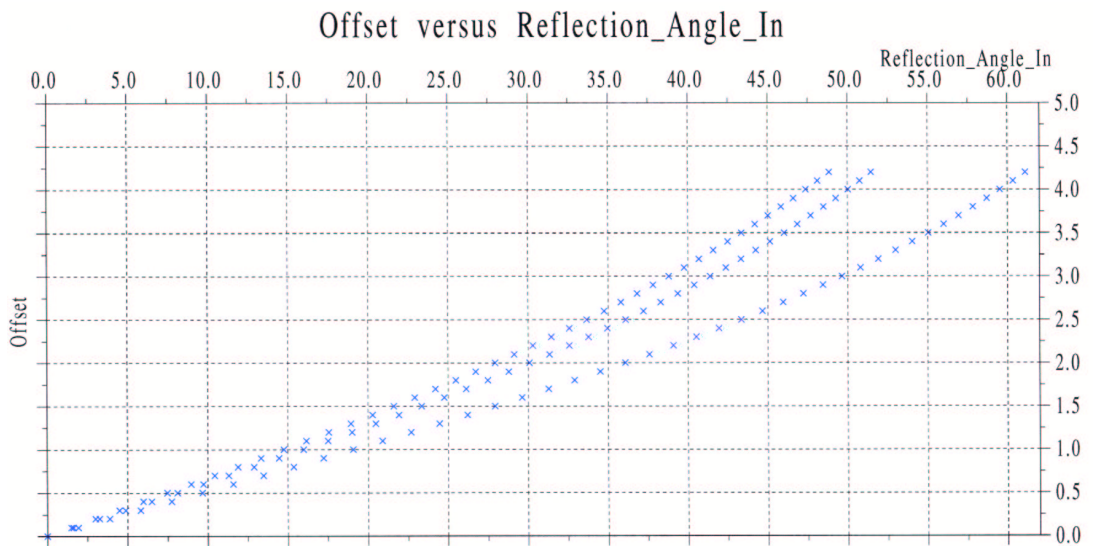

Figure C.2: *The offset in kilometers is plotted against angle of incidence for the case where a 50% saturated gas-cloud is situated in the overburden.*
The P-S wave is displayed farthest to the right, the P-P wave in the middle and the S-S wave is the one to the left.

Appendix D

Well $25/8 - 6T2$

Table D.1, gives the parameters extracted from well $25/8 - 6T2$ at the Jotun Field.

These parameters are used to build the initial earth model in chapter 6.

Due to the fact that the layers here are rather thin, especially layers 25 to 36, a smoothened version of this table was made. The new table (table 6.1) is used as the basis for the earth models generated to model the results from the Jotun field.

Well $25/8 - 6T2$						
	$d\,(m)$	$V_p\,(m/s)$	$V_s\,(m/s)$	$\rho\,(kg/dm^3)$	Q_p	Q_s
Layer 1	128	1470	0	1.04	10.000	10.000
Layer 2	12	1644	315	1.82	10.000	10.000
Layer 3	40	1778	422	1.92	10.000	10.000
Layer 4	55	1864	492	1.99	10.000	10.000
Layer 5	90	1935	548	2.05	10.000	10.000
Layer 6	200	1942	553	2.05	10.000	10.000
Layer 7	100	1923	538	2.04	10.000	10.000
Layer 8	100	1932	545	2.05	10.000	10.000
Layer 9	100	2028	622	2.12	10.000	10.000
Layer 10	100	2105	684	2.18	10.000	10.000
Layer 11	100	2128	702	2.20	10.000	10.000
Layer 12	80	2186	749	2.25	10.000	10.000
Layer 13	79	2225	780	2.28	10.000	10.000
Layer 14	78	2247	798	2.30	10.000	10.000
Layer 15	78	2207	765	2.27	10.000	10.000
Layer 16	79	2104	683	2.18	10.000	10.000
Layer 17	79	2057	645	2.14	10.000	10.000
Layer 18	80	2089	671	2.17	10.000	10.000
Layer 19	80	2128	762	2.20	10.000	10.000
Layer 20	80	2222	778	2.28	10.000	10.000
Layer 21	80	2326	860	2.36	10.000	10.000
Layer 22	80	2357	886	2.38	10.000	10.000
Layer 23	80	2465	972	2.47	10.000	10.000
Layer 24	67	2620	1100	2.36	10.000	10.000
Layer 25	4.3	3100	1550	2.32	10.000	10.000
Layer 26	7.8	3200	1800	2.14	10.000	10.000
Layer 27	3.9	2800	1270	2.30	10.000	10.000
Layer 28	8.6	3200	1750	2.12	10.000	10.000
Layer 29	1.4	3100	1530	2.32	10.000	10.000
Layer 30	8.2	3400	1820	2.14	10.000	10.000
Layer 31	3.8	3030	1550	2.25	10.000	10.000
Layer 32	7.0	3350	1810	2.14	10.000	10.000
Layer 33	3.2	3400	1800	2.17	10.000	10.000
Layer 34	12.3	3450	1810	2.21	10.000	10.000
Layer 35	11.8	3520	1830	2.19	10.000	10.000
Layer 36	1.8	2750	1100	2.34	10.000	10.000
Layer 37	880.8	3500	1840	2.21	10.000	10.000

Table D.1: *The physical parameters extracted from well $25/8 - 6T2$ from the Jotun Field.*

Appendix E

Offset vs angle of incidence - for chapter 6

As in chapter 5, the modeled seismograms in chapter 6 are compared to a plot of the reflection coefficients for the P-P, P-S and S-S waves. Due to the fact that the values for the velocities and the density in the layers are independent of the degree of saturation in the overburden, the reflection coefficients are the same for all cases.

To be able to compare these figures carefully, it is necessary to find the correct conversion from the offsets given in meters to the offsets given in angle of incidence.

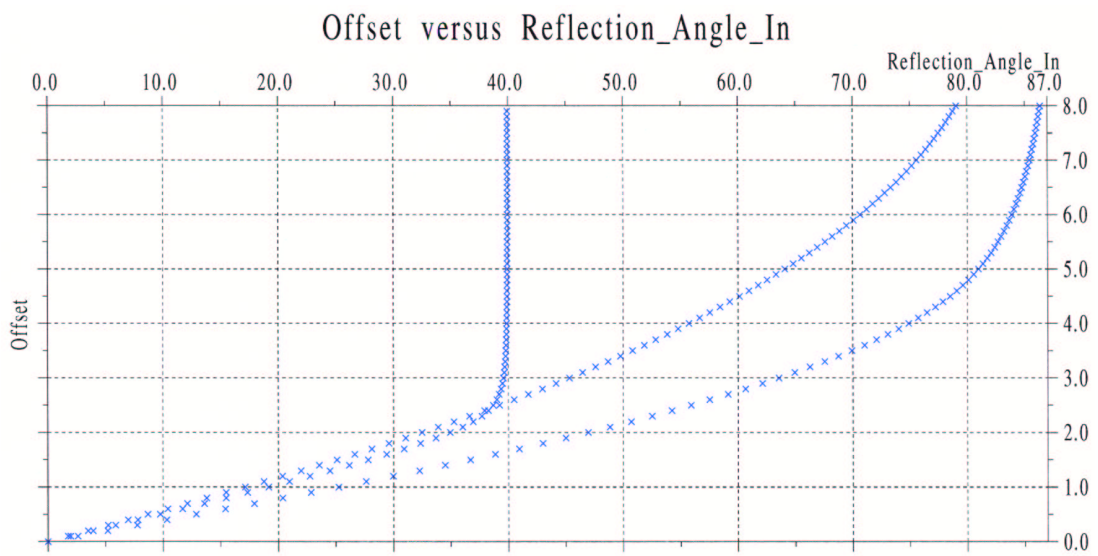The plot of this conversion is displayed in figure E.1.

Figure E.1: *The offset in kilometers is plotted against angle of incidence for the case of dry overburden.*
The P-S wave is displayed farthest to the right, the P-P wave in the middle and the S-S wave is the one ending at an angle of 40 deg *(critical angle).*